REACTIONS AND INTERFACIAL BEHAVIORS OF THE WATER–AMORPHOUS SILICA SYSTEM FROM CLASSICAL AND AB INITIO MOLECULAR DYNAMICS SIMULATIONS

Jessica M. Rimsza, B.S.

Dissertation Prepared for the Degree of

DOCTOR OF PHILOSOPHY

UNIVERSITY OF NORTH TEXAS

May 2016

APPROVED:

Jincheng Du, Major Professor
Richard Reidy, Committee Member
Nigel Shepherd, Committee Member
Witold Brostow, Committee Member
Zhenhai Xia, Committee Member
Andrey Voevodin, Chair of the Department of Materials Science and Engineering
Costas Tsatsoulis, Dean of the College of Engineering
Costas Tsatsoulis, Interim Dean of the Toulouse Graduate School

Rimsza, Jessica M. *Reactions and Interfacial Behaviors of the Water-Amorphous Silica System from Classical and Ab Initio Molecular Dynamics Simulations*. Doctor of Philosophy (Materials Science and Engineering), May 2016, 214 pp., 21 tables, 37 figures, references, 307 titles.

Due to the wide application of silica based systems ranging from microelectronics to nuclear waste disposal, detailed knowledge of water-silica interactions plays an important role in understanding fundamental processes, such as glass corrosion and the long term reliability of devices. In this dissertation, atomistic computer simulation methods have been used to explore and identify the mechanisms of water-silica reactions and the detailed processes that control the properties of the water-silica interfaces due to their ability to provide atomic level details of the structure and reaction pathways. Through the development of nanoporous amorphous silica structure models, the interactions between water and the complex unhydroxylated internal surfaces identified the unusual stability of strained siloxane bonds in high energy ring structure defects, as well as the hydroxylation reaction kinetics, which suggests the difficulty in using DFT methods to simulate Si-O bond breakage with reasonable efficiency. Another important problem addressed is the development of silica gel structures and their interfaces, which is considered to control the long term residual dissolution rate in borosilicate glasses. High temperature evolution of the silica-gel-water (SGW) structure was performed through classical MD simulation of the system, and growth of the gel into the water region occurred, as well as the formation of intermediate range structural features of dense silica.

ACKNOWLEDGEMENTS

First, I would like to thank Dr. Jincheng Du, who has been a wonderful and patient adviser over the last four years, not just in guiding my technical work, but also as a mentor for the development of my academic career.

I would also like to thank my committee members, Dr. Richard Reidy, Dr. Nigel Shepherd, Dr. Witold Brostow, and Dr. Zhenhai Xia, as well as Dr. Jeffry Kelber (UNT Chemistry), Dr. Joe Ryan (PNNL), Dr. Sebastien Kerisit (PNNL), and Dr. Louise Criscenti (Sandia) for providing additional technical expertise into my research.

I have been able to work with many excellent scientists from around the world, and I would like to thank them for providing insight into the wider scientific community: Dr. Christian Bonhomme, Dr. Christel Grevais, Dr.Haiyan Xiao, and Dr. Xiaotao Zu.

The friendships that I developed during my time at UNT have provided encouragement during my graduate studies: Doug Kinkenon, Dr. Ankit Srivastava, Jon-Erik Mogonye, Kris Mahdak, Graciela Penso, Dr. Niraj Gupta, Kyle Roget, Dr. Reinaldo Santos-Ortiz, Andres Garcia, Alyn Gray, Calvin Mikler, Matthew Karl, and Nathan Ley.

I would also like to thank my group members: Dr. Mrunal Chaudhari, Leopold Kokou, Dr.Ye Xiang, Wei Sun, Lu Deng, Menguo Ren, Xiaonan Lu, and PoHsuen Kuo.

Funding for my doctoral studies has been provided by the NSF Graduate Research Fellowship Program (NSF GRFP), DOE Nuclear Energy University Program (DOE NEUP), and the Semiconductor Research Corporation (SRC).

Lastly, I am very thankful for the continuing love and support of my family who have been such a big part of my journey towards earning my PhD. Without them, I truly would have been lost.

TABLE OF CONTENTS

Page

LIST OF TABLES

Page

LIST OF FIGURES

Page

CHAPTER 1

INTRODUCTION AND BACKGROUND

1.1 Introduction

Silica and water are two of the most abundant systems present on earth, with the earth's crust being composed of ~62% SiO_2 and 90% of rocks classified as silicate minerals, along with 1.4 billion cubic kilometers of water in the oceans and on the earth's surface, resulting in countless opportunities for water-silica interfaces to form [1-3]. Due to the wide application of silica in a variety of industries, there is significant interest in the processes and mechanisms which occur when silica surfaces come in contact with water.

One clear application is in geology, where the chemical weathering of silicate minerals, typically by interactions with aqueous environments, causes restructuring of the surface and affects the rate of silica diffusion in water, the stability of the earth's crust, and the ability to date geological formations [3,4]. Additionally, water causes hydraulic weakening in silicate minerals and alters the stress corrosion of silica glasses, particularly at highly strained crack tips [5].

Water-silica interfaces also impact the reliability of microelectronics, including the degradation of the mechanical properties of low-*k* dielectrics [6] and loss of interfacial adhesion properties [7]. Overall, corrosion effects related to the introduction of water into the system were predicted to be the cause of 20% of failures in microelectronic devices [8].

Many energy applications also use silica based materials, including catalysis supports [9-11], hydrogen storage materials [12-14], carbon sequestration to separate

CO_2 from gaseous exhaust streams [15-17], and humidity sensors [18], all of which use nanoporous silica.

The biomedical sector also employs silicate glasses, such as 45S5, the bioactive glass composition developed by Larry Hench, which is 45 mole% SiO_2, and has led to increased interest in the interface between bioactive glasses and body fluids, which are composed primarily of water molecules [19-21]. The formation of hydroxyapatite on the surface of bioactive glasses requires ion exchange and the development of silanol groups through water-surface reactions [22].

One of the most pressing needs for understanding the interfacial properties of water-silica systems was the development of borosilicate glass compositions in the 1970s for the vitrification of nuclear waste for long term storage [23] . Since radioactive isotopes remain active for thousands of years, host materials must be durable enough to stabilize the ions for comparable time frames [24].

Glasses present themselves as a solution for the immobilization of nuclear waste due to their long-term stability and the low probability of leaching elements into the surrounding environment [25]. For example, some naturally forming glasses, such as fulgurites and obsidians, have existed for over 3000 million years, suggesting that manmade glasses may experience similar longevity [23,25]. The incorporation of nuclear waste into a glass matrix adds the chemical durability of oxides to the system, providing a stable environment until the ions are no longer radioactive.

Current nuclear waste glasses are primarily borosilicates, with variations between the six countries which currently vitrify nuclear waste for disposal, from which an estimated 15,000 metric tons of nuclear waste glass have been produced [23-25]. An

example of the complex glass compositions used for nuclear waste disposal is SON68, a thirty component borosilicate glass (Table 0-1) which is an inactive surrogate for French vitrified nuclear waste [26]. To ease some of the difficulties associated with the analysis of such complex glass compositions, a simpler six component glass (Table 0-1), termed international simple glass (ISG), was selected by an international consortium for the standardization of results worldwide [26].

Table 0-1: International simple glass (ISG) and SON68 nuclear waste glasses compositions [26,27]

Composition (Mole %)	SiO_2	B_2O_3	Na_2O	Al_2O_3	CaO	ZrO_2	Other
ISG	60.2	16.0	12.6	3.8	5.7	1.7	0.0
SON68	45.5	14.0	9.9	4.9	4.0	2.7	19.0*

*Other elements include: Li_2O, Fe_2O_3, P_2O_5, NiO, Cr_2O_3, Cs_2O, SrO, Y_2O_3, MoO_3, MnO_2, CoO, Ag_2O, CdO, SnO_2, Sb_2O_3, TeO_2, BaO, La_2O_3, Ce_2O_3, Pr_2O_3, Nd_2O_3, UO_2, and ThO_2

By developing a detailed understanding of the mechanisms which control the dissolution rate of glasses, compositions which are capable of ensuring safe long-term storage of nuclear waste can be identified.

Due to the ubiquitous nature of silicates and water in the systems discussed above, there is a significant drive to understand the reactions and processes which govern water-silica interfacial properties. The analysis of these systems has been approached from many different angles, resulting in a significant research output in an effort to understand these interfaces. As an example in 1955 Krauskopf noted in his paper on the dissolution and precipitation of silica in fresh and salt water that “The literature of the geologic role of silica….is exceeding voluminous”, indicating that even

more than sixty years ago the available information of water-silica systems was beyond the scope of a single person to review in its entirety [27].

Therefore, in the following sections the aspects of the water-silica interface most critical to the work included in this dissertation is presented. The focus is on the water-silica interface, the hydroxylation process, formation of structured water, breakage of strained and unstrained Si-O bonds in silica, and a brief overview of the dissolution process in silica and multicomponent glasses. Difficulties and advantages of the use of computational and experimental methods are also included. For a more exhaustive description of the water-silica system the reader is directed to the following books on the topic [3,28-30]

1.2 Application of Experimental Methods to Water-Silica Systems

Long before the advent of modern experimental methods, analysis of water-silica systems was performed to provide insight into the role of water on the dissolution of silicate materials. One preliminary study of silica's solubility in water was performed by Church in 1867, which identified the polymerization of silica out of an oversaturated solution through visual examination [31]. Since then, the explosive advances in characterization of material interfaces has provided ample opportunity to investigate the water-silica surfaces with increased accuracy.

Application of experimental methods to water-silica interactions is broad, and most of the available characterization techniques have been employed, including secondary ion mass spectroscopy (SIMS), nuclear magnetic resonance (NMR) analysis, Fourier transform infrared spectroscopy (FTIR), transmission electron microscopy

(TEM), scanning electron microscopy (SEM), electron energy loss spectroscopy (EELS), Raman spectroscopy, and sum frequency generation (SFG) spectroscopy, among others. Many of these characterization methods encounter difficulties during the investigation of amorphous, insulating, or oxide materials, and in differentiating between atomic species. Brief descriptions of the most commonly used characterization methods with respect to their applications in glasses are discussed below.

The use of diffraction based characterization methods to investigate water-silica systems is complicated by the amorphous structure, which results in the formation of broad peaks in the diffraction pattern, and must be separated for the identification of interatomic distances [32,33]. However, neutron diffraction studies have been used extensively to identify the short range order, such as bond lengths and coordination numbers, in a wide variety of glasses [34-39]. Neutron diffraction becomes more complicated in the characterization of water containing systems due to the similar mass of hydrogens and neutrons. This generates incoherent background scattering which must be removed through statistical methods [33]. Deuterium exchange with hydrogen can be used to differentiate protons from neutrons, but cannot completely remove the noise in the diffraction spectra [33]. X-ray diffraction can also be used to identify the pair distribution functions from the localized order in amorphous materials [40-42], though it is limited to short range structural features. Neither neutron nor x-ray diffraction can differentiate between different oxygen or hydrogen sites [33].

Various types of vibrational spectroscopy, including FTIR and Raman spectroscopy have been used to analyze the structure of glasses [43-52]. Raman spectroscopy in particular has been used in the analysis of water-silica systems, since

this method is applicable to both solids and liquids and can identify terminal groups, such as non-bridging oxygen (NBO) or silanol groups on the surface [33,46,53]. Much like the diffraction based techniques, Raman spectroscopy of glasses struggles with the identification of structural features from a single broad peak in the spectra [33]. In the case of well-known systems, separating out individual contributions to this peak can be performed, but the process is more difficult if unusual peaks or features are noted [33,54]. The calculations of the vibrational density of states can be used to index structural features in the glass which appear in the Raman spectrum [33]. Additionally, the identification of bonding states in water is possible, which is critical for the analysis of hydrated systems [33]. Even so, application of IR spectroscopy to hydrated systems is complicated by the inclusion of absorbed water, which can interfere which the OH vibrations in the silanol groups [55].

Solid state NMR spectroscopy is also well suited for the study of amorphous systems through description of the local environment surrounding a nucleus. This technique does not require diffractions of neutrons, electrons, or x-rays [33]. As a result, NMR can identify different bonding environments in silicon, such as the number of bridging oxygens [56,57] and coupled O-H interactions in silanols [58-63], as well as providing information on the localized structure, such as bond angles [64,65]. NMR can investigate the interactions between water and silica due to the high natural abundance of the hydrogen-1 isotope (^{1}H), which has high NMR sensitivity [33]. Silica systems have other complexities for NMR analysis, notably the low natural abundance of the NMR sensitive oxygen isotope oxygen-17 (^{17}O) at 0.04%, which requires isotope exchange

for analysis, and its high quadrupolar interaction, which makes identification of peak shifts more difficult [33].

Atom probe tomography (APT) has recently increased in popularity for analysis of oxide systems due to its ability to provide compositional information, especially across interfaces such as those formed during glass dissolution [33,66-70]. Traditionally, APT has been limited in glasses since it requires the ionization of individual atoms on the tip of a specimen, which can be difficult in insulators due to high mechanical stress developed during ionization resulting in the cracking of brittle samples [33]. Despite these limitations, APT has been applied to investigations of glass dissolution, and has provided insight on the composition of interfacial gel layers [71,72]. ATP methods work best for identifying the composition of gels developed from complex glass compositions, including heavy transition metals, but the analysis is more complicated in pure silica gels, composed almost exclusively of hydrogen, oxygen, and silicon [33].

For additional detailed information on the difficulties associated with characterization of glassy systems the reader is directed to Reference [33].

Due to the complexities present in the characterization of amorphous, insulating, and hydrated oxide structures, a mixture of the above techniques, plus those which have not been discussed in detail, must be used in order to fully characterize the glass surface. However, even if all available experimental techniques were applied, aspects of the glass system would still be difficult to identify, such as reaction mechanisms which occur in picoseconds, the changing charge of atoms involved in the reaction, the rate of siloxane breakage and reformation, and analysis of interface structures. Other

techniques have therefore been employed to provide additional information to develop a complete and mechanistic understanding of the processes which govern water-silica interactions.

1.3 Application of Computational Methods to Water-Silica Systems

In addition to the extensive application of experimental characterization techniques, simulation methods have also been used to investigate water-silica systems, since several of the difficulties which occur in the experimental analysis are not present. Here, the application of atomistic simulations are discussed in the investigation of water-silica systems, specifically the use of classical molecular dynamics (MD) and density functional theory (DFT) methods. Both of these computational approaches have been used extensively in the study of water [73-78], silica [79-84], and combined systems [85-91], with differing levels of accuracy and efficiency, allowing for the identification of diverse aspects of water and silica.

In the application of DFT simulations to water-silica interfaces, the calculation of the electronic structure, which is the basis of the method, are more accurate for light elements such as hydrogen and oxygen since the calculation of complex d- and f-electrons orbitals is not required [92]. DFT simulations can also provide information on the partial atomic charges and charge transfer during reactions, orientation of dipole moments and hydrogen bonds in water, or the movement of individual atomic species. Additionally, atomistic resolution in simulations can provide details on mechanisms responsible for individual bond breakage, which would be almost impossible to identify from the use of experimental characterization methods due to reaction speeds. Despite these advantages the application of computational methods have some challenges with

the simulation of water-silica systems. In *ab initio* DFT methods, which require full calculation of the electronic structure, simulation sizes are limited (<500 atoms) as is the time frame of the simulations (<100 ps) making long simulations difficult and computationally expensive [92]. To account for these cluster calculations, a small number of atoms which are suspended in vacuum, have been used, which negates the effects of the bulk material on the surface properties [93,94]. It was only in recent years that computational algorithms and hardware has become advanced enough to allow for the simulation of bulk surfaces and the accurate identification of surface features [92]. Without even greater efficiency in DFT algorithms and improvements in the networking of computer power, the ability to simulate larger systems (10,000+) will be outside the reach of *ab initio* simulations for many years to come.

A natural answer to the difficulties associated with using *ab initio* methods is the application of slightly less accurate, but much faster, classical MD simulations, which implements a user generated forcefield to describe the interatomic forces. With the use of more efficient classical MD methods larger systems (up to billions to atoms) can be simulated for longer time frames (milliseconds for accelerated molecular dynamics), opening up a range of dynamic studies which can be performed while maintaining atomistic resolution [95,96]. An added difficulty in this case is the development of classical MD potentials, which must be designed to simulate the water-silica systems, and requires knowledge of the reaction mechanisms which occur in the system. The development of dissociative forcefields which can describe the complex bonding environments, changing atomic speciation, accurate reaction mechanisms, in water-silica systems, all with reasonable efficiency, has been a challenge. Several recent

successes have been identified, primarily the development of a bond order based potential by van Duin, Goddard, and colleagues [82,85,97,98], which serves as an improvement over a number of earlier potentials [99-104] which had difficulties allowing for the unpredictable siloxane bond breakage on complex silica surfaces. A more in-depth discussion of the challenges associated with developing water-silica force fields and evaluating them based on available *ab initio* data is discussed in Section 4.2.

In order to simulate systems with DFT accuracy but classical MD efficiency, quantum mechanical and molecular mechanics (QM/MM) are sometimes used, with a higher level of theory, such as DFT, applied to the area of interest, while the rest of the system is simulated with less accurate methods [105,106]. The use of QM/MM simulations can be complicated since they require a method of connecting the two regions, and results have been shown to be sensitive to the amount of the surface which is treated with DFT [105,106].

The application of both computational and experimental methods to the investigation of water-silica systems has resulted in the identification of key features of the water-silica interfaces and the process of silica dissolution.

1.4 Evolution of the Water-Silica Interface

The development and evolution of the water-silica interface is time dependent, due to the relatively high activation energies for the breakage of siloxane bonds, the kinetics of the reactions, and stability of the initial oxide structure as well as the possible formation of interfacial regions on the surface.

In the following sections examples of changing features of the water-silica interfaces are identified, including hydroxylation of the silica surface, formation and identification of silanol concentrations, properties of nanoconfined water, breaking of Si-O bonds in strained and unstrained configurations, and the dissolution of silica and silicate glasses.

1.4.1. Hydroxylation and Surface Silanol Concentrations

The interfacial properties of silicates are controlled by the existence of surfaces species, which in non-functionalized silica are almost exclusively hydroxides or silanols (Si-OH). The concentration of silanols affects the reactivity of the surface, and can alter the surface character from hydrophilic to hydrophobic [107]. The hydrophobic character of the silica surface is due to siloxane (Si-O-Si) bonds, which do not form hydrogen bonds with water, and isolated silanol groups, which occur when only one silanol groups is bonded to a silicon [107,108]. The isolated silanol groups do not allow for sufficient hydrogen bond formation to result in hydrophilic behavior. In contrast, hydrophilic silica is generated by closely spaced vicinal silanol groups or geminal silanols, formed when two silanol groups are bonded to the same silicon, allow for the creation of a hydrogen bonded water network due to the polar nature of the –OH group which stabilizes the water on the surface [107-109]. A sketch of the structure of geminal and vicinal silanols, as well as siloxane bonds, on the silica surface, is included in Figure 0-1.

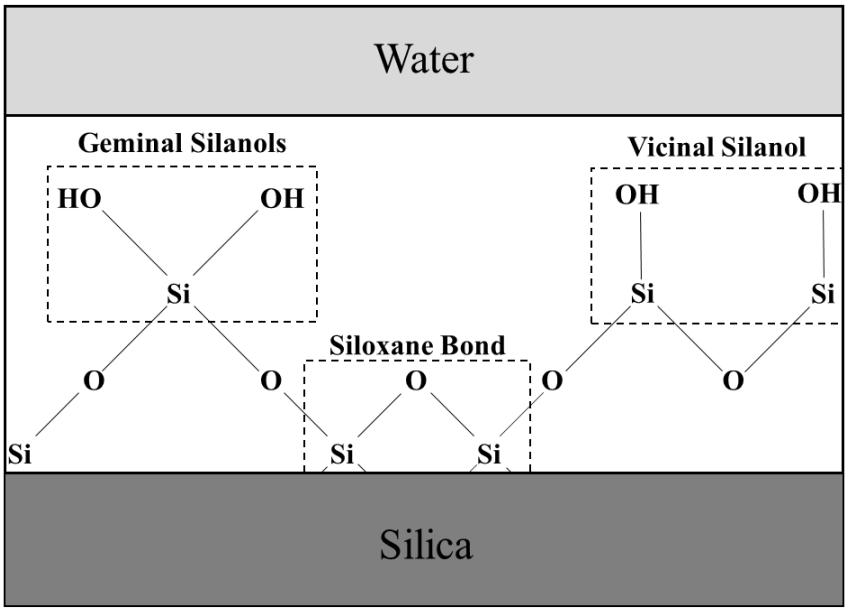

Figure 0-1: Sketch of geminal silanols, vicinal silanols, and siloxane bonds located on a silica surface.

The differences in the silanol species are not only responsible for the hydrophilic surface but also affect the acidity, altering the surface chemistry [110]. The identification of both vicinal and geminal silanol species has been performed using FTIR [55,108], NMR [111], and SIMS [112]. Differences in silanol species appears in the studies of dried or annealed silica surfaces, since above 800K the geminal silanol groups recombine to form additional siloxane bridges, increasing the hydrophobic character of the surface [55,111,113].

Silanol groups are first formed through the termination of coordination defects, such as NBO and under bonded silicon (Si^3), which form silanol groups during reaction with water, as in Eq. 0-1 and Eq. 0-2.

$$Si^3 + H_2O \rightarrow Si - OH + H^+ \quad \text{Eq. 0-1}$$

$$NBO + H_2O \rightarrow Si - OH + OH^- \quad \text{Eq. 0-2}$$

H^+ (protons) or OH^- (hydroxides) which are formed during the reactions typically recombine with other OH^- or H^+ in the water, resulting in the formation of complete water molecules. Since both H^+ and OH^- are required to terminate coordination defects on the surface the removal of even numbers of NBO and Si^3 results in the consumption of water molecules through their transformation into silanol groups. At high and low pH values coordination defects such as NBO or Si^3 can be stabilized, due to the formation of other species, such as $Si\text{-}O\text{-}Na^+$ in systems with high sodium concentrations, at the silica surface [102,114].

The hydroxylation of coordination defects is too fast to be identified experimentally, and recent *ab initio* investigations have indicated that the process does not have an activation energy, indicating the speed with which the coordination defects are removed [115]. In computational systems hydroxylation times for the NBO defects have been identified as <10 picoseconds, with varying NBO stability due to the use of closed shell methods in the DFT simulations and changing simulation sizes, with NBO's being preferentially terminated through proton transfer from a H_3O^+ [87,116,117].

Experimentally, the measurement of silanol groups can be complicated by the low silanol concentration on flat surfaces, compared to hydrated systems, where the concentration is higher and easier to identify. In fully hydroxylated surfaces, such as those developed in ambient conditions and in powders, surface silanol concentrations of ~4.6 silanol/nm^2 have been reported [112,118]. Classical MD simulations identified that by terminating all the coordination defects and opening ring structure defects, silanol surface concentrations of ~4.6 silanol/nm^2 occur, consistent with the experimental

values indicating that the formation of surface silanols is primarily due to the removal of high energy defects [86,112].

In order to investigate the hydroxylation rate of un-reacted silica surfaces, silica rods were fractured under ultra-high vacuum [119-121] by D'Souza and Pantano, to develop a surface without an initial concentration of silanol groups and slow the hydroxylation process by limiting water in the atmosphere, with silanol concentrations to be measured quantitatively using SIMS [118]. Stable silanol concentrations of 2.5-2.6 silanol/nm^2 were identified, as was an initial increase in silanol concentration followed by an equilibrium value, due to removal of strained Si-O bonds in high energy structures on the surface [118]. The changing silanol concentration with time is included in Figure 0-2 from Reference [118].

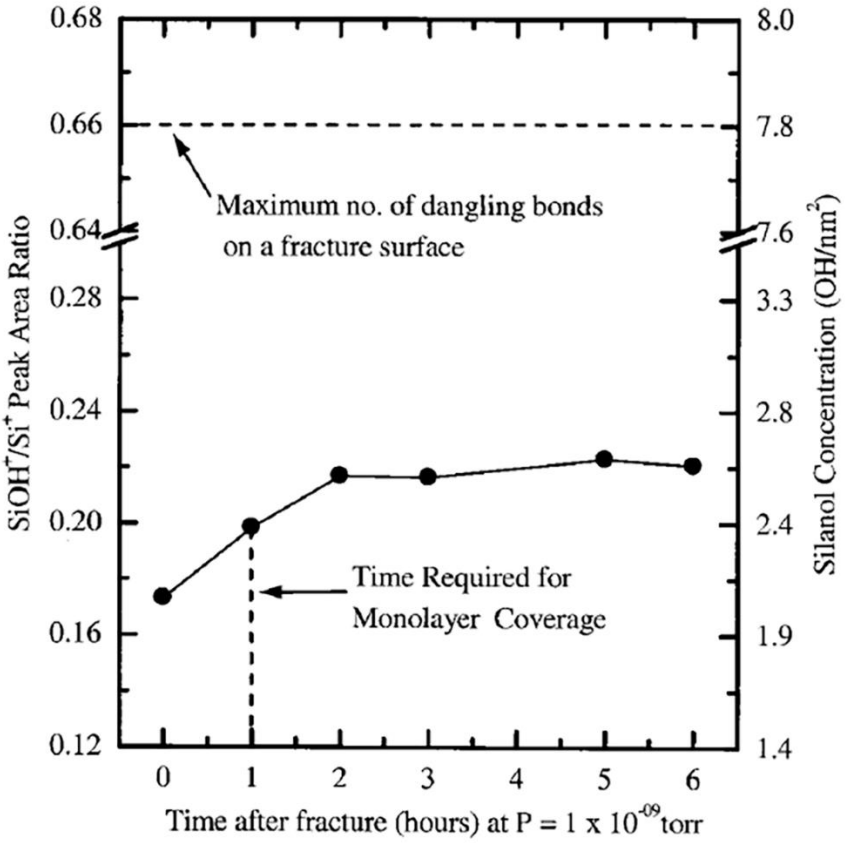

Figure 0-2: Silanol concentration with time after fracture for silica glass broken in ultra-high vacuum (10^{-9} torr) conditions [119].

Rapid increases in silanol concentration after other types of surface modification, such as etching, was also noted by Davis and Tomazawa [122]. A combined metastable impact electron spectroscopy and ultraviolet photoelectron spectroscopy study was used to identify increased silanol concentration with water coverage on a silica surface and suggested that silanol species stabilize hydrogen bonding in bulk water [123].

The stabilization of hydrogen bonds has also been identified in an analysis of silanol species, which have been shown to affect the formation of frozen or structured water, identified as water adjacent to fully hydroxylated surfaces. This region of water is

dynamically limited, and has also been identified through the use of proton NMR, neutron diffraction, and differential scanning calorimetry [58,60,63,124]. In NMR, frozen water typically appears as changes in the ^{1}H NMR spectra, indicating a modification in the hydrogen bonding environment around the proton [125]. The structuring of water adjacent to nanoporous silica surfaces is connected to changing surface properties due to varying Si-OH concentrations, including Si-OH enrichment in acidic conditions [57] and the decrease in viscosity of the confined water identified by resonance shear measurements [126]. The affect is seen primarily in water confined in pores less than 1 nm in diameter [58] and due to the high level of confinement which is required to identify this affect, it is well suited to detailed analysis by computational methods.

Using classical MD [89,109,127-133], *ab initio* [134,135], or grand Monte Carlo (MC) [59,129] computational methods, several features of nanoconfined water have been identified. These include the existence of density fluctuations up to 10Å away from the surface due to the structure of water based on the surface morphology, with the hydrogen atoms directed toward the surface and limited rotational dynamics, and smooth pore walls increasing the level of organization [59,109,127,129,133,135]. The distortion of the water molecules has been quantified by a tetrahedral order parameter, which outlines the formation of a structured water unit formed from hydrogen bonds and regulated through the O-O-O bond angle, which is consistent with values of O-O-O seen in hexagonal ice [134]. Water diffusion next to the surface is limited compared to the bulk, the affect is more extreme when the surface of the pore is rough, and it varies with the amount of water which is confined [59,109,127,128,130,131,134]. The slowing of water diffusion is due to the formation of hydrogen bonds between the water and the

silanol groups, which limits the atomic movement, resulting in increasing diffusion rates as the water molecules move away from the surface [127,134]. In some cases the effect of the interface on the diffusion coefficients can be identified up to 1 nm away from the surface [128,129].

While there is significant evidence demonstrating the slowing of the diffusion of water molecules next to interfaces, it is unclear if this affects the fast transport of protons through the solution due to the hydrogen hopping mechanism [59,109,128,130]. Fast movement of hydrogen through the solution occurs as hydrogens transfer from one water molecule to another, with the formation of H_3O^+ ions as intermediate molecules, allowing for diffusion of hydrogen without the movement of the entire water molecule [136]. Several computational studies have investigated proton transport as a common method of facilitating proton transport through bulk water to terminate coordination defects [85,131,136]. Whether or not proton diffusion is slowed in the interfacial region would provide insight into how the dynamics of the molecules near the reaction sites affects the water-silica reaction rates.

Overall, the concentration and type of silanol groups on the silica surface has significant effects on the reactivity of the surface, the rate of water diffusion next to the interface, and the formation of structured water due to hydrogen bonding network.

1.4.2. Strained Siloxane Bond Breakage

After all of the coordination defects on the surface have been terminated with water, any additional hydroxylation of the surface is due to the breakage of siloxane bonds on the surface. The breaking of a siloxane bond by a water molecule results in

the formation of two silanol groups (Eq. 0-3) with the de-hydroxylation process being the reverse, with the condensation of two silanol groups, resulting in the formation of a siloxane bond and a water molecule (Eq. 0-4) [137].

$$Si - O - Si + H_2O \rightarrow 2SiOH \quad \text{Eq. 0-3}$$

$$2SiOH \rightarrow Si - O - Si + H_2O \quad \text{Eq. 0-4}$$

In silica systems both strained and unstrained bonds exist, and significant differences in silanol reactivity is noted [118,121], affecting water-silica reaction rates. Based on classical MD simulations it has been suggested that over 60% of the silanol groups on the surface are the result of strained Si-O bond breakage, rather than the termination of coordination defects while unstrained bonds remain stable [86].

Unstrained Si-O bonds have a length of ~1.6Å in dense silica [32,138-140] and are located in SiO_4 tetrahedron with Si-O-Si and O-Si-O bond angles of 147° and 109.3° respectively [98,141]. These unstrained Si-O bond angles and distances typically occur in silica rings which contain five or more silicon atoms in addition to the bridging oxygen, and allows for sufficient freedom in the Si-O-Si bond angle to create a relaxed system [142]. The peak in the ring size distribution for dense silica is six-membered rings, which is also the primary ring structure in crystalline SiO_2, such as cristobalite [143] .

Strained siloxane bonds typically occur in smaller rings, including four-membered, three-membered, and two-membered rings, with smaller rings resulting in more perturbation of the Si-O-Si and O-Si-O bond angles as seen in Figure 0-3 [144]. Three-membered and four-membered rings have been identified in experimental systems through the use of Raman [144,145], x-ray photoelectric spectroscopy [146] , NMR [147], and FTIR [147,148], and the computational analysis of structure models is

used in order to index peak positions seen in the experimental results [149]. Schematic representations of two-membered, three-membered, and four-membered rings in silica are included in Figure 0-3.

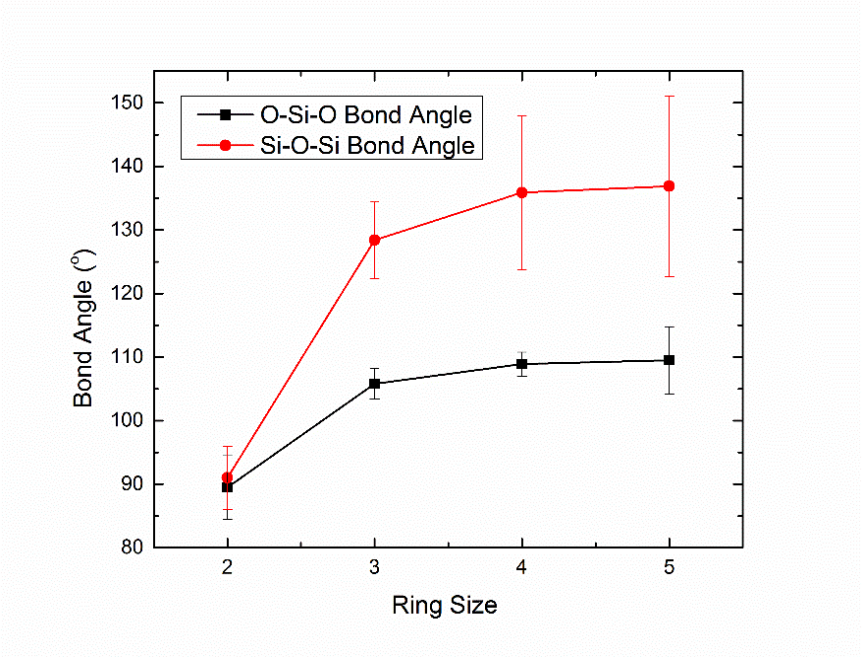

Figure 0-3: Changing O-Si-O and Si-O-Si bond angles with ring size. Data for three-membered, four-membered, and five-membered rings are from Raman spectroscopy [145], and two-membered data is from Section 4.4.1.

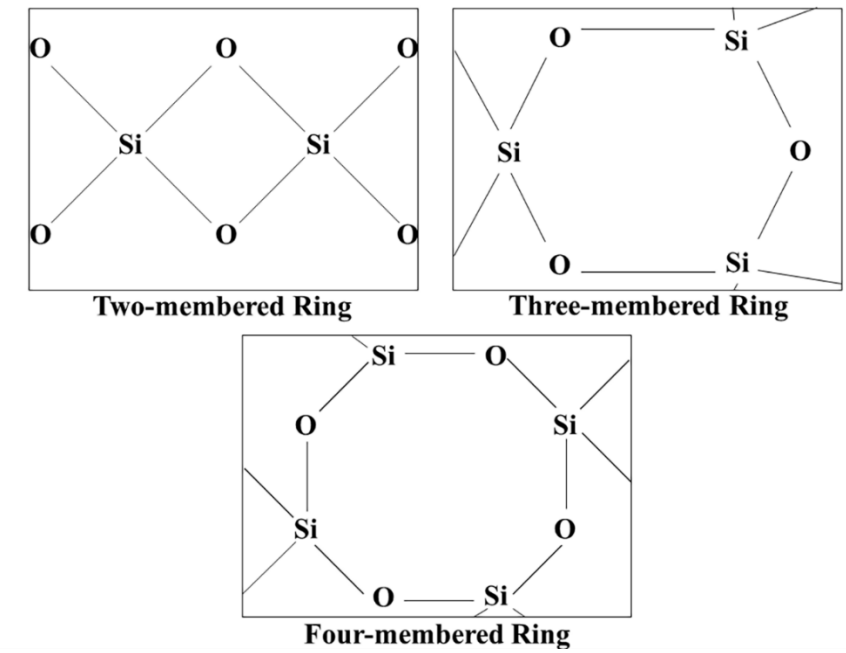

Figure 0-4: Sketch of two-membered, three-membered, and four-membered ring structures in silica.

Typically, these small membered rings are present in dilute concentrations, with ~0.2% of oxygen in silica located in three-membered rings and only ~0.4% of oxygen in four-membered rings by solid state NMR [149], and up to 20% concentration of three-membered rings on silica surfaces by Raman spectroscopy [147]. When the system is under high pressure [150], or when insufficient water is present to allow for the formation of silanol groups [118], higher concentrations are identified. Experimental evidence for high energy two-membered rings exist through the use of NMR and are noted to be primarily a surface defect [147].

The activation energies for the removal of the high energy ring structures vary compared to unstrained six-membered rings, and have therefore been of interest since strained silica ring removal is one of the first stages of the dissolution of silica surfaces.

It has been suggested that changes in the tetrahedral geometry around the silicon in small rings alters the Si-O-Si bonds from hydrophobic to hydrophilic, encouraging interactions with water and the breaking of the bond [147]. Mechanisms for the breakage of strained and unstrained siloxane bonds, including the formation of intermediate defects, such as over-bonded silica (Si^5) and hydrogens bonded to bridging oxygen, are discussed in detail in Section 3.4.1.

Generally, two-membered and three-membered ring defects are considered to be metastable in experimental systems, and strained ring removal is predicted to occur within the first few seconds in experimental systems, due to the rapid increase in silanol concentrations for silica surfaces formed in ultra-high vacuum conditions [118,147]. Removal of the strained Si-O bonds in two-membered rings occurs at rates ~100,000-75x greater than for unstrained bonds in amorphous silica [118,147,148]. Due to the extremely fast kinetics for the removal of strained ring species, analysis of the mechanisms responsible for siloxane bond breakage is outside the range of what can be identified experimentally.

The fast dynamics of the reactions are well suited to further study by computational methods, since atomistic resolution can be achieved, and short reaction times are simulated with highly accurate electronic structure methods. Additionally, higher concentrations of two-membered defects occur in computational systems due to the fast cooling rates which are used to generate silica models from melt and quench procedures [151]. Activation energies for the most strained Si-O bonds present in pure silica, two-membered rings, are between 0.32-1.27eV depending on the simulation size, computational method used, the bond breakage mechanism, and the location of the ring

in the silica systems [93,94,98,105,152,153]. A description of these activation energies is included in Table 0-3 and a detailed discussion of the removal of two-membered ring defects is the basis of Chapter 3.

An accurate understanding of the removal of the high energy siloxane bonds from the silica surface when in contact with water provides a base line for the energetics associated with silica dissolution since the removal of unstrained bonds is expected to be significantly slower.

1.4.3. Dissolution Process in Pure Silica

In the equilibrium dissolution process of pure silica, the system begins with a fully hydroxylated surface, from which the highest energy coordination and ring structure defects have been removed, as discussed in the previous sections. The result is dense silica composed of SiO_4 tetrahedral, with the exception of the surface silicon, which will be bonded to between 0-3 silanol groups. At this point, all of the silicon bonds are unstrained, and the dissolution process can become more complicated since the reactivity of the different silicon species is less clear.

To further analyze this process the number of bridging oxygens connected to a silicon, described as Q_n speciation, with n as the number of bridging oxygens, can be used to separate out the bonding states. Sketches of Q_4, Q_3, Q_2, and Q_1 structures of silica is included in Figure 0-5.

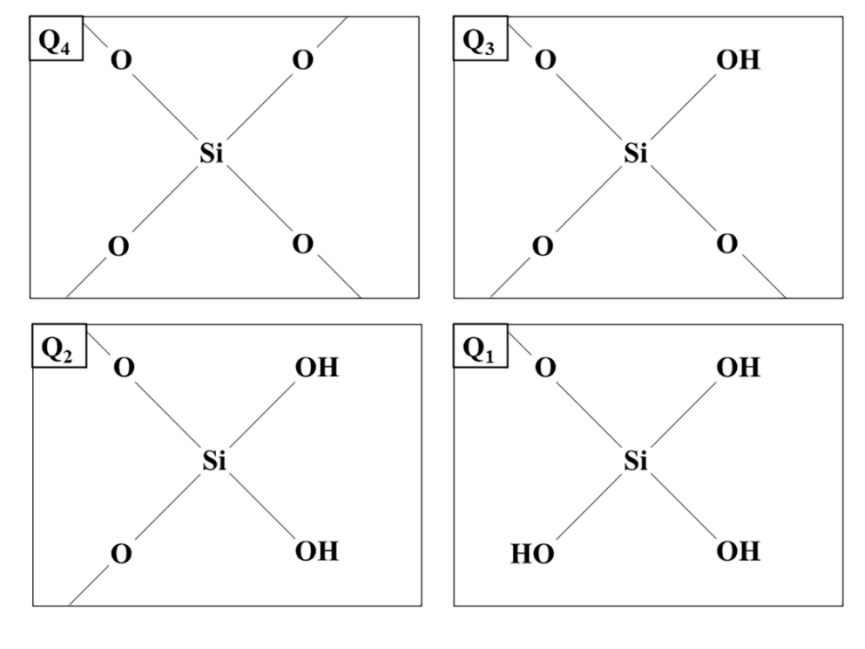

Figure 0-5: Sketch of Q_4, Q_3, Q_2, and Q_1 species in silica.

It has been theorized that the dissolution process begins with a fully bonded silicon as a Q_4 species, and then bridging oxygen bonds break one by one, forming a Q_3, then a Q_2, a Q_1, and finally a Q_0 species (SiO_4H_x) [154]. During each siloxane bond breakage a NBO and a Si^3 defect will form, which will be hydroxylated by nearby water molecules, resulting in the consumption of water in the reaction described by Eq. 0-3. The mechanism for the breakage of an unstrained siloxane bond, and in particular how it may vary from strained siloxane bonds is still under investigation, with several different mechanisms being proposed [87,155,156]. Regardless of the mechanism, the result is the development of hydroxylated silica monomers, SiO_4H_x, in solution, which have been identified as the primary dissolved silica species by Raman spectroscopy [157,158].

The activation energy of the breakage of each siloxane bond cannot be identified experimentally, but the energetics of the removal of an entire SiO_4 unit has been

identified and values between 0.62-1.12 eV are reported [159,160]. The activation energy depends on the composition of the solution, temperature, and the use of a bulk or powdered sample [161,162], and higher values of ~2.0eV were reported computationally [117]. Other studies also report that activation energies are highly dependent on temperature, composition of the solution, pH, fluid flow rates, and silica concentration [159,160,163-165]. These activation energies are significantly lower than the Si-O bond energies of 5-6eV identified by DFT methods [166] indicating the important role that water plays in lowering the energy for breaking the siloxane bond.

Since activation energies are variable, computational studies provide a more detailed understanding of the energetics for the removal of SiO_4 tetrahedra from the surface due to the ability to control and identify the intermediate steps involved in the dissolution process. This type of analysis provides insight into which of the transitions ($Q_4 \rightarrow Q_3$, $Q_3 \rightarrow Q_2$, $Q_2 \rightarrow Q_1$, or $Q_1 \rightarrow Q_0$), has the highest activation energy and therefore may be the controlling factor in silica dissolution [88,155,167]. Simulations can also investigate the role of extra protons or hydroxides on the energy barrier, due to the ability to precisely control the simulation environment.

Examples include work by Zapol et al., who investigated energy barriers for the breakage of Si-O-B bridging oxygen bonds in borosilicates, based not just on the bridging oxygen concentration of the network formers, but also on the acidic or basic condition of the solution using *ab initio* methods [167]. From this work it was identified that acidic conditions decrease the energy barrier, suggesting that low pH will result in faster dissolution rates [167]. The identification of activation energies based on Q_n speciation has also been performed for pure silica systems, and from this analysis the

$Q_2 \rightarrow Q_1$ transition was identified as having the highest activation energy, though absolute values are off by a factor of two between classical MD [88] and *ab initio* methods [155]. The most stable Si-O-Si bonds consist of two Q_4 silicon, such as found in a fully coordinated set of tetrahedron, with an activation energy of ~2.2eV, indicating the importance of less coordinated Q_n species in silica dissolution [155]. The wide range of these values makes the analysis of water-silica interactions complicated since without a consistent value the inclusion of this information in MC simulations or dissolution model is difficult [154,168].

During silica dissolution the successive removal of silica tetrahedra results in the formation of a fragmented silica gel which has been hydrated by the diffusion of water molecules into the systems as the silica monomers diffuse into the bulk water.

Further identification of the dissolution of pure silica is complicated by the slow rate of the dissolution process and the high variability in the kinetics due to the role of dissolved species and the pH of the solution [169]. The amorphous surface also presents its own challenges, due to the changing concentration of surface sites as silica dissolves and silica polymerizes on the surface. Therefore, the typical mechanisms for description of the dissolution of crystalline silicates cannot be applied [160]. Additionally, the use of deuterium to improve the ability to analyze the resulting hydrated systems has been shown to decrease dissolution rates by a factor of four, providing additional complexity to the analysis [156]. Finally, pure silica glasses do not have the wide spread use that multicomponent glasses or silicate minerals have, resulting in fewer investigations of pure silica than other compositions, particularly in experiments.

Computational analysis of water-silica systems has been slowed by the variability in reaction rates and energies for water in complex silica structures, discussed in Chapter 3, and it is the intention that the information in this dissertation will provide insight into the aspects of the longer term dissolution process, in addition to an analysis of the activation energies and reaction mechanisms.

1.4.4. Dissolution in Multicomponent Glasses

Up to this point, all discussion of water-silica interactions have focused on the interactions between pure silica with water, and have neglected the role of network formers and modifiers in multicomponent glasses, which have a profound effect on the interfacial properties of these systems. Analysis of the dissolution behavior of glass compositions more complex than pure silica are common in experimental literature since most applications require glasses with a high number of network modifiers or variations in network formers, such as nuclear waste glasses [26,170,171], bioactive glasses [19,21,172], and container glasses [173-175]. The different compositions result in a wide variation in the stages of silica dissolution based on the stability of the bonding structures inside the glass and the changing surface features with obsidians having lower dissolution rates compared to borosilicates or soda lime silicate glasses [176]. Due to the high variability in the composition of glasses and the unknown effect of even small compositional changes on the stability of glassy materials, the individual mechanisms which control the long term dissolution rate of multicomponent glasses are currently unidentified.

Despite these variabilities, the standard stages which are present in the dissolution of multicomponent glasses are known though the length and stability of each of the stages and the dissolution rates vary with composition. Loosely, the stages are identified as: (1) interdiffusion between the water and the network modifiers; (2) the generation of an initial dissolution rate due to hydrolysis of bridging oxygen bonds; (3) a drop in the dissolution rate due to the formation of interfacial gel layers; (4) a long-term residual rate that controls the majority of the glass dissolution and the further development of alteration layers and crystalline phases, and; (5) occasionally a final resumption rate associated with an increase in dissolution rate for select compositions occurs due to formation of zeolites on the surface [154,177]. An outline of these dissolutions stages are included in Figure 0-6 from Reference [178].

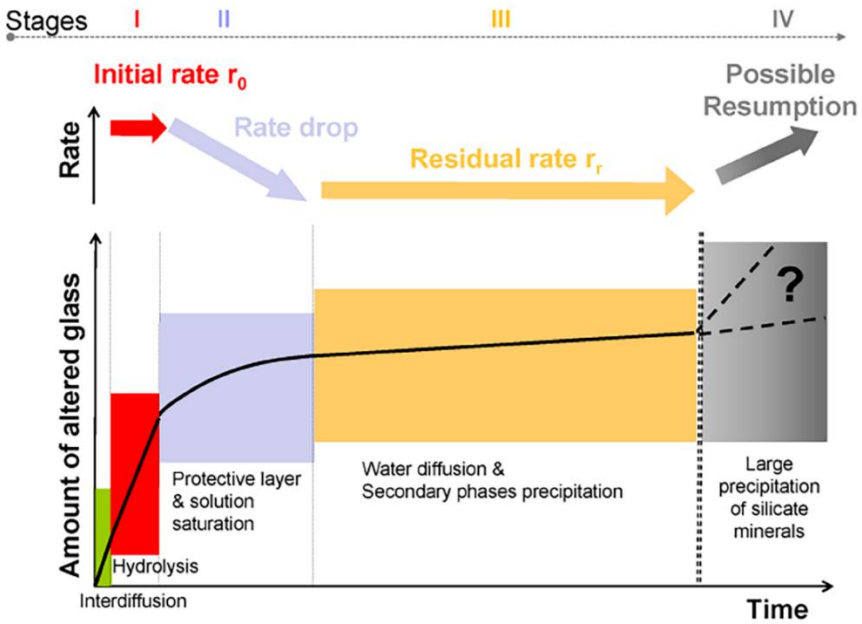

Figure 0-6: Outline of the dissolution stages of multicomponent glasses with their dissolution rates [179].

The first stage of dissolution is based on the inter-diffusion between the network modifiers and the water, as well as hydration of the interfacial layer by breaking the weaker oxygen-cations bonds [179,180]. This results in the reorganization of the surface due to the removal of sodium and calcium with protons from the water being absorbed into the glass to balance the negative charge of the surface [154]. The composition of the surface varies with the time it has been in contact with the water due to the time dependent removal of Ca^{2+}, Na^{+}, and other network modifiers [178].

The second stages is the hydrolysis of the silica surface, which includes the breaking of the highest energy siloxane bonds and the removal of silica into solution [154]. Theoretically, this process would result in all elements being removed from the surface at an equal rate, termed congruent dissolution, but this does not occur in nuclear waste glasses based on the differences in the stability of the network forming elements, specifically silicon and boron [154]. The hydrolysis process has been investigated in detail for pure silica glasses using computational methods and is discussed in Section 4.4.2, with few investigations of the stability of mixed network former systems [167]. The initial hydrolysis rate depends on the temperature, pH, glass composition, and dissolved species in solution where the time required to reach the next stage of dissolution varies from seconds to days [154].

During the next step, there is a drop in the dissolution rate due to the formation of a protective surface layer which is an amorphous porous hydrated silica gel phase [154,178]. The drop in dissolution rate typically occurs which silica reaches a concentration of 1 mg/L in solution at ~350K [154] with the thickness of the gel varying with pH [181]. Though the exact process responsible for its generation is still discussed

in the literature, the silica gel appears to be the silica remnant of the initial glass structure with additional reorganization and some polymerization of silica species onto the surface from the saturated solution [178,182]. The role of this gel as either altering the chemical affinity of the surface or a passivating affect has been extremely contentious in literature with recent studies suggesting that both mechanisms occur increasing the complexity of the analysis [154]. The slowing of the dissolution rate is predicted to be the result of the formation of an oversaturation of silica in solution that limits further removal of SiO_4 tetrahedra from the silica backbone structure [179,183].

The properties of the interfacial gel layers is critical to the identification of the residual rate of glass dissolution since its existence results in a decrease in the dissolution rate compared to the rate of hydrolysis [154]. Several recent studies have implemented a suite of characterization methods including SIMS, TEM, SEM, EELS, ATP, and Raman spectroscopy to analyze the structure and properties of the interfacial layers developed during glass dissolution [26,184,184,185]. Generally, the investigation of the gel layer was accomplished through either elemental mapping of SON68 glass coupons [71,185], or used isotopically tagged elements to identify the diffusion and polymerization of surface features into the gel layer [184]. Details of the altered regions have been identified through the use of these high resolution characterization methods including the formation of a silica rich interfacial gel structure, the existence of multiple interfacial layers, the identification of silica gel thickness, the deposition of crystalline silicates on the surface, and the prediction of glass dissolution rates [26,71,184] . Decreases in the dissolution rate has been identified in the case of densification of the outer layers of the alteration layer, but how often densification naturally occurs is still

under investigation [186,187]. Overall, it has been established that the silicates in multicomponent glasses are more stable than the network modifiers (Ca, Na, Li) and other networker formers (B) while other components (Al) have similar stability to silicon, which varies with pH [186-190]. A more detailed discussion of the formation of the silica gel layer and the generation of comparable structure models are discussed in Chapter 5.

Once the hydrated gel layer has been formed, secondary precipitation phases start depositing on the surface, and silica dissolution slows to a residual rate [154,178]. During this period the interfacial structures continue to form and relax according to the Ostwald rule of stages, so that the alteration layers tend toward more thermodynamically stable crystalline phases [178].

There is the possibility of a final stage in the dissolution process during which there is a sudden increase in the reaction rate, which has been identified as the result of precipitation of crystallized zeolite phases and is related to changes in the pH and composition of the solution [154,154,178,188,189,191]. Why the dissolution rate suddenly increases and when it will occur is still being investigated requiring extensive analysis of longer range diffusion studies and a detailed understanding of how the formation of surface layers affects the dissolution process. Due to the complexities of the dissolution of nuclear waste glasses, a number of reviews are available [154,171,178,180,183] for additional information.

Computational analysis of the dissolution of these multicomponent glass systems is of interest to the scientific community since atomistic resolution in simulations is capable of identifying the reactions which are responsible for the evolution of the

structure with time, the stability of individual bonds, the effect of changing diffusion rates on soluble ions, and the development of precipitation phases. Several difficulties exist in the use of the previously discussed computational methods, primarily classical MD and DFT methods, on these systems.

In classical MD realistic potentials that are capable of simulating water-silica interfaces are currently under development, but the creation of potentials which can simulate water interactions with multicomponent glasses are still in the future, with only recent development of potentials for water-calcium-silicate systems [132,192], which does not include sodium, aluminum, or boron [26]. For non-hydrated structures most classical MD potentials do not include the ability to simulate systems with mixed glass formers due to competing mechanisms between the generation of three coordinated and four coordinated boron in borosilicates, with the addition of aluminum increasing the complexity of the required potential [193,194]. Several potentials have been developed to model multicomponent glasses, but thus far none include functionality for all six components required for the simulation of ISG compositions or water functionality [193-197]. Due to these difficulties simulations which do not require a potential can be used, either those which are more accurate and simulate smaller systems, such as DFT, or those which are less accurate but simulate larger systems, such as kinetic MC (KMC).

Since the composition and structure of multicomponent glass is complex, the small system sizes in DFT methods makes the analysis more difficult. For example, in a 300 atom simulation, multicomponent glasses may contain only 3-4 atoms of a certain type, limiting the possibility of phase separation affects and not providing sufficient statistics for comparison with experimental results. Some simulations of similarly

complex bioactive glass compositions may provide a framework for future studies [198-201].

What is more common is the use of KMC simulations, which are capable of describing the dissolution reactions of much larger simulations including the formation of interfacial gels and the interdiffusion of water [168]. KMC modeling uses a predetermined glass structure which evolves based on the probabilities of hydrolysis and dissolution reactions which are derived from the bonding environments of atoms, and are selected to be consistent with experimental trends [168]. KMC has been extremely useful in analyzing the dissolution process, especially in the case of long term studies, and has been extensively applied to the study of glass dissolution [95,168,188,202-206]. A full analysis of the current state of KMC modeling is outside the scope of this dissertation, but a recent review by Pierce et al. provides insight into the application of KMC to the dissolution of nuclear waste glasses [168]. Ultimately, the accuracy of these simulations depends heavily on the assumptions which are built into the model that can be improved through the use of more accurate classical MD or DFT models [183,188,206]. Also, KMC methods do not provide information on the mechanisms of glass dissolution that the atomistic simulation used in this work, instead focusing on the long term structural evolution.

1.5 Conclusions

A detailed and mechanistic understating of the processes which govern water-silica interactions are of interest due to the use of silica in a number of engineered and naturally occurring systems, such as geology, microelectronics, bioactive glasses, and

the vitrification of nuclear waste. Through extensive application of experimental methods, the structure and properties of the silicate glasses can be identified, although difficulties with the amorphous systems, the insulative nature of oxides, and the analysis of both solids and liquids continue to be a challenge. Through the use of atomistic computational methods, the processes which govern water-silica interactions can be characterized in detail, including the identification of reaction mechanisms and localized structure changes that would be difficult to analyze using experimental methods. Several features of the silica surface have already been identified including silanol concentration, the importance of surface silanol density, and the formation of structured water adjacent to fully hydroxylated surfaces. The reactivity of strained and unstrained Si-O bonds in silica have also been discussed as well as reactions with water molecules. Finally, the stages of multicomponent silica glass dissolution when in contact with water is included presenting some of the complexities and difficulties associated with the use of computational methods to analyze the dissolution process.

1.6 Purpose and Dissertation Layout

While computational analysis of water-silica surface has been undertaken since the 1980s, several barriers to the investigation exist including limitations in classical MD potentials, accessible systems sizes and time frames, and limited studies on the structure of silica surfaces, such as silanol concentrations, and activation energies for the breaking of Si-O bonds. Recent advances in computational methods, such as the development of dissociative water potentials [85,98,101], baseline studies on the stability of siloxane bonds [93,94,105,153], and the formation of hydrogen bonding

water network in water adjacent to silica surface [134,135], have allowed for the further analysis of the water-silica interface beyond interactions between water molecules and flat, unhydroxylated surfaces. In this dissertation, the structure of water-silica interfaces and the reaction mechanisms are analyzed to investigate the effect of complex surface formations and the existence of interfacial phases on the water-silica systems.

In Chapter 3, complex nanoporous silica structure models that represent the complexities in realistic nanoporous silica systems are examined during their reaction with water. This provides insight into how the internal surfaces of nanoporous silica affect the reaction mechanisms between water and silica systems, specifically in an analysis of the changing reactivity of strained silica bonds. The complex hydrated nanoporous silica systems introduces a number of different sites for water-silica reactions, and comparison of the changing structure provides an opportunity to validate the classical MD potential ReaxFF for use in the analysis of the dissolution of silica in water.

In Chapter 4, a detailed analysis of the accuracy of dissociative water-silica potentials in their application to water-silica systems is investigated since an understanding of inconsistencies between the less accurate but more efficient classical MD potentials and the more accurate but slower DFT methods is required before larger simulations can be performed. Once the classical MD simulation has been validated for use in hydrated nanoporous silica systems two new structures were created representing intermediate phases of glass dissolutions, can be analyzed.

In Chapter 5, the development of silica gel models is explored including the comparison between structures developed from dense silica and those from the silica-

rich remnant of multicomponent silicate glasses. The silica gels are analyzed and then input into a three-component model consisting of dense silica, silica gel, and bulk water, and high temperature evolution of the structure was performed. From these systems, changes in the silica, gel, and water regions of the system can be evaluated and the differences in localized features, intermediate range structures, and silica speciation in water are identified. The result is a complex multiphase model which highlights how the inclusion of an interfacial silica gel in dissolution model changes the analysis of the water-silica interface.

CHAPTER 2

COMPUTATIONAL METHODOLOGY

2.1 Abstract

The use of simulations to perform investigations of material properties and structures has surged in recent years due to improvements in computational efficiency and the ability to investigate a variety of systems with increasingly accurate methods. In this chapter, two of the most important methods that have been used throughout this dissertation, are also the commonly implemented atomistic simulation methods: classical molecular dynamics (MD) simulations and first principles density functional theory (DFT) method. Additionally, structural analysis (bond angles, bond distances), dynamic properties (diffusion coefficients and activation energies), and the calculation of partial atomic charges are also discussed. Future chapters will refer to the information included in this chapter.

2.2 Introduction

The basis of the simulation methods which are in use today were developed over the last century with the creation of quantum and classical mechanical methods of describing interatomic forces. It was not until the advent of the computer in the last fifty years when it became practical to perform these calculations on relatively large system sizes. Even so, the application of computational methods to amorphous materials started even later, in the 1970s. This was because interatomic potentials had been developed for a variety of liquids and crystalline solids, but had not yet been extended

to the formation of the tetrahedral structure commonly found in glasses [207]. Interest in performing simulations of amorphous materials was significant due to the ability to investigate not just the structure of glasses, but the development of density of state functions and to provide benchmarks for glass characterization [207].

Many simulation methods are available and encompass length scales, from angstroms (10^{-10}m) to nanometers (10^{-9}m) to meters, from femtoseconds (10^{-15}s) to nanoseconds (10^{-9}s) to seconds. Each of these regimes provide different information about the material system. In this work, atomistic simulations are employed, that include length scales from 10Å to 1nm and time scales up to the nanosecond range, these efforts include systems sizes as small as two atoms up to 1,000,000 atoms or larger.

In the next sections, the two most common atomistic simulation methods are discussed in more detail. They are: classical MD that relies on a user generated forcefield to describe the interatomic forces and DFT that solves the Schrödinger equation to calculate the electronic structure, from which properties of the system can be identified.

The reader should note that a number of other atomistic simulation methods are available including Monte-Carlo (MC) simulations which is a stochastic method of accepting and rejecting atomic movement, *ab initio* simulations which uses the Hartree-Fock method to calculate the electronic structure, and a variety of semi-empirical methods, which include the use of empirical data to improve the approximations used in *ab initio* simulations, among other [92].

2.3 Classical Molecular Dynamics (MD)

Classical MD is one of the most commonly implemented atomistic simulation methods to investigate the changing properties of materials with time, pressure, temperature and composition. They were first performed by Alder and Wainwright in the late 1950s to simulate the force between two hard spheres [208,209]. Since then, improvements in both the algorithms and the tools used to perform calculations have occurred. With current computational efficiency, MD simulations can be performed with as many as a tens of millions of atoms [210] for microseconds. This is far beyond what can be done using more accurate electronic structure methods such as DFT. The efficiency of classical MD methods relies on the use of forcefields to describe interatomic interactions, rather than calculating the forces from the electronic structure of the individual atoms. Each atom is then treated as one unit, without differentiating between electrons and the nuclei. Therefore, the accuracy of the results are heavily dependent on the development and parameterization of a forcefield, and each atomic interaction needs to be explicitly included in the potential. Forcefields are often fitted with a mixture of experimental and *ab initio* data depending on what is available. For instance, experiments can provide macroscopic properties (density, mechanical properties) for a variety of crystal polymorphs while highly accurate DFT methods can provide bond distance and bond angle information.

The development of classical MD potentials for glassy structures can be complicated by its non-equilibrium nature, and that perhaps using crystalline polymorphs for fitting amorphous potential parameters will result in unrealistic structures in the model. Previous studies have found that, even if a forcefield is fitted almost

exclusively to crystalline parameters and designed to simulate silica polymorphs, is still capable of generating a realistic amorphous structure [151]. This is due to the commonly used melt and quench procedure to generate computational models of amorphous materials, and allows for the formation of short range structures while the fast cooling rates (which are exacerbated by short simulation times) ensure a lack of long range order.

Ultimately, the development of accurate forcefields is often considered to be an art, rather than a science, and a discussion of the forcefields used in this work as well as a brief description of how classical MD simulations are performed is included.

2.3.1 MD Algorithm – Equation of Motion

In classical MD simulations, the dynamics of the system are calculated using classical Newtonian mechanics; therefore, the particles obey Newton's well-known equation of motion:

$$-\frac{dV}{d\vec{r}} = m\frac{d^2\vec{r}}{dt^2} \qquad \text{Eq. 0-1}$$

In Eq. 0-1, m is the mass of the atom, t is time, V is the potential energy at a given atomic position r, where the r vector contains the atomic coordinates for all the particles in the system. The change in the potential energy with the r vector can be rewritten as a force.

In order to calculate the changing position of the particles with time, a Taylor series expansion is used (Eq. 0-2):

$$\vec{r}_{t+1} = r_i + \frac{dr}{dt}(\Delta t) + \frac{1}{2}\frac{d^2r}{dt^2}(\Delta t)^2 + \cdots \qquad \text{Eq. 0-2}$$

By using the particles' position at time t and t-1, the position of the particles at t+1 can be obtained directly from the potential (V), as is seen in Eq. 0-3, where F is the force and a is the acceleration:

$$a = \frac{F}{m} = -\frac{1}{m}\frac{dV}{dr} \qquad \text{Eq. 0-3}$$

The above method of identifying atomic positions is referred to as the Verlet algorithm which is used to solve Newton's equations of motion numerically. At each time step, the forces allow the system to evolve with time. As the size of the time step decreases the approximation made by the Verlet algorithm improves, so that the smaller the time step the more accurate the simulation. Therefore, selection of the time step used is critical to ensuring an accurate simulation. Concerns with the Verlet algorithm include the generation of truncation errors which arise from using finite precision when large differences in positions are being considered. One improvement was the development of the leap-frog algorithm, which implements a half-time step (½Δt) and explicitly states the velocity, an advantage when temperature and energy are being controlled. The equation for the velocity and position of the atoms in a leap-frog integrator are included in Eq. 0-4 and Eq. 0-5 respectively:

$$r_{t+\frac{1}{2}} = r_t + v_{t+\frac{1}{2}}\Delta t \qquad \text{Eq. 0-4}$$

$$v_{t+\frac{1}{2}} = v_{t-\frac{1}{2}} + a\Delta t \qquad \text{Eq. 0-5}$$

One critical issue with the leap-frog algorithm is seen in the above equations with the velocity (v) and the position (r) being out of phase by ½Δt. This error can be removed by reformatting Eq. 0-4 and Eq. 0-5 into the most commonly used integration algorithm, the velocity Verlet algorithm:

$$r_{t+1} = r_t + v_t\Delta t + \frac{1}{2}a_t\Delta t^2 \quad \text{Eq. 0-6}$$

$$v_{t+1} = v_t + \frac{1}{2}(a_t + a_{t+1})\Delta t \quad \text{Eq. 0-7}$$

In the Eq. 0-6 and Eq. 0-7, the velocity and position of the particles are in phase with each other, and the velocity values are explicitly stated allowing for adjustments of the particles speed for temperature control.

2.3.2 Potentials and Forcefields

The interatomic forces of the atoms in classical MD simulations are controlled almost exclusively by user parameterized forcefields which describe the potential energy formed between different atomic pairs. Hundreds of potentials have been developed over time to identify specific aspects of selected systems, since no one potential which describes all interatomic relationships has been identified. In the following sections two of the classical MD forcefields used in this work are discussed, a Buckingham based silica potential as well as a dissociative bond-order based potential, ReaxFF.

2.3.2.1 Buckingham Potential – Silica

One of the common silica potentials uses a Buckingham form of interatomic potential which was first proposed in 1938 for application in gaseous systems [211]. The original Buckingham potential has the form of Eq. 0-8, which characteristically implements an exponential decay to describe the repulsive force and an r^{-6} term to describe the attractive forces [211]:

$$\Phi_{12}(r) = Aexp(-Br) - \frac{C}{r^6} \quad \text{Eq. 0-8}$$

In Eq. 0-8, A, B, and C are coefficients which are parameterized based on the systems composition, and r is the interatomic distance.

Modern application of the Buckingham potential include an additional term to describe the Columbic interactions which accounts for differences in atomic charge:

$$\Phi_{12}(r) = \frac{q_i q_j e^2}{4\pi\varepsilon r} + Aexp(-Br) - \frac{C}{r^6} \quad \text{Eq. 0-9}$$

In Eq. 0-9, q_i and q_j are partial charges of atomic species i and atomic species j respectively. The parameters were fitted against crystalline silicates and hydroxides. Parameterization of the forcefield for the silica systems is discussed in detail in Reference [86].

2.3.3 Reactive Forcefield (ReaxFF)

A primary concern with the use of classical MD forcefields is that they require an extensive knowledge of the system including structural details and interaction energies, and typically do not allow for the simulations of reactions. This issue arises from the inability to differentiate atomic species in various bonding environments and the use of fixed charges to describe columbic interactions of atoms undergoing chemical reactions.

In 2001 Adri van Duin and coworkers developed a more complex forcefield, which is estimated to provide efficiency close to classical MD while providing DFT or *ab initio* quality results [82,97]. While the underlying concept for ReaxFF is the same as a classical MD potential, the complexity is increased to allow for the simulation of properties with higher accuracy. The full equation for the forcefield is seen in Eq. 0-10 with descriptions of

each term included in Table 0-1. Functional forms of each term is included in Reference [97]. The ReaxFF potential is bond order based, and allows for a changing number of atomic bonds based on the interatomic distances. By implementing a continuous function to describe the bond order and bond energy, the transition from one bonding state to another does not cause step-wise changes in the system energy. The gradual transition in bonding state and order allows for reactions to occur without explicitly including their description in the forcefield itself. There is a small decrease in the efficiency of the simulation due to the inclusion of additional terms in the energy calculation, but efficiencies are still 1000x higher than DFT simulations.

$$E_{system} = E_{bond} + E_{over} + E_{under} + E_{val} + E_{pen} + E_{tors} + E_{conj} + E_{vdWaals} + E_{coulomb} \quad \text{Eq. 0-10}$$

Table 0-1: Description of energy terms for ReaxFF system energies. [97]

E_{bond}	Bond order energy identified through interatomic distances
E_{over}	Energy penalty with over coordination
E_{under}	Accounts for energy contribution from pi-electron resonance on under bonded atoms
E_{val}	Ensures that energy from valance angle terms approaches zero as the bond order approaches zero
E_{pen}	Energy penalty for incorrect valence angles due to overcoordination or under coordination
E_{tors}	Ensures that the energy from the torsion angle approaches zero as the bond order approaches zero
E_{conj}	Contribution of conjugation effects to the energy
$E_{vdWaals}$	Applied to all atom pairs and account for long range interactions, as well as short range repulsive interactions

$E_{coulomb}$	Applied to all atomic pairs to calculate energies short range interactions, including atomic shielding at low interatomic distances

2.3.4 Statistical Ensembles

During the course of a classical MD simulation it is often advantageous to control one or more thermodynamic parameters of the simulation, in order to test the response of the structure to changing temperature, pressure, enthalpy and other conditions. Since each atom in a simulation will behave slightly differently, and each snapshot includes different microstates of the system, the collection of all of these configurations is referred to as an ensemble [212]. In order to control an ensemble, external constraints are imposed on the system so that different properties can be analyzed.

One of the most common ensembles is the micro-canonical or NVE ensemble. The NVE ensemble controls the number of atoms in the simulation (N), the volume of the simulation cell (V), and the energy (E), and typically represents an equilibrium systems [212].

The canonical or NVT ensemble, is similar to the NVE ensemble, with the exception that the temperature (T) is controlled in addition to the number of atoms (N) and the volume (V) of the simulation cell. It is one of the most common ensembles and allows for an analysis of the system with increasing or decreasing temperature.

The isothermal-isobaric ensemble (NPT) is often used to identify the density of the system since it allows for expansion or contraction of the simulation cell in order to standardize the external pressure. Simulations performed using the NPT ensemble will often experience “breathing” or an oscillation of the cell parameters around a set value as the simulation continually corrects the cell size in an attempt to maintain a constant

pressure. NPT simulations can be difficult to control due to the application of both a thermostat and a barostat, and incorrect selection of thermostat/barostat parameters can result in unstable simulations.

Typically, a mixture of these ensembles are used over the course of a simulation, targeting the analysis of specific material properties.

2.3.5 Classical MD Codes

Over the last several years a number of different classical MD codes have been developed to run atomistic simulations on high performance parallel computers. In this work, two different classical MD codes are used. The first is the DL_POLY 4.0 code, which was originally developed at Daresbury Laboratory by W. Smith, T.R. Forester, and I.T. Todorov [213].

The second classical MD code used is LAMMPS (Large-scale Atomic/molecular Massively Parallel Simulator) which was developed and is distributed by Sandia National Laboratories [214]. It contains potentials for a number of solid-state materials and, due to its distribution as an open-source code, contains extensive functionality and the ability to be easily modified.

2.4 Density Functional Theory (DFT)

The advent of DFT methods began in the 1920s as physics began to develop the equations which describe the electronic structure of the atom from which the interatomic forces can be calculated. During the next 60 years, a number of crucial approximations allowed for the relatively efficient calculation of the electronic structure leading to the

formation of modern DFT methods. The theoretical background required to fully understand DFT simulations is significant, and only a brief overview of the methods is included. For a more exhaustive description the reader is directed to several books on the topic, References [92,212,215].

2.4.1 The Schrödinger Equation

The basis of quantum mechanical simulation methods is the Schrödinger equation since it can provide information on the electronic structure of the system from which the structure and properties of the material can be derived. The Schrödinger equation consists of a Hamiltonian operator (H), which describes the inter particle interaction, the wave function (Ψ), and the energy (E) of the current system configuration:

$$H\Psi(r) = E\Psi(r) \qquad \text{Eq. 0-11}$$

By solving Eq. 0-11, variation in the wave function with time is identified, the square of which gives the probability of an electron occurring at a position (r) at a set time (t) [92]. The Schrödinger equation can only be solved completely for one electron systems, such as hydrogen atoms or H_2^+ molecules, and for more complex systems, a number of approximations are used to facilitate the calculations [92].

2.4.2 The Born-Oppenheimer Approximation

The Born-Oppenheimer approximation was first introduced in 1927, and is one of the cornerstones of quantum mechanics. The Born-Oppenheimer approximation states that it is possible to separate the coordinates of the electrons and nuclei in the system

so that the wave function can be solved with only a single set of coordinates to streamline the calculation. The separation of the nuclear and electronic wave function is justified through the mass differences between the nuclei and the electrons. Since the electrons are much lighter, they also move much faster so that the nuclei can be considered stationary in comparison.

Through iteratively solving the Schrödinger equation for different r values using the Born-Oppenheimer approximation, a potential energy surface can be identified. It is along this potential energy surface that the nuclei move, which is separate from the movement of the electrons (though the path of the electron density tends to follow the movement of the nuclei) [92].

2.4.3 Hartree-Fock Equations and the Slater Determinant

The Hartree-Fock equations introduce a simplification of the complex dynamics of electrons in a molecular system through the implementation of an independent particle model. An independent particle model simplifies the interactions between individual particles (atoms) by averaging over all the interactions in a system. In this model, each electron is described as an orbital where the total wave function is a product of all the individual orbitals. Since the electrons in the system are identical, the total wave function is antisymmetric and does not change when two electrons are exchanged. Therefore, a Slater determinant can be constructed, which consists of single electron wave functions at different electron coordinates. To derive the Hartree-Fock equation, the energy of a single Slater determinant is identified by diagonalization of the matrix so as to minimize the vibrational energy of the system. Once the energy of

the system is minimized a Fock operator is identified, which describes the electron-electron repulsion, and electron-nuclei attraction. The Fock operator only accounts for the variation in the total energy, rather than the total energy of the system. Further simplification of the Fock operator through the use of Lagrange multiplies and simplification of the Fock operator results in the Hartree-Fock equations in terms of molecular orbitals (Eq. 0-12):

$$F_i\phi_i' = \varepsilon_i\phi_i' \qquad \text{Eq. 0-12}$$

2.4.4 Kohn-Sham Equation

One of the foundational concepts in DFT methods is the use of orbitals, which was first suggested in Kohn-Sham theory. The Kohn-Sham model is similar to the Hartree-Fock method, and the formulas which describe the kinetic, electron-nuclear and Coulombic electron-electron energies are the same. The major change is that the electronic kinetic energy is split into two parts: one which is the same as the Hartree-Fock energy, and a smaller second term. The justification for this is that the electrons in the orbitals are non-interacting, therefore the Schrödinger equation can be solved exactly through the use of the Slater determinant to describe the molecular orbitals and an exact kinetic energy functional. To introduce energy associated with the electron-electron interactions, a second exchange-correlation term is introduced.

2.4.5 Exchange-correlation Functionals

Up to this point all the discussion of the computational methods for solving the Schrödinger equation have been consistent across nearly all *ab initio* simulation methods. The use of the Kohn-Sham method is able to reproduce 99% of the atomic

energy of a system assuming that a sufficiently large basis set has been selected. Since in the Kohn-Sham method the electron-electron interactions are averaged over the system, there is an extra electron exchange and correlation energy which must be accounted for. This last 1% of the energy can be critical in properly identifying the properties of the system, and several different methods have been developed to improve this approximation. The reader should note that though it is possible to calculate the exchange energy and correlation energy separately it is more efficient and common to combine them into an exchange-correlation functional [212].

2.4.5.1 Local density approximation

The local density approximation (LDA) is the simplest method of approximating the value of the exchange-correlation functional. In this form, the electron density around a point is assumed to be that of a uniform electron gas. Therefore, the interactions between the energy and a background electron density is calculated, rather than needing to calculate the interaction between each individual pair of electrons. LDA's tend to be effective in systems where the charge density changes slowly over in the structure, such as in simple metals and covalent systems [212].

A slightly more advanced form of the LDA approximation is the Local Spin Density Approximation (LSDA) which adds in a spin based component. For closed shell systems (where the electrons are forcibly pared in an electron orbital), the LDA and LSDA approximation are the same. In practice, LSDA is used more often than the LDA approximation, and some common versions include the VWN and PW LSDA exchange-correlation functionals [92].

2.4.5.2 Generalized gradient approximations

The Generalized Gradient Approximations (GGA) implement a gradient in the electron density rather than assuming a uniform electron density. GGAs are especially effective in systems where there is significant variation in the electronic density surrounding an atom. Typically, the use of a GGA results in increased accuracy of the simulation. The PBE (Perdew-Burke-Ernzerhof) GGA is a very popular exchange-correlation functional which is used in this work [216]. Another well used GGA-hybrid functional is the BLYP (Becker-Lee-Yang-Parr) versions which consists of an exchange functional by Becke [217] combined with a correlation functional from Lee-Yang-Parr [218].

2.4.6 Basis Sets

All *ab initio* methods implement a basis set which is used to expand an unknown molecular orbital value into a set of known and well described functions. This makes solving the Kohn-Sham equations more straight-forward. In theory, expanding a basis set to infinity would result in a complete basis set, which would be capable of exactly describing a molecular orbital. In practice a finite basis must be used with a smaller basis set resulting in lower accuracy and higher efficiency, and vice versa. Additionally, the form of the basis function is critical since a more accurate form of the basis requires fewer functions to gain a certain level of accuracy.

2.4.6.1 Gaussian Basis Function

Gaussian basis functions are among the most commonly used basis sets. They have the functional form:

$$\chi_{\zeta,l_x,l_y,l_z}(x,y,z) = Nx^{l_x}y^{l_y}z^{l_z}e^{-\zeta r^2} \quad \text{Eq. 0-13}$$

With $l_x+l_y+l_z$ determining the type of the orbital and the r^2 dependence as the primary features of Gaussian type orbitals. The r^2 dependence can result in a rapid falling off of the atomic orbital as the distance increases, and as a result, a higher number of basis sets are required than for other basis functions. Even so, calculations which use Gaussian type orbitals are efficient, and are therefore one of the most commonly used basis functions for calculating electronic structures.

For basis set size, a doubling of all basis functions can be introduced by developing a double zeta (DZ) basis by placing a 2 in front of the zeta (ζ) which is present in the Eq. 0-13. This allows for multiple functions to describe a single electron. So, for example, in a minimum or single zeta (SZ) basis set, a hydrogen atom is described by a single function to describe the s orbital. In the DZ basis set, the number of functions has doubled to two (1s and 1s'). For a triple zeta (TZ) basis set, the number of functions is tripled compared to the minimum basis set and so on.

Polarization functions can also be added to account for higher angular moment functions. This allows for the electron distribution to be correlated with other nearby orbitals, and increases the accuracy of the simulations. Basis set size selection can have a significant impact on the results and efficiencies of the calculations. To large of a basis set can impede the ability to perform the simulation while too small and the results

are not accurate. In the majority of the work performed here, a double zeta potential (DZP) is used.

2.4.6.2 Plane waves as basis functions

Due to the localization of the Gaussian type basis sets discussed above, when periodic systems are simulated, the Gaussian basis sets must be extended to infinity, and the convergence to a discrete value is computationally expensive. Therefore, it is common to implement plane wave basis functions as a method of efficiently introducing periodicity into the system. The free electron behavior of the valence electrons in metals inspired the use of a free electron form of a basis function. The Schrödinger equation can be expanded as a set of complex exponents or sine and cosine functions in Eq. 0-14 and Eq. 0-15 respectively.

$$\phi(x) = Ae^{ikx} + Be^{-ikx} \qquad \text{Eq. 0-14}$$

$$\phi(x) = Acos(kx) + Bsin(kx) \qquad \text{Eq. 0-15}$$

In an infinite space, the wave functions form bands, which can be described as a set of expanded orbitals with a plane wave basis, Eq. 0-16:

$$\chi_k(r) = e^{ik\cdot r} \qquad \text{Eq. 0-16}$$

In the above equation, the value of k varies similarly to the value of ζ in the Gaussian type orbitals previously discussed. The selection of k dictates how many basis functions are generated with a higher k-value increasing the number of plane waves. An energy cut-off value of 200eV with 0.01eV k vector spacing is common and generates ~20,000 basis functions, far more than will be used in a calculation with Gaussian type orbitals. The number of plane waves generated depends almost exclusively on the size of the

cell and the plane wave cut-off distance, and that the complexity of the system inside the simulation cell does not have a significant effect.

Plane wave basis have difficulties with the simulation of core electrons since it requires a large number of highly oscillating functions to adequately describe the interactions. This issue has been addressed with the implementation of pseudopotentials, described later in this chapter.

2.4.6.3 Gaussian plane wave (GPW) basis

The Gaussian plane wave (GPW) basis consists of both Gaussian and plane wave type orbitals. In essence, a set of Gaussian basis sets are used to describe the localized wave functions and electron density, and then a set of plane wave basis describes the longer range interactions [219]. The use of plane waves for a portion of the basis allows for more efficient calculation of the density as well as the more natural inclusion of periodic boundary conditions. Due to efficient treatment of the periodic boundary, the GPW method is recommended for the use in the simulation of large dense systems including liquids and solids [219]. Further developments in the use of GPW methods have allowed for the development of an augmented-plane-wave (GAPW) methods which allows for all electron calculations. Recent work by VandeVondele and coworkers has demonstrated the use of the GPW method for the simulation of liquid water as well as oxide systems [78,219].

The GPW basis implemented as the QUICKSTEP method in the CP2K code which is a multi-use atomistic code developed by European and Pacific Northwest

National Lab (PNNL) researchers that includes a variety of functionality across atomistic simulation methods [220].

2.4.7 Pseudopotentials

Pseudopotentials (also referred to as effective core potentials) have been implemented to explicitly describe the behavior of core electrons that differs heavily from valence electrons. Previous methods of simulating electrons (Gaussian and plane wave basis) can break down when applied to the core electrons. They also provide a method of introducing relativistic effects for the core electrons without increasing the computational cost. The selection of pseudopotentials is especially critical in the simulation of high atomic number elements with a large number of core electrons that can affect the results of the simulation.

In simulations which use Gaussian type basis sets, Gaussian functions are typically used to describe the pseudopotentials. Since these functions are continuous it is unnecessary to fix a position at which the core potential is being implemented, and instead it is the number of electrons which are represented by the pseudopotential which dictates it size and accuracy. For instance, an all electron calculation describes all the electrons in the system explicitly while a small core calculation will include all the valence electrons plus one level deeper into the core of the electron.

For plane wave basis sets, the pseudopotential smears out the modeling of the core electrons so that a high number of plane waves is not required for the simulation. A core radius is typically selected which varies with atomic type, and the potential for the electrons inside the core regions varies according to a selected function [92]. The first

and second derivatives of the pseudo wave function must match with the selected reference wave function for the calculation to run successfully without generating discontinuities in the plane wave basis. The size of the valence region determines the hardness or softness of the potential with a small core region corresponding with a hard pseudopotential. There are a number of different pseudopotential schemes available including norm-conserving, ultra-soft, and the frozen core approximations [92].

2.4.7.1 Projector augmented wave (PAW) method

The projector augmented wave (PAW) method is commonly considered to be a type of pseudopotential although it still describes all of the core electrons rather than smearing them out. The PAW can be written as a function with a valence term expanded into a plane wave basis, and in the core region the values are predicted based on a grid. The energy contributed from the core region is the difference between the all-electron atomic orbitals and the value introduced by the expansion of the valence term into the core region. Theoretically, this is an improvement over the pseudopotential methods althrough very few direct comparisons have been performed [92].

The PAW method is implemented in the Vienna Ab initio simulation package (VASP), a plane wave based density functional theory code to perform electronic structure calculations and quantum-mechanical molecular dynamics distributed by the University of Vienna [221].

2.5 Analysis Methods

Throughout the work performed here a number of different analysis methods are used to both analyze the changes in the structure of the system with time, as well as to validate the results against available experimental data. The details of these commonly implemented analysis methods are discussed.

2.5.1 Structural Analysis

Structural analysis methods are a key component of evaluating amorphous silica structure models and include the compilation of different bond lengths, bond angles, and longer range structural features, such as the formation of silica ring structures. In amorphous systems, there is a significant variation in interatomic distances and bond angles, especially compared to the crystalline systems. Therefore, variations need to be averaged over a large number of snapshots of the systems to account for vibrational affects and to represent the variations in the structure. To gain the appropriate statistics, thousands of snapshots from a single simulation are analyzed and compiled to provide accurate results.

2.5.1.1 Pair Distribution Functions (PDF)

Bond lengths are analyzed in radial distribution functions (RDF) and pair distribution functions (PDF), the first being a complication of all the interatomic distances in the system and the latter being the individual sets of interatomic distances (Si-O, O-O, Si-Si). For each frame of the simulation, the bond lengths are analyzed and then averaged to provide a distribution. Examples of PDF data for a dense silica system

are in Figure 0-1. The integration of the first peak in the PDF provides the coordination number in the first coordination shell, or alternatively the number of nearest neighbors. Unlike in crystalline systems, the PDF for amorphous systems has shorter and broader peaks as distance increases indicating the loss of long range order.

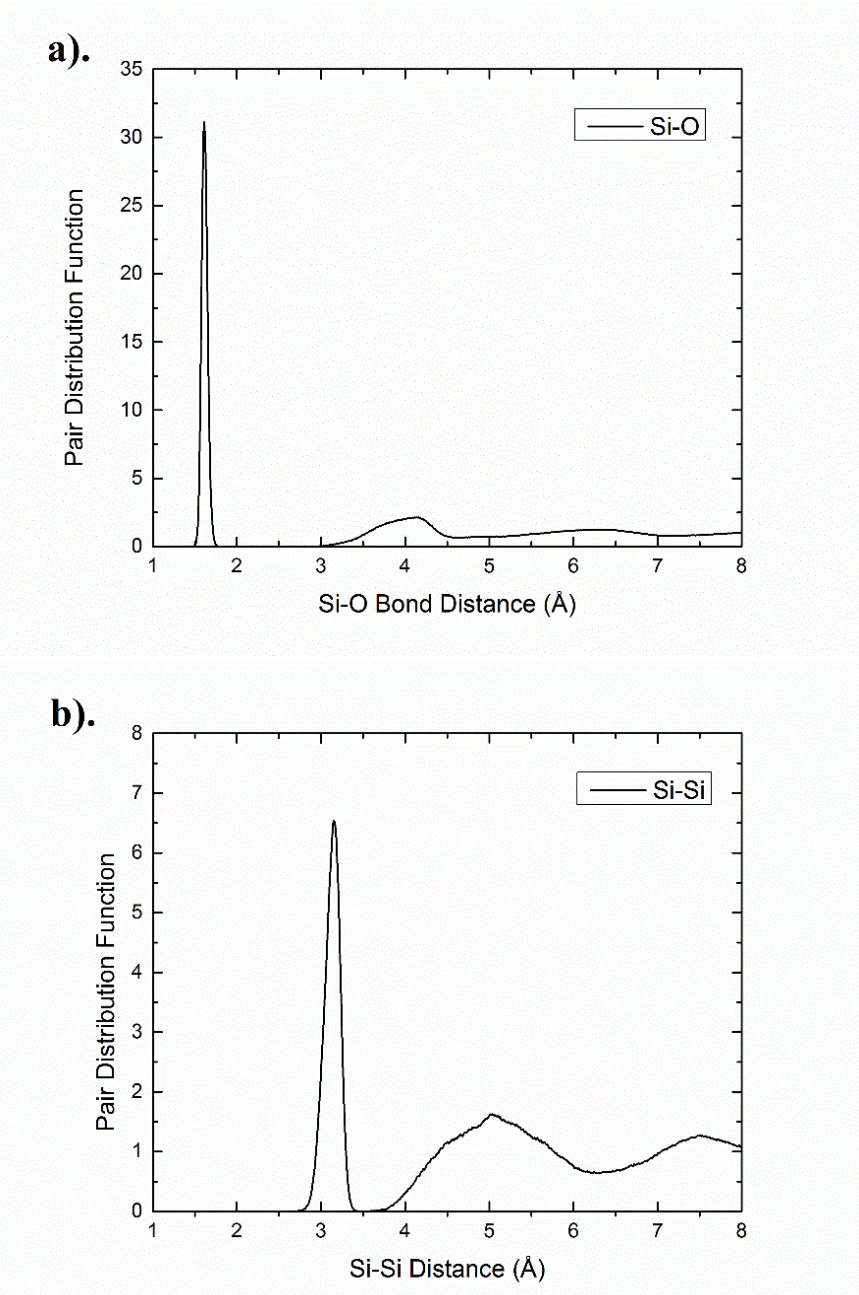

Figure 0-1: (a) Si-O and (b) Si-Si PDF for a 3000 atom dense silica model simulated at 300K using classical MD simulations.

2.5.1.2 Bond angle distribution (BAD) functions

Bond angles are analyzed in bond angle distribution (BAD) functions, which are averaged over a large number of snapshots in order to compile a distribution of bond angles that account for variations due to temperature and the amorphous structure. An important component of bond angles is the selection of a cut-off radius, to identify which angles should be included in the analysis. Based on the Si-O bond lengths the value of 2.25 Å is selected, which falls in the first minimum after the main Si-O peak in the PDF data. This ensures that all of the first nearest-neighbors in the SiO_4 tetrahedron are included. Examples of BAD data for a dense silica glass system are included in Figure 0-2.

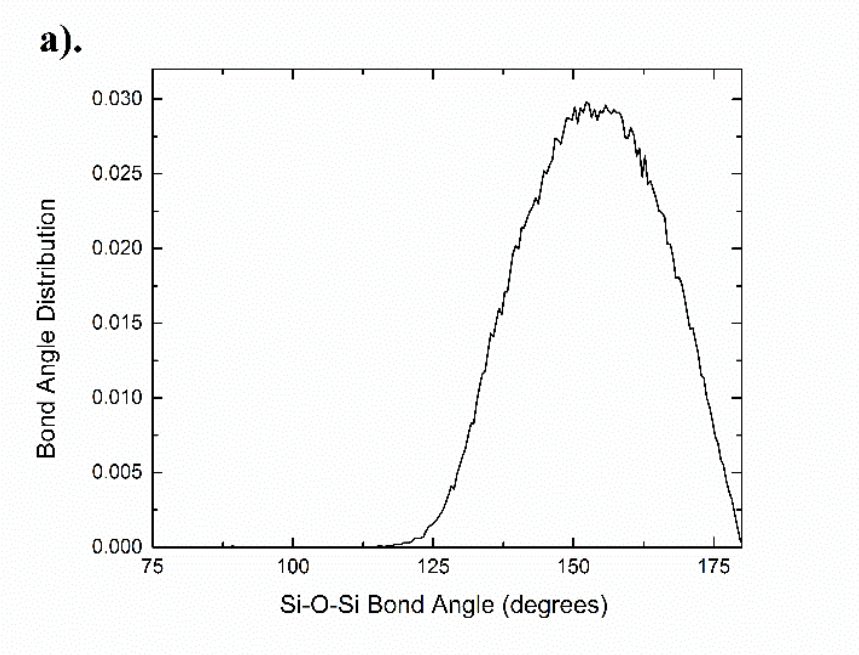

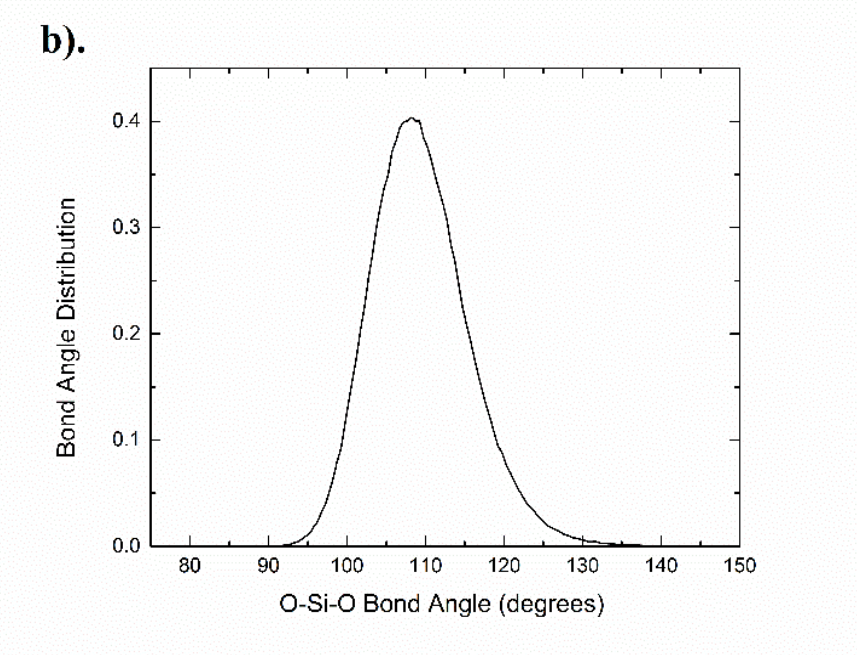

Figure 0-2: (a) Si-O-Si and (b) O-Si-O BAD for 3000 atom dense silica models simulated at 300K using classical MD simulations.

2.5.1.3 Q_n distributions

For amorphous systems the evaluation of the Q_n speciation of the network formers is used to describe the connectivity of the amorphous structure. The “n” in the Q_n represent the number of bridging oxygen which are attached to a selected network former, primarily silicon [222]. Therefore, a perfect silica structure would consist of 100% Q_4 species. When the number of network modifiers increases the silica structure fragments, increasing the concentration of Q_3 (silicon bonded to three bridging oxygens), Q_2 (silicon bonded to two bridging oxygens), and so on.

A compilation of the Q_n distribution is called the connectivity. Connectivity is calculated using Eq. 0-17, where C is the connectivity, n is the number of bridging oxygen associated with a network former, and Q_n is the proportion of the Q_n species. A

perfectly connected structure would have a connectivity of 4.0, with decreasing connectivity with increased network modifier concentration or porosity [222].

$$C = \sum_{n=1}^{1} n * Q_n \qquad \text{Eq. 0-17}$$

2.5.1.4 Ring size distributions

The previous analysis methods which have been discussed focused on short range structural features, bond lengths, bond angles, and Q_n distribution. Another metric is used to analyze the medium range structure of amorphous system is the ring size distribution. A ring is noted by the number of network formers which are included in the smallest complete ring that can be formed, so that when stepping from one network former to the next, it is possible to return to the original position in the system [223]. Ring structures occur in both amorphous and crystalline systems that consist of tetrahedral structures. The distribution of ring sizes is typically centered on six for dense silica, since it is a derivative of other silicate polymorphs, with ring sizes as small as three or as large as the system size will allow. An even smaller two-membered ring can form due to a set of edge sharing SiO_4 tetrahedron and is discussed in future chapters. A representative ring size distribution for a dense silica simulation is included in Figure 0-3.

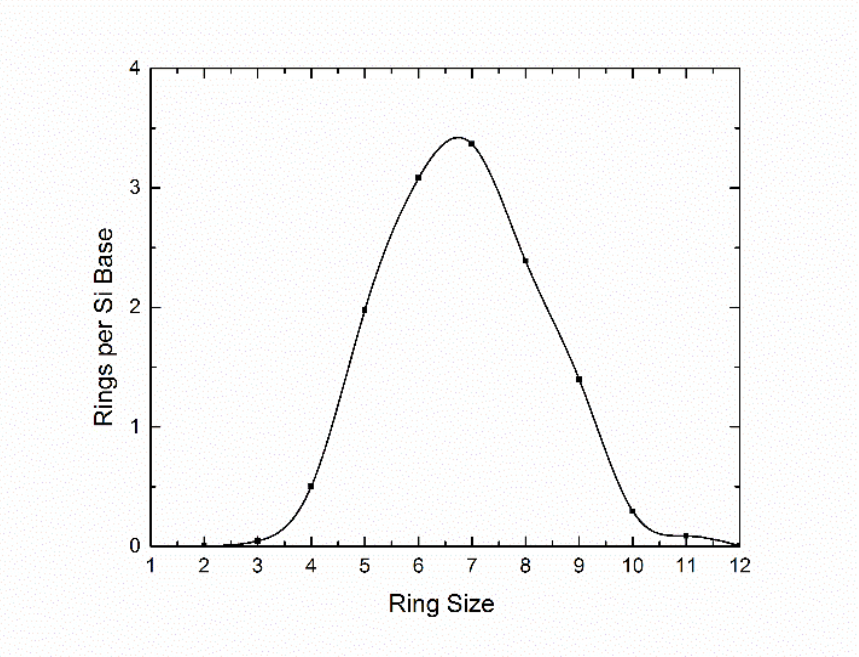

Figure 0-3: Ring size distribution for a 3000 atom dense silica model from classical MD simulation.

2.5.2 Diffusion Analysis

Throughout this work, information on dynamic properties of the systems are also introduced. One of the primary metrics used to analyze the movement of atoms through a network is the diffusion coefficient. Diffusion coefficients are calculated through the compilation of mean square displacement (MSD) data from an equilibrium structure simulated over long time frames, typically no less than 30ps in length. The MSD of each atom is calculated by Eq. 0-18 [224]:

$$MSD = \langle |n_i(0) - n_i(t)|^2 \rangle \qquad \text{Eq. 0-18}$$

Where n is the position of particle i, $n_i(0)$ and $n_i(t)$ are the positions of particle at time 0 and time t, respectively [224]. The derivative of the MSD data with time is used to

calculate the diffusion coefficient through the Einstein diffusion equation (Eq. 0-19) which describes random-walk diffusion in a three-dimensional crystal [225]:

$$D = \frac{1}{6} \lim_{t \to \infty} \frac{d}{dt} MSD \qquad \text{Eq. 0-19}$$

The 1/6 coefficient removes the redundancy in the degrees of freedom since the MSD data includes forward and backward movement in each of the three dimensions (x, y, and z). The limit as time approaches infinity is critical as atoms will go through three different diffusion stages. The first is the ballistic region, where the MSD is proportional to time squared [226]. The next region is the cross over region, where the MSD is independent of time [226]. The final region is the diffusion region, and occurs when the MSD is proportional to time [226]. The difference in diffusion regions is particularly apparent when the logarithm of the MSD with time is plotted. Representative plots of the mean squared displacement (MSD) data with time is included in Figure 0-4 for hydrogen atoms in water, to demonstrate the change in the diffusion regimes with time.

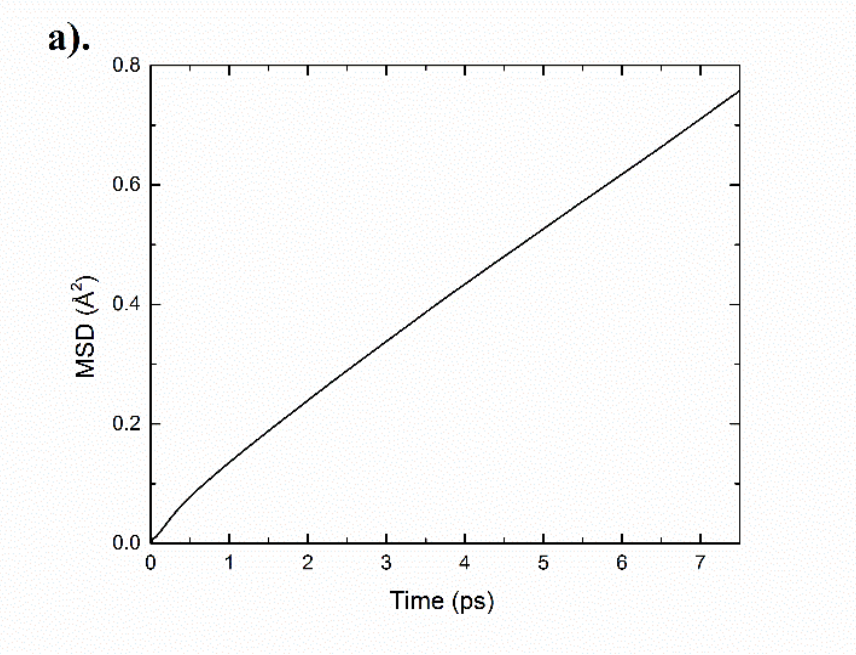

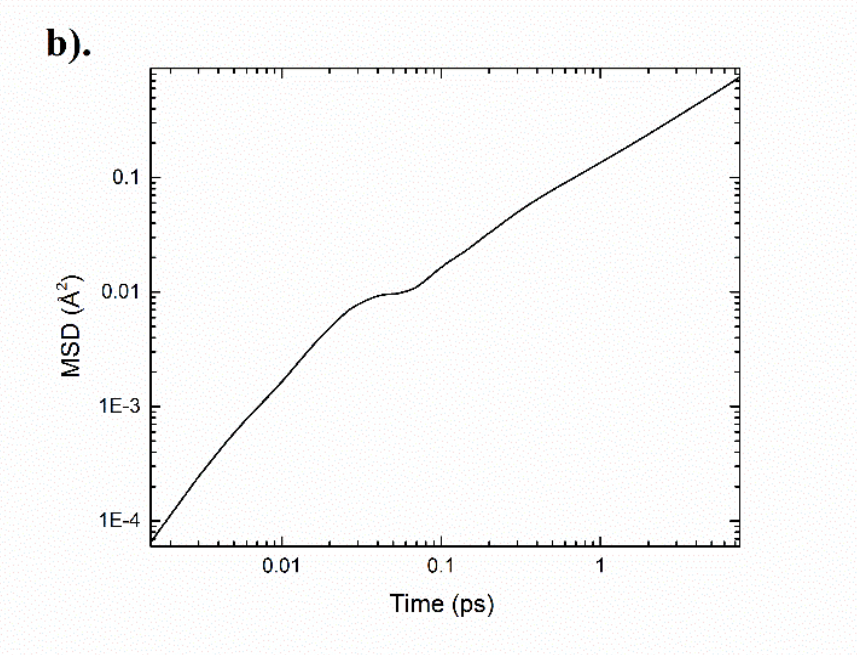

Figure 0-4: (a) Linear and (b) logarithmic MSD for hydrogen ions in a 6000 atom bulk water model at 300K using the ReaxFF classical MD potential.

Diffusion coefficients are sensitive to temperature variations in the material. The effect of temperature is described by the Arrhenius equation (Eq. 0-20):

$$D = D_o \exp\left(-\frac{E_a}{RT}\right) \qquad \text{Eq. 0-20}$$

Where D_o is a pre-exponential factor, E_a is the activation energy, R is the gas constant, T is the temperature, and D is the diffusion coefficient [225]. By taking the logarithm of both sides of the equation there is a linear relationship between the diffusion coefficient and the inverse of the temperature, given in Eq. 0-21 [225]:

$$\ln(D) = \ln(D_o) - \frac{E_a}{RT} \qquad \text{Eq. 0-21}$$

The activation energy is commonly used to indicate which species in the material system has the lowest energy barrier for diffusion and which ions in a solid are mobile.

2.5.3 Population Analysis Methods

Using population analysis methods the partial atomic charge of the individual atoms in a DFT simulation can be identified since information on the electronic structure is already calculated. It is worth noting that calculation of partial atomic charges cannot typically be performed with classical MD potentials since many of them implement fixed charges. There are a number of ways to partition the atomic orbitals and assign their electrons to different atomic nuclei. The most straightforward method is to use the atomic orbitals, which contain the individual electronic density contributions. All the atomic orbitals associated with a selected nuclei can be summed to identify the electron density. In some cases, an atomic orbital may be associated with more than one nuclei; therefore a method of separating out how much of an atomic orbital is assigned to each nuclei is necessary. In the case of Mulliken charge analysis any atomic orbitals which is assigned to more than one atom have their electron density split between the two evenly [227,228]. There are a few natural issues with arise with this method, since it does not consider the electronic negativities of the atoms involved nor their bonding state. In recent years, additional schematics have been developed for identifying partial atomic charges, including Hirshfeld, Atoms-in-Molecules, and Natural Atomic Orbital population analysis methods [92,229,230]. A description of these methods and their application to boron-carbides can be found in Reference [231].

2.5.4 Standard Error

Unlike crystalline systems, amorphous systems can experience significant variation in the results due to their inconsistent long range order. Variation in properties

can occur in any property based on the medium and long range structure of the systems, including mechanical properties, density, and diffusion coefficients. To account for this variation, it is common to perform the simulations several times with different starting structures and report the data in terms of the average value plus a standard deviation or a standard error term (mean ± standard error). In this work, the standard error is used most often to represent data from three different simulations, and deviation in this protocol are noted when they occur. The method for calculating standard error is included in Eq. 0-22 with SE as the standard error, s as the standard deviation, and n as the number of unique simulations.

$$SE = \frac{s}{\sqrt{n}} \qquad \text{Eq. 0-22}$$

2.6 Summary

Two of the most common atomistic simulation methods currently used to study the structure and properties of materials, classical MD and DFT, were discussed in detail. This includes a description of the underlying classical or quantum mechanics which govern the forces responsible performing the calculations. Additionally, several of the analysis methods used in this work were discussed, including structural analysis methods, diffusion coefficients and activation energies as well the calculation of partial atomic charges.

CHAPTER 3

AB INITIO MOLECULAR DYNAMIC SIMULATIONS OF THE HYDROXYLATION OF NANOPOROUS SILICA[1]

3.1 Abstract

Accurate details of water-silica interactions is critical to understanding the mechanical properties and long-term durability of silica and silicate glasses. In this chapter, interactions of water and nanoporous silica models were investigated using *ab initio* molecular dynamic (AIMD) simulations with density functional theory (DFT) was employed to accurately describe the surface reactions. AIMD simulations up to 30ps were performed for hydrated nanoporous silica systems with porosities between 31% and 67%. Complete hydroxylation of coordination defects was observed while some ring structure defects, including two-membered (2-Ring defects) and three-membered rings (3-Ring defects), remained stable within the simulation duration of 30 ps. The limited removal of 2-Ring defects is due to the inaccessibility of the reaction sites and the increased stability of rings located on concave surfaces. The first stage of the 2-Ring removal mechanism the formation of an intermediate over-coordinated silica (Si^5) defect, continued to persist throughout the simulations indicating that there is thermodynamic drive for 2-Ring defect removal which is kinetically limited.

[1] Chapter 3 is based on the publication Rimsza, J. M., and Jincheng Du. "Ab initio Molecular Dynamics Simulations of the Hydroxylation of Nanoporous Silica." *Journal of the American Ceramic Society* 98.12 (2015): 3748-3757, with permission from John Wiley & Sons.

3.2 Introduction

The interactions between silica and water occur in a variety of natural systems and have numerous applications in both science and technology. For instance, water-silica interactions are considered to be the cause of weakening in silicate minerals, as well as in pure silica or silicate glasses [5,122]. The stress corrosion of glasses also determines the long-term mechanical properties of the material, due to the chemical reaction of water with silicate glasses crack tips. Understanding silica and silicate glass-water interactions is also critical in evaluating the stability of vitrified nuclear waste materials, since the durability of the borosilicate glass host is paramount for the immobilization of nuclear waste [26,168,178,232]. A detailed mechanistic understanding of the water-silica interactions can lead to more accurate predication of the behaviors of vitrified nuclear wastes during geological storage.

Water-silica reactions are based on the breakage of siloxane linkages and the formation of silanol groups is described by Eq. 0-1 [88]:

$$Si - O - Si + H_2O \rightarrow Si - OH + HO - Si \qquad \text{Eq. 0-1}$$

The energy barrier for the above reaction depends on the number of bridging oxygens which are attached to the silicon as well as the stress state of the siloxane bond. At a crack tip, where the Si-O bonds are under stress, the energy barrier is lowered. A similarly stressed Si-O bond exists in 2-Ring defects which occur on freshly fractured surfaces and are a set of edge sharing SiO_4 tetrahedron. Therefore, short range and longer range structural features including bridging oxygen concentration and ring structure affect the reactivity of the silica surface.

Experimental and computational methods have been used to investigate the activation energies for silica dissolution in aqueous environments. Work by Icehnhower and Dove investigated changing dissolution rates of quartz at different temperatures and suggested activation energies of 74.5±1.4 kJ/mole (0.77ev) for Si-O bond breakage through experimental reaction kinetics [159]. The 0.77eV energy barrier is consistent with other experimental work indicating activation energies between 60.9-89.0 kJ/mole (0.63-0.92eV) [159]. Extensive computational work by Kagan et al. implemented classical molecular dynamic (MD) simulations to look at the dissolution of a silica surface and separated the reaction rate by changing Qn species, with n as the number of bridging oxygen atoms associated with a silicon [88]. The limiting step in silica dissolution, as reported by Kagan et al., are the $Q_3 \rightarrow Q_2$ and $Q_2 \rightarrow Q_1$ steps, both of which have an energy barrier of 14 kcal/mole (0.61eV) [88]. In comparison the $Q_1 \rightarrow Q_0$ and $Q_4 \rightarrow Q_3$ transitions have lower energy barriers of 13 kcal/mole (0.56eV) or 11 kcal/mole (0.48/eV) respectively [88]. Due to the added strain associated with the 2-Ring defect, it is expected that energy barriers for their removal is lower [81].

2-Ring defects have been identified experimentally using both SIMS (secondary ion mass spectroscopy) [118,121] and ^{29}Si DAS (dynamic angle spinning) NMR (nuclear magnetic resonance) [65,138]. Investigation of the hydroxylation of 2-Ring defects was performed by D'Souza and Pantano by fracturing silica rods in ultra-high vacuum conditions so that the dangling oxygen bonds and undercoordinated silica form the 2-Ring defects [121]. Two hydroxylation rates were identified to describe the hydroxylation and de-hydroxylation behavior of fractured silica glass surfaces. The first reaction was governed by first-order kinetics with reaction times too fast to be analyzed, but were

theorized to be the annihilation of 2-Ring defects [121]. In comparison, the second stage of the reaction was much slower, and believed to be the removal of 3-Ring defects from the system [121]. The 3-Ring defects are expected to be more stable than the 2-Ring defects since they have a less constrained Si-O-Si bond angle of 127^{o} by ^{29}Si DAS NMR compared to 90^{o} for the Si-O-Si bond angle in 2-Ring defects [65]. Despite the results reported by D'Souza and Pantano for the hydroxylation of 3-Ring defects, the same techniques and methods cannot probe the reaction mechanisms and reaction rates for 2-Ring removal, indicating the important role that computational methods can play in investigating silica hydroxylation.

In addition to the above experimental investigations of silica hydroxylation both classical and first-principles atomistic simulations have been widely used to investigate water-silica reactions. The simulations complement the experimental work since the complexity of the bulk amorphous structure, the short time-frames of the reactions, and the limited methods available to quantify the different reactants and products of the reaction makes water-silica reactions challenging to identify. Classical MD forcefields capable of describing these interactions have been under development by Garofalini and colleagues starting in the early 1990s [233,234] and continuing until the present [88]. Additionally, Fogarty et al. parameterized the ReaxFF forcefield developed by van Duin et al. to investigate water-silica reactions including the identification of extensive proton transport as a critical feature in reaction pathways [82,85,97]. Even with the development of classical MD methods which are capable of simulating water-silica reactions, they need to be carefully benchmarked against more accurate simulations. Thus, DFT based methods provide reaction mechanisms for water-silica surfaces which

can be incorporated into the parametrization of classical MD codes. The ever increasing computational efficiency of the DFT algorithms and computing power also make it possible to perform AIMD simulations with hundreds of atoms and the inclusion of bulk surfaces. Interactions between silica surfaces and water have been studied using both classical MD [86,90,91,233] and DFT methods [105,106,110,135,152] as well as investigations of nanoconfined water [89] and hydrophobic surfaces [107]. Even so, long term simulation of water-silica interactions using AIMD methods is still missing in the literature. These results provide valuable mechanistic information on water interactions and provides model data for classical MD simulations.

Despite the wide number of computational studies performed on this topic, the detailed reaction mechanism for Si-O bond breakage is relatively unstudied, especially in the case where the reaction is naturally allowed to develop [152]. For example, Du and Cormack artificially formed silanol bonds and then measured the formation energy, Kagan et al. placed water molecules in an ideal configuration to cause siloxane bond breakage, and Tilocca and Cormack positioned water molecules adjacent to 2-Rings to facilitate reactions in Carr-Parrinello molecular dynamic simulations of 45S5 bio glass [86,88,198]. An exception is work by Du et al. who used mixed quantum mechanical and molecular mechanical (QM/MM) simulations to investigate the natural hydroxylation process on silica surfaces [105,106]. The results indicate that the portion of the surface which is treated with quantum mechanical methods can affect the results with increasing quantum mechanical treatment lowering activation energies, especially compared to cluster calculations [106]. Selective placement of water molecules and the

implementation of constrained dynamics facilitate the reactions, but few studies investigate the direct dynamics of water-silica interactions.

In this chapter the interactions between water and nanoporous silica were investigated through the use of AIMD simulations. The natural reaction pathways involved in Si-O bond breakage and the effect of porosity on the water-silica behavior is identified. Additionally, the hydroxylation process and structural and electronic changes along the reaction pathways are studied in detail.

3.3 Simulation Details

To investigate the interactions between porous silica and water, two simulation methods were used, classical MD with effective partial charge empirical potentials and DFT based AIMD simulations. Nanoporous silica models were created with classical MD methods and the DFT simulations were used to study the water-silica dynamics. The classical MD simulations were implemented in the DLPOLY 2.20 code [213], and DFT simulations of the water-silica interactions used a Gaussian localized basis set in periodic DFT based AIMD simulations in the CP2K code [219]. Previous work on aqueous systems using CP2K has indicated that it provides accurate descriptions for insulating and aqueous systems [78].

3.3.1 Nanoporous Silica Structure Generation

For this project, a method of generating nanoporous silica structures which mimic CVD (chemical vapor deposition) derived nanoporous silica was used. A 99 atom system was chosen to allow for sufficient variability in the amorphous structure while still

being small enough to allow for computational intensive AIMD simulation in the subsequent investigation of water-silica interactions.

First, a 99 atom bulk silica structure was created through a melt and quench procedure where a random mixture of 33 silicon atoms and 66 oxygen atoms were heated to 5000K. The systems were then cooled in a step wise fashion by 500K every 120ps. Alternating NVT (canonical) and NVE (microcanonical) ensembles were used. Ensembles describe which elements of the simulation are controlled, whether that is the number (N) or the atoms, the volume (V), the temperature (T), the energy (E), or the pressure (P). Implementation of alternating ensembles allows for the regulation of the temperature to cause system cooling and then removing the temperature restriction so that the simulation can equalize.

Once the dense silica glass has been created, volume needs to be introduced to create pores. A series of linear lattice expansions were performed, in serial, to generate the porous structures. A four step procedure for generating the nanoporous silica structure is included below.

First, the 99 atom dense silica structure (ρ=2.2 g/cm^3, A=B=C=11.44Å) underwent a linear lattice expansions by 20% in all three dimensions, resulting in silica system with a volume of 1798Å^3 (A=B=C=12.16Å). All the Si-O bonds are broken during the expansion and the SiO_4 tetrahedron were expanded.

Next, the newly expanded silica system undergoes 30,000 steps of relaxation with a 1 fs time step in a NVT ensemble. The temperature is held constant at 300K with a Nose-Hoover thermostat. This allows for all of the atoms in the structure to rearrange themselves and recreate the SiO_4 tetrahedra.

After the relaxation of the system the porosity is now scattered throughout the structure, rather than all located in one region of the cell. At this point, the porosity of the system is ~20%. To generate a structure with a higher porosity the nanoporous silica model undergoes another linear lattice expansion, introducing additional free space into the system and increasing the porosity. The process of expansion and relaxation is performed iteratively until the desired porosity is reached.

Finally, once the porosity of the nanoporous silica structure has been finalized an additional simulation with an isothermal-isobaric (NPT) ensemble is performed, allowing for control of the pressure (P) through the use of a Nose-Hoover thermostat and barostat resulting in a chancing simulation cell size and a constant temperature. NPT simulations remove the negative pressure regions in the nanoporous silica models to create a structure at a thermo-mechanical equilibrium. The resulting nanoporous silica systems have porosities between 30%-70% and densities between 0.74-1.53 g/cm^3. In order to account for the variation in both the amorphous silica structure as well as the added porosity all simulations were performed in triplicate, and error bars are typically equal to the standard deviation or the standard error of the three values. The standard error is the standard deviation divided by the square root of the number of measurements.

Even though the silica systems used here are only ~100 atoms, the same method has been previously performed on much larger systems (~3000 atoms) with success, and it is expected that the same method used for the larger systems will produce similar structures in these systems. Additional information on the system,

including bond angles, bond distances, ring size analysis, and mechanical properties performed on the 3000 atom systems is included in Reference [235].

Due to the complex internal surface area present in the nanoporous silica structures, a series of flat surfaces were generated to provide a control for the complex internal geometries that were studied.

To create a flat surface a dense silica structure was cut in two by extension of the periodic boundary conditions in the z-direction. Through the insertion of 10Å of vacuum space the system was essentially cleaved in half, creating the flat surface. Five unique surfaces were generated and underwent relaxation using the same DFT methods discussed in Section 3.3.2 to remove any high energy sites before water was added to the system.

3.3.2 Water-Nanoporous Silica Interactions

Once the nanoporous silica structures at the selected porosities (30%, 40%, 50%, 60%, and 70%) were generated, water was introduced into the pore volume through the following process.

First, a simulation cell of pure water with dimensions of 50Åx50Åx50Å was generated. Then, the water box was overlaid with the nanoporous silica system. Finally, any water molecules which were outside the nanoporous silica simulation box were removed, as were any water molecules within 1Å of the nanoporous silica structure. Snapshots of the resulting hydrated nanoporous silica structure are included as Figure 0-1.

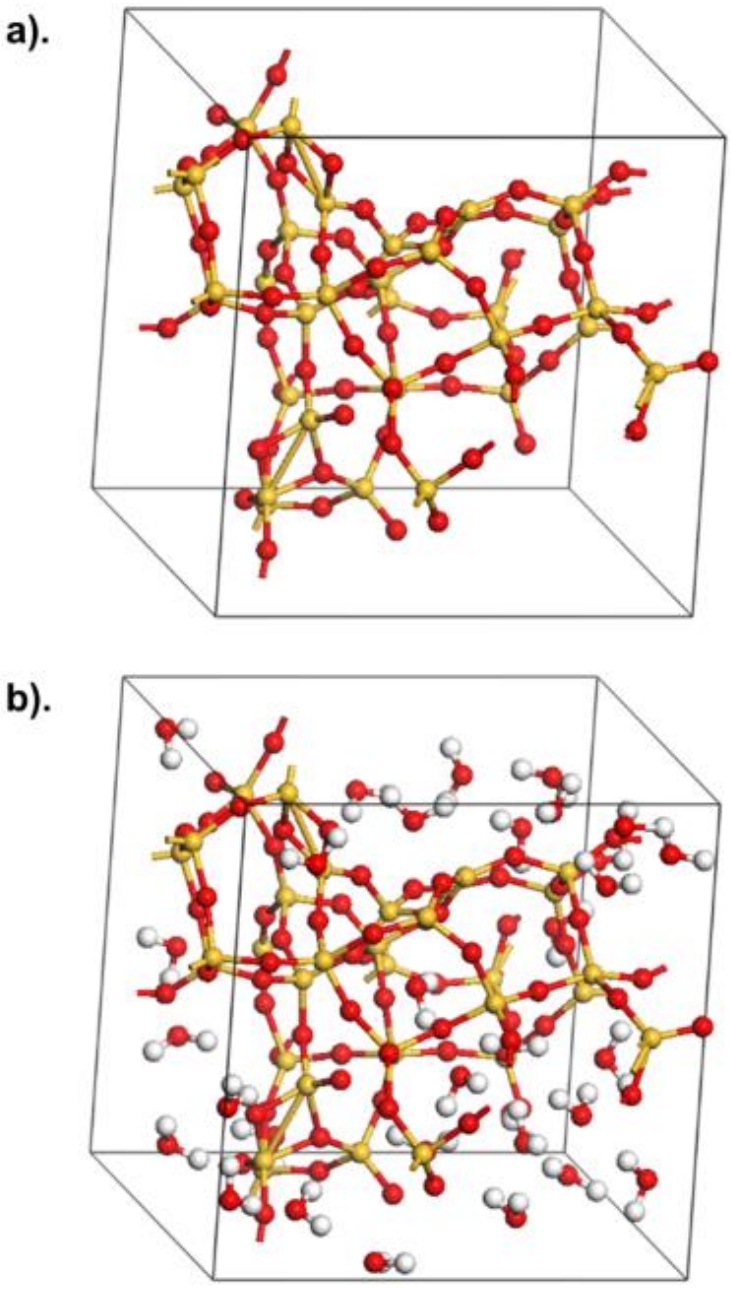

Figure 0-1: Snapshot of the 42% nanoporous silica systems (a) unhydrated and (b) hydrated. O:red, Si:yellow, H:white.

Due to the increasing volume of the porosity in the systems, more water molecules were added to the higher porosity nanoporous silica systems. A table of the number of added

water molecules and the porosities of the nanoporous silica systems are included as Table 0-1.

Table 0-1: Changing number of water molecules and systems sizes with increasing porosity in hydrated nanoporous silica systems

Porosity	31%	42%	52%	60%	67%
Water Molecules	20±2	30±1	47±2	66±3	85±3
Total System Size (atoms)	159±5	189±2	241±5	298±10	354±10

For the initial relaxation of the hydrated nanoporous silica structures a DFT geometry optimization was performed for 500 steps, which removed the high energy strained sites which were developed through the introduction of water to the system. Following the geometry optimization, a DFT AIMD run was performed for 30ps. The AIMD runs were performed at 300K which was controlled through a Nosé-Hoover thermostat in an NVT ensemble. Periodic bound conditions were employed with a DZVP basis set and a BLYP generalized gradient approximation which was implemented in the CP2K simulation package [220]. For more information on basis sets, exchange correlation functionals, and the CP2K code, please refer to (Chapter 2).

3.4 Results

3.4.1 Water-Silica Reaction Mechanisms

The use of the first principles simulation methods in this work provided an opportunity to investigate detailed reaction mechanisms which are responsible for the Si-O bond breakage which governs silica dissolution.

The coordination defects which are present in unreacted silica have the highest energy in the system, and are therefore removed from the surfaces first. These defects include non-bridging oxygens (oxygen bonded to only one silicon), three bonded oxygens (oxygen bonded to three silicon), under bonded silicons (silicon atoms bonded to only three oxygen), and over bonded silicons (silicon atoms bonded to five oxygen). Snapshot of the under bonded silicon (Si^3) and non-bridging oxygen (NBO) defects are included in Figure 0-2. These defects were removed during the first 500 steps of geometry optimization and replaced with silanol (Si-OH) groups. In the case of the NBO, a nearby water molecule donates a hydrogen to form the silanol, leaving a remaining OH^- to undergo limited diffusion before receiving a proton via hydrogen hopping to reform a water molecule. For the case of an under bonded silicon, an OH^- group from a water molecule bonds with the Si^3 defect to form a silanol group, and the extra H^+ ion is free to move through the system via proton transfer to either become a H_3O^+ molecule, or terminate a NBO defect. The reader should note that when the proton is transferred through the water it is through successive hydrogen transfers from one water molecule to the other, and is not due to the movement of one hydrogen through the solvent. The result is an extremely rapid relative diffusion of hydrogen atoms through the structure compared to bulk water diffusion [85].

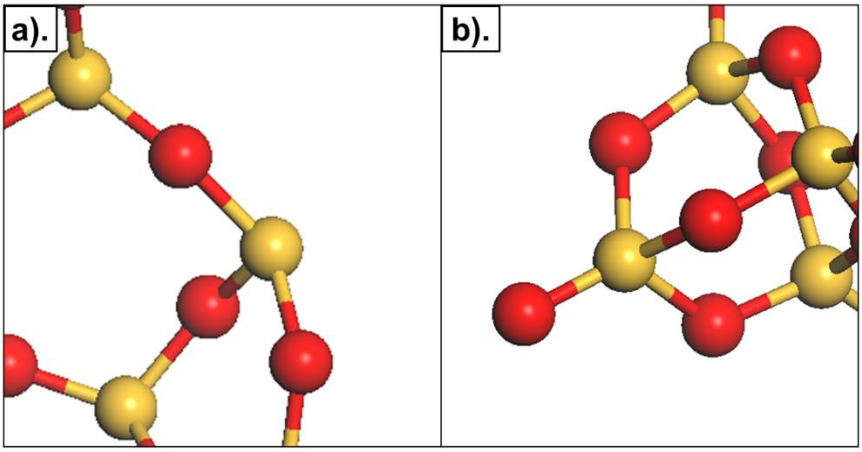

Figure 0-2: Snapshots of (a) a Si^3 defect and (b) a NBO defect. Si:yellow and O:red.

2-Ring and 3-Ring defects are also formed on the internal surface areas of the pores. The defects are named by the number of silicon present in the ring structure. A snapshot of a 2-Ring defect is included in Figure 0-3.a. The mechanism of 2-Ring defect removal is complicated since it requires the breakage of a Si-O bond and forms two additional defects, a NBO and Si^3. Additionally, the interplay between two or more water molecules, plus the accessibility of reaction sites, has a significant impact on the reactivity. Previous work by Masini and Bernasconi used DFT to suggest the existence of two distinct reaction mechanisms for 2-Ring defect removal on flat surfaces [152]. During the first reaction mechanism a water molecule is absorbed onto a silicon resulting in the formation of a temporary Si^5 defect, after which the Si-O bond breaks [152]. In the second, the hydrogen in a water molecule absorbs onto one of the bridging oxygens in the 2-Ring structure [152]. Even though the second mechanism, the absorption of the water molecule onto the bridging oxygen, has a lower activation energy of 0.32eV, the first Si^5 based reaction mechanisms has a lower initial energy barrier of 0.11eV for the absorption of the water onto the silicon atom [152]. The total

energy barrier for the removal of the 2-Ring defect from the Si^5 based mechanism has total activation energy of 1.1eV [152]. In addition, the Si^5 based reaction mechanism is more commonly reported in both DFT and classical MD based simulations, including work by Kagan and Garofalini, and Du et al., among others [88,93,105].

In the AIMD simulations performed here, only the second 2-Ring breakage mechanism was identified. The reaction steps are as follows:

1. Approach and orientation of the water molecule on the 2-Ring defect site (Figure 0-3.a). This requires the site to be accessible to the water molecule and may be affected by the position of the 2-Ring defect structure in the system.
2. Absorption of the water molecule onto one of the silicon in the 2-Ring defect (Figure 0-3.b). The Si^5 defect is stable for ~0.1-0.2ps. The stability of these defect sites is variable, and they can be formed at any point during the simulation.
3. One of the hydrogens on the absorbed water molecule breaks away, leaving an Si^5 defect connected to four bridging oxygens and one silanol group (Figure 0-3.c).
4. Opening of the 2-Ring defect resulting in the formation of a NBO defect (Figure 0-3.d). This reaction occurs almost simultaneously with the removal of the hydrogen from the absorbed water molecule.
5. Termination of the NBO defect through proton transport from the solution (Figure 0-3.e). It is worth noting that the extra hydrogen which terminates the NBO is not one of the hydrogen atoms from the initial absorbed water molecule, but has

been generated through the reaction of a different water molecule with a defect elsewhere in the system.

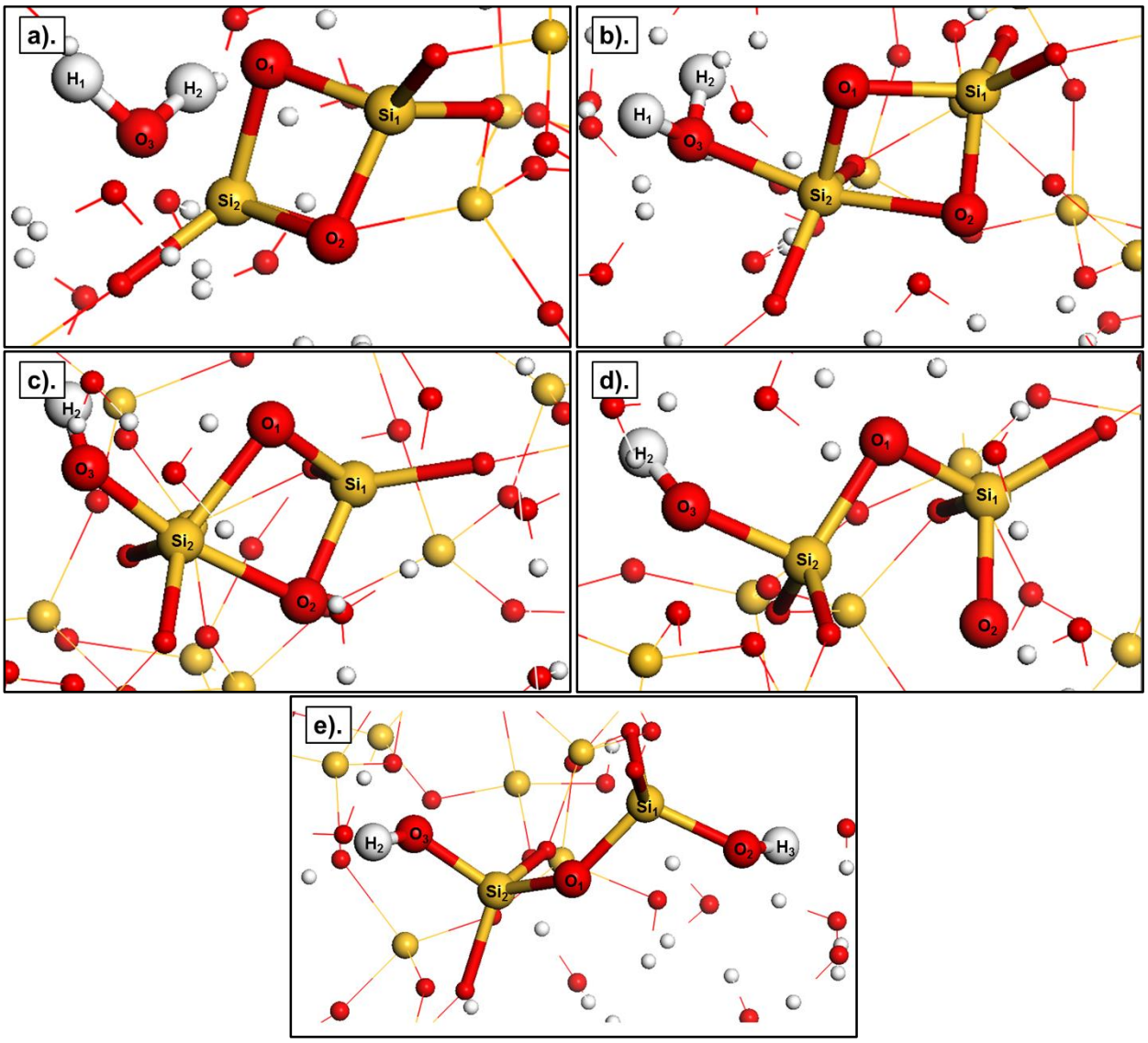

Figure 0-3: Snapshots of the five representative steps of the mechanisms of 2-Ring bond breakage in a 60% nanoporous silica system in the presence of water. Si:yellow, O:red, H:white.

The flat silica surfaces do not exhibit any 2-Ring bond breakage and instead, all of the rings which occur on the surface survive the 30ps AIMD simulation. The lack of 2-Ring defect removal is consistent with experimental reaction rates suggested by

D'Souza and Pantano with an additional strain rate added to account for the 2-Ring structures [118,121]. Due to the short simulation time, the experimental reaction rate predicts that an average of $3*10^{-10}$ Si-O bonds should be broken in these simulations [118]. This suggests that the opening of the 2-Ring defect in the porous systems is unusual, and that a significant amount of strain is introduced due to the 2-Ring structure. Additional analysis of the reaction rates derived from changing silanol concentrations are included in Section 3.4.4.

3.4.2 Atomic Charge Transfer

Partial charge analysis of the individual atoms involved in the 2-Ring defect bond scission mechanism is critical to understanding the reactions which governed Si-O bond breakage in different environments. There is limited information on charge transfer during the hydroxylation reaction available in the literature due to the use of classical MD simulations, rather than more accurate DFT simulation methods, to perform the calculation. Since classical MD simulations typically use fixed charges, there is no changing charge states to analyze. The partial atomic charge information which is available is focused on the analysis of silanol structures in localized clusters, such as SiO_4H_4 (orthosilic acid), the orientation of water molecules, and hydrogen bond formation [236,237].

The most complete analysis of the reaction has been performed by Du et al., who investigated the role of proton transfer between hydronium ions, rather than the charge of the NBO and Si^3 defects formed during the reaction [105]. Even so, DFT computational studies identified charge transfer between silanol groups and adjacent

water molecules [105]. Additionally, Bredas et al. found that even slight changes in the geometry of the system results in significant changes in the atomic charge densities, which highlights that once charge is introduced to the system it is almost instantaneously transferred throughout the system [238].

To investigate the partial atomic charges, a Mulliken population analysis was performed for three different trajectories along the 2-Ring defect breakage reaction steps. Details on the Mulliken population analysis method is included in Section 2.5.3.

For the following data on partial atomic charges all atom names are referenced to the images in Figure 0-3. One aspect of the reaction which should be noted is that two of the hydrogen atoms, H_1 and H_3 are not included in the entire reaction. H_1 diffuses away from the silica surface after step 2, and H_3 only becomes a part of the opened 2-Ring when it terminates the NBO during step 5. Therefore, fluctuations in the H_1 and H_3 charges after they leave the reaction site should not be considered. All of the changing partial atomic charges for the silicon, hydrogen, and oxygen atoms in the reaction are included in

Table 0-2 and Figure 0-4. Charge values for different atoms are averaged over three equivalent reactions.

The silicon atoms in the reaction experience a loss in electronic charge (a less negative charge) between reaction step 1 and 2 when a Si^5 defect is formed as seen in Table 0-3. The difference in the Si_1 and Si_2 charges is not as extreme as the less negative charge between the silicon in the network structure between the same steps indicating it is not the change in the bulk silica structure which is responsible for the changing charge (Table 0-2 and Figure 0-4.a). The less negative charge of the network

silica between steps 1 and 2 is due to the removal of coordination defects elsewhere in the structure during the same time frame that the reaction is taking place. After the initial change in the charge of the silica its charge is constant for the remainder of the reaction, indicating that after step 1 its charge is stable. In the 2-Ring structure the less negative charge in the Si_1 and Si_2 during step 2 is balanced by a more negative charge of the associated bridging oxygen (O_1 and O_2) resulting in a 0.929 net charge of the 2-Ring structure in step 1 and a charge of 0.926 in step 2, seen in

Table 0-3. During the first two steps of the reaction the charge of the water molecule also become less negative from -0.060 at step 1 to 0.106 at step 2 (

Table 0-3). The change in the charge suggests that the interaction of the water molecule with the 2-Ring structure results in transfer of electrons into the silica structure during the formation of the Si^5 defect by a water molecule. Charge transfer from the water to a 2-Ring structure was also noted in previous work by Du et al. using QM/MM simulations [105]. The charge transfer has an effect on both the oxygen and the hydrogen that make up the water molecule with a more negative charge of ~0.05 for all the three atoms (Figure 0-4.b and Figure 0-4.c).

After the initial charge transfer between the water molecule and the 2-Ring defect during step 2, the charge of the system is constant until the formation of the NBO in step 4. The formation of the NBO causes a more negative charge of the silicon atom (Si_1) associated with the NBO independent of the network silicon an effect which decreases with the formation of a silanol group in step 5. The more negative charge of both the silicon, and not just Si_1, is indicative of the generalized charge transfer which occurs in molecular structures form the formation of localized defects. Previous work by

Hamann on the charge state of a 2-Ring defect from Mulliken population analysis identified the existence of an unsupported pi bond between the two silicons [239]. The latent bond in the 2-Ring defect facilitates the charge transfer between the silicon atoms during the reaction (Figure 0-4.a and

Table 0-2). The un-supported pi-bond also accounts for the consistent charge difference between Si_1 and Si_2 until the formation of the NBO in step 4.

The oxygen atoms in the reaction exhibit a distinct difference in the charge states between the oxygen environments with O_1 and O_2 which are part of the 2-Ring structure exhibiting a consistently less negative charge than the O_3 in the water molecule. The effect decreases in step 5, when the water molecule has been bonded onto the silica surface in the form of silanol groups. An interesting note is that the formation of a NBO causes an abrupt decrease in charge on the silicon atom associated with the NBO rather than on the oxygen atom.

The hydrogen atoms initially exhibit a difference between the hydrogens which are part of the water molecule versus those that are part of the bulk water. Once the water molecule has disassociated in step 2, the charges of the different hydrogen atoms start to converge until step 5 at which point the charge transfer has been completed.

Overall, the analysis of the partial atomic charges describes the charge transfer which occurs during the annihilation of the 2-Ring defect including transfer of the charge from the water molecules to the surfaces as well as the effect on the atoms surrounding the defect site.

Table 0-2: Partial atomic charges of silicon, oxygen and hydrogen atoms involved in 2-Ring defect breakage mechanism in Figure 0-4.a-e. (Reaction Steps 1-5). Standard deviation is the standard error.

Step	1	2	3	4	5
Si_1	0.913±0.030	0.967±0.011	0.970±0.008	0.910±0.015	0.945±0.003
Si_2	0.995±0.025	1.024±0.010	1.025±0.015	0.982±0.008	0.981±0.010
O_1	-0.449±0.039	-0.550±0.019	-0.551±0.040	-0.589±0.023	-0.450±0.029
O_2	-0.481±0.022	-0.516±0.008	-0.515±0.023	-0.535±0.004	-0.486±0.005
O_3	-0.332±0.058	-0.279±0.018	-0.297±0.049	-0.370±0.022	-0.375±0.059
H_1	0.137±0.007	0.192±0.006	0.172±0.08	0.165±0.005	0.172±0.015
H_2	0.145±0.013	0.194±0.013	0.151±0.014	0.157±0.002	0.169±0.007
H_3	0.119±0.024	0.148±0.004	0.150±0.004	0.159±0.005	0.159±0.014

Table 0-3: Partial atomic charges of the water molecule and the 2-Ring defect structures during 2-Ring opening at the five stages pictured in Figure 0-3. (Reaction Steps 1-5)

Step	1	2	3	4	5
2-Ring	0.929	0.926	0.930	0.767	0.989
Water	-0.050	0.106	0.026	-0.048	-0.035

a).

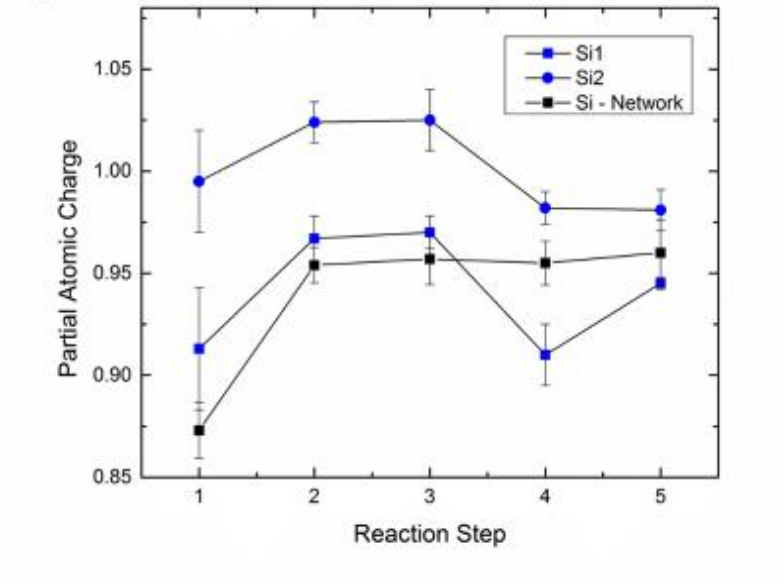
Si1
Si2
Si - Network
Partial Atomic Charge
Reaction Step
1.05
1.00
0.95
0.90
0.85
1
2
3
4
5

b).

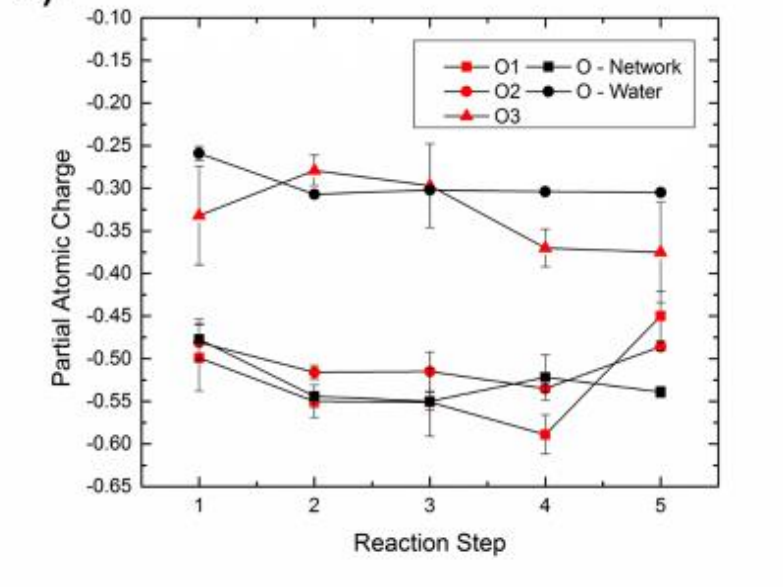
O1
O2
O3
O - Network
O - Water
Partial Atomic Charge
Reaction Step
-0.10
-0.15
-0.20
-0.25
-0.30
-0.35
-0.40
-0.45
-0.50
-0.55
-0.60
-0.65
1
2
3
4
5

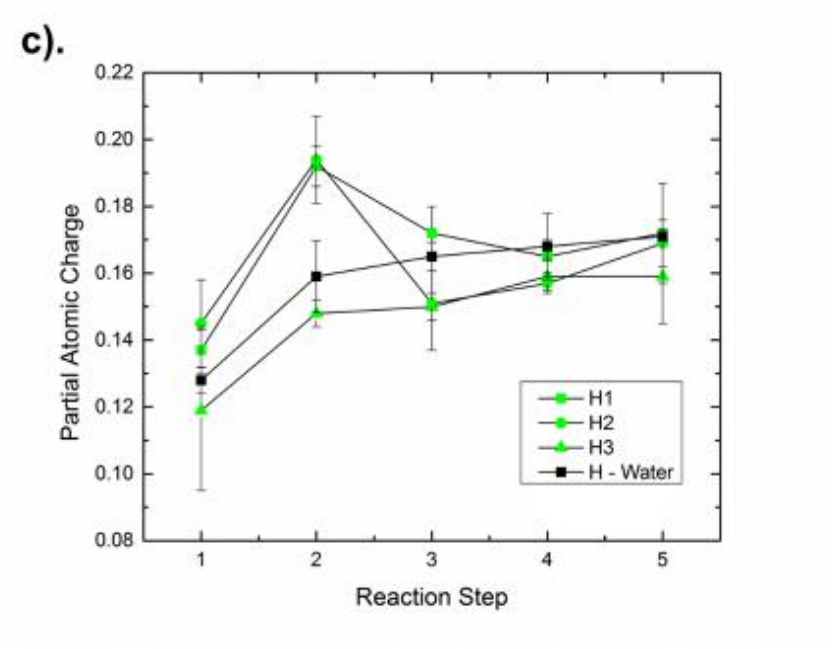

Figure 0-4: Changing partial atomic charges of (a) silicon, (b) oxygen, and (c) hydrogen atoms involved in the 2-Ring defect bond scission mechanism outlined in Figure 0-3. The error bars are equal to the standard error.

4.4.3 Bond distance – bond angle correlations

Bond angle-bond distance correlations provide an opportunity to investigate how constraints in the O-Si-O bond angle affect the Si-O distance in a single snapshot of the simulation. Typically, the bond angle distributions (BAD) and pair distribution functions (PDF) are presented independently from one another. Through the investigation of both distributions simultaneously, it is possible to identify outliers in both the BAD and PDF data and investigate how they relate to each other. In Figure 0-5 and Figure 0-6, the contour plots of the Si-O bond lengths in the nanoporous silica and surface silica models with the three O-Si-O bonds associated with the SiO_4 tetrahedra are presented. In a few cases, a fourth angle is included which only occurs if the silicon is five

coordinated identified by five oxygen atoms within the 2.25Å cut-off. The PDF and BAD data is included in the plots along the x-axis and y-axis, respectively, and are centered on the experimental bond length of 1.61Å and the ideal O-Si-O bond angle of 109.5^{o}.

Initially, both the nanoporous (31% porosity) silica structure model and the flat surface exhibit a broad distribution of bond lengths and bond angles (Figure 0-5.a and Figure 0-6.a). The surface model has more outliers in the initial configuration due to the introduction of water into the system, which generates an initial set of defects. After the geometry optimization was performed, there is a decrease in the distribution of the bond angles and bond distances indicating the relaxation of the silica surface. An additional 30ps of AIMD simulation further decreases the distribution of bond lengths and bond angles. Careful examination of the bond angle-bond distance correlations indicate that even after the 30ps of AIMD, a number of outliers remain in both systems, typically a O-Si-O bond above 140^{o} or below 100^{o} coupled with a Si-O bond length greater than 1.75Å. The outliers are attributed to the temporary formation of a Si^{5} defect, identified in the simulations performed here as well as by Kagan et al. [88]. Since the formation of the Si^{5} defect is the primary method through which siloxane bond breakage occurs, their continued formation indicates that there is sufficient energetic drive to form the intermediate defect, but that the energy barrier for breaking the ring structure is much higher. There is also a shoulder in the BAD on the y-axis which is attributed to an O-Si-O bond angle of ~90^{o} which is due to the stable concentration of 2-Ring and 3-Ring defects [30].

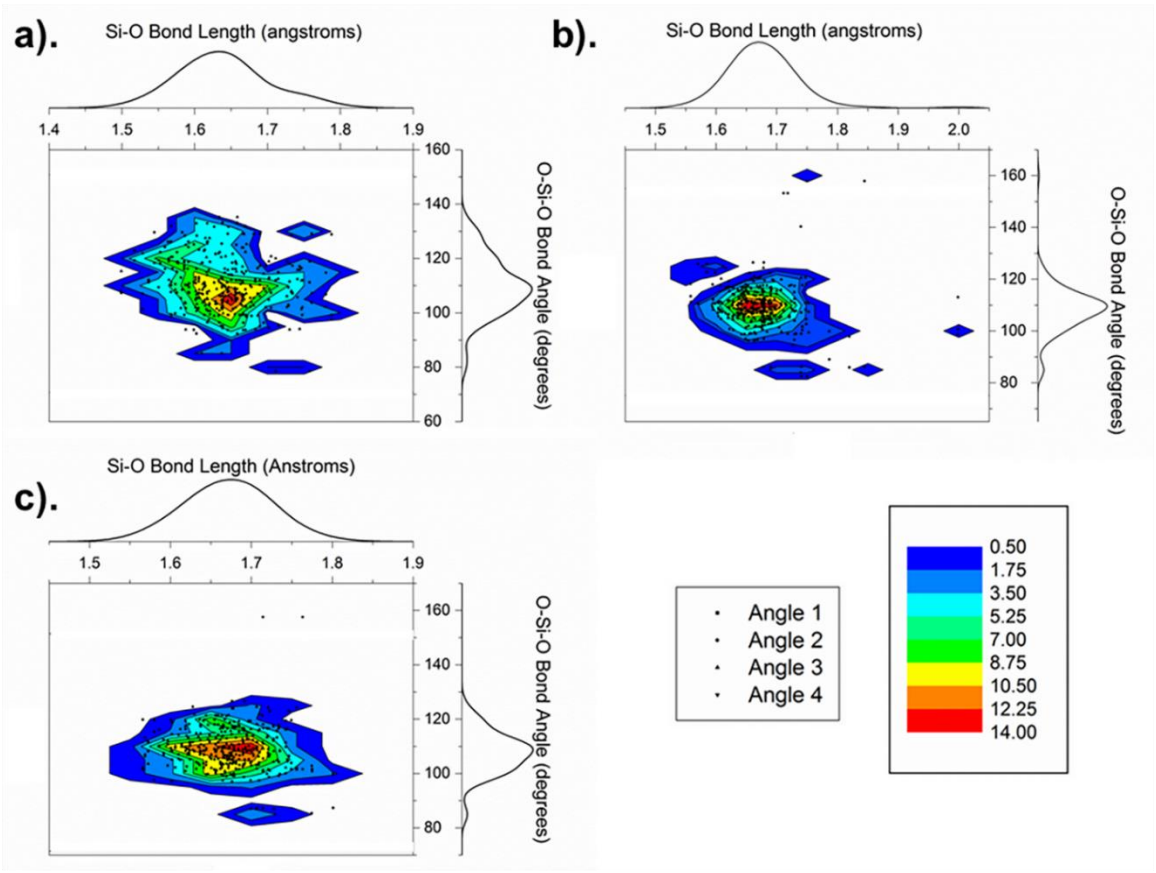

Figure 0-5: O-Si-O bond angle and Si-O bond length plots of 31% nanoporous silica computational systems (a) initial configuration (b) after geometry optimization and (c) after 30ps of AIMD. The Si-O pair distribution and O-Si-O bond angle distribution are on the x- and y-axis respectively.

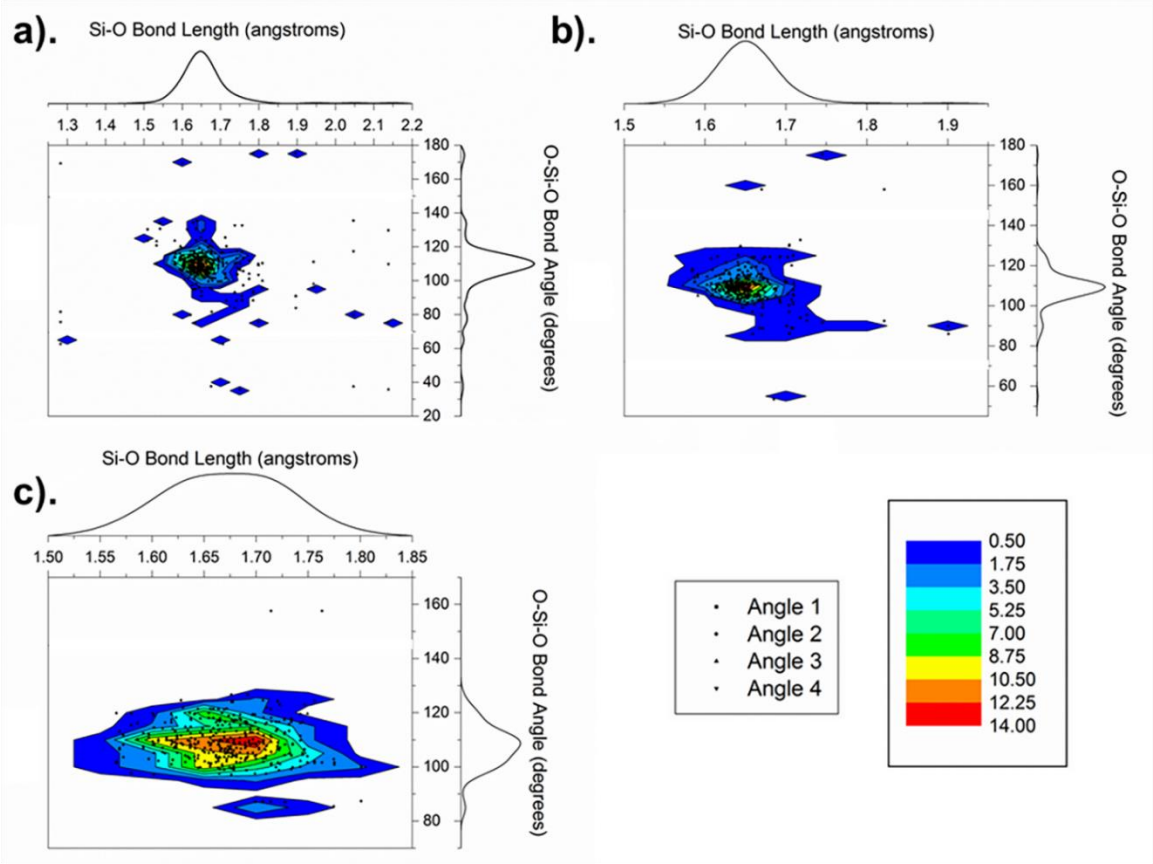

Figure 0-6: O-Si-O bond angle and Si-O bond length plots of silica surfaces computational systems (a) initial configuration (b) after geometry optimization and (c) after 30ps of AIMD. The Si-O pair distribution and O-Si-O bond angle distribution are on the x- and y-axis respectively.

3.4.3 Two-Membered Ring (2-Rings) Concentrations

2-Ring defects are high energy surface defects which have been identified in both computational and experimental systems. Thermodynamically, these high-energy defects are removed from silica systems almost instantaneously during their interaction with water. Kinetically, 2-Ring defect removal is complex due to the role of the water molecules in facilitating the reaction. Investigations by Tilocca and Cormack on the reaction of bioactive glasses with water using *ab initio* methods identified some stability

in 2-Ring structures [198]. The reactivity of 2-Rings is hypothesized to depend not only on water-defect interactions but also water-water reactions, and, since smaller rings can only react with 1-2 water molecules at a time, their reactivity is limited [198]. In a nanoporous silica system where access to sites is even more limited due to limited free space in the system, this affect is exacerbated. Kagan et al. also noted that energy barriers increased for silicon reaction sites on slightly concave surfaces since the water molecule interacts with atoms on the side of the pore as well as the defect itself [88]. Due to the varying position of the 2-Ring defects in the porous silica, a portion of them may be present on concave surfaces leading to variations in stability. Limited 2-Ring removal does occur in the highest porosity systems (52%+) where the defects would be most easily accessed by water molecules (Figure 0-7). The added curvature both increases the drive to remove the 2-Ring defects due to the added strain, but also increases the energy barrier due to its position. Therefore, there are a set of competing mechanisms to cause 2-Ring defect removal, due to the accessibility of the site and the curvature of the internal surface areas.

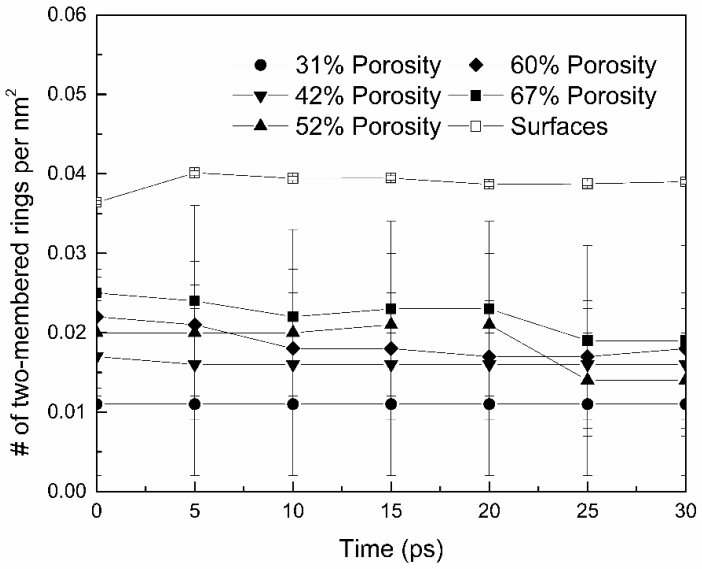

Figure 0-7: Changes in the 2-Ring defect concentrations per nm^2 of surface area for nanoporous silica systems with porosities between 31%-67% and flat surfaces. Standard deviation is equal to the standard error.

3.4.4 Silanol Concentrations on Hydroxylated Silica Surfaces

Silanol concentrations on silica surfaces are used to investigate defect concentrations since they are generated through the hydroxylation of common defect species (NBO, Si^3, 2-Ring, 3-Ring). Silanol concentration were calculated by identifying the number of Si-OH groups in the systems and then dividing by the internal surface area. By rolling a simulated solvent molecule with a 1Å radius along the nanoporous silica surface, a Connolly surface can be generated using Material Studio [240,241].

Silanol concentrations of ~4.6nm^{-2} have been reported for both computational and experimental systems with work by Du and Cormack identifying that the total silanol concentration can be separated by the initial defect species which are hydroxylated to form the silanol concentration [86]. The comparatively low concentration of silanol

groups in the nanoporous silica systems developed here (Figure 0-8) is the result of limited termination of ring defects during the course of the simulation (Figure 0-7). By identifying the concentration of 2-Ring and 3-Ring defects, and assuming that their removal will result in two additional silanol groups, a theoretical silanol concentration is calculated. The computational silica surfaces exhibit a theoretical silanol concentration of 3.92±0.11 silanol/nm^2 assuming complete defect removal. The nanoporous silica systems have a much broader range of theoretical silanol concentration between 2.8-3.7 silanol/nm^2 which varies with porosity. Differences in the theoretical maximum hydroxylation concentration for porous systems is attributed to changing surface morphology causing fewer defects per nm^2 of surface area. 2-Ring and 3-Ring defects were responsible for ~60% of the theoretical silanol concentrations.

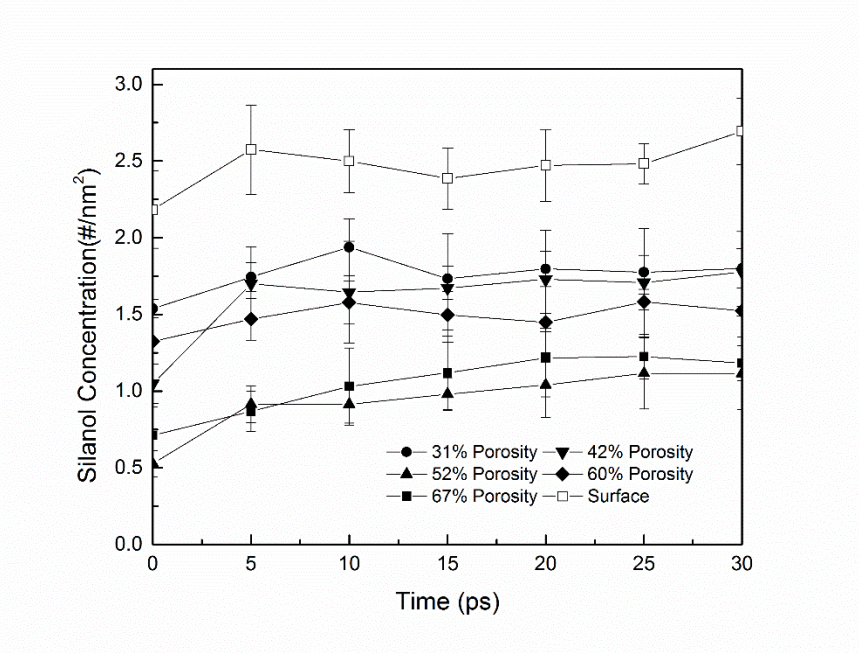

Figure 0-8: Silanol concentration in silanol/nm^2 for nanoporous silica systems with porosities between 31-67% porosity and flat surfaces with time. Standard deviation is equal to the standard error.

Experimentally, concentration of silanol groups on freshly fractured surfaces were quantified using SIMS and then used to predict reaction kinetics for silanol formation [118,121]. Two reaction regimes were noted to occur: one very rapid process due to the breaking of 2-Ring defects, followed by slower hydroxylation rate for 3-Ring breakage [118,121]. Similar reaction rates occur here with extremely fast reaction rates for the hydroxylation of coordination defects (Si^3, NBO) and slower reaction times for 2-Ring and 3-Ring defect removal. D'Souza and Pantano suggested the use of first order reaction kinetics to calculate the reaction rate using Eq. 0-2 where c(t) is the concentration at time, t, c_o is the initial concentration, and k is the rate constant:

$$c(t) = c_o e^{kt} \qquad \text{Eq. 0-2}$$

Using Eq. 3-2 and the final theoretical silanol concentration, the amount of simulation time required to reach maximum silanol concentration was estimated. It was found that in order to remove all the 2-Ring and 3-Ring defects from the nanoporous silica systems between 62-472ps of additional AIMD simulation time would be required, and for flat surfaces 1011±380ps would be required (Table 0-4). Both of these ranges are significantly higher than the 30ps of AIMD simulation time performed here and suggests that hydroxylation, even for highly strained 2-Ring defects, exhibit high energy barriers and are rare events requiring long simulation times. Since 2-Ring defects are the most reactive in a silica system, and they appear stable during 30ps of AIMD, it is expected that the simulation of Si-O bond breakage in bulk silica containing an average ring size of six would require significantly more simulation time, or the use of other methods such as Nudged Elastic Band (NEB) or potential mean force methods [167,242].

Table 0-4: Reactions rates and time to maximum silanol concentration for nanoporous silica computational systems and flat surfaces for removal of two-membered ring and coordination defects. Standard deviation is equal to the standard error.

Porosity	Reaction Rate (silanol/nm^2)	Maximum Silanol Concentration (silanol/nm^2)	Time to Maximum Silanol Concentration (ps)
31	0.005±0.001	0.20±0.16	472±137
42	0.017±0.004	0.92±0.41	192±71
52	0.005±0.001	0.70±0.37	436±53
60	0.025±0.008	1.68±0.06	128±63
67	0.021±0.008	1.41±0.10	63±23
Surface	0.007	0.99±0.89	1011±380

3.5 Conclusions

Interactions between water molecules and nanoporous silica models with porosities between 31-67% were investigated through the use of DFT based AIMD simulation. The 30ps of AIMD simulation time allowed for the accurate description of bond breakage and formation during water-silica reactions. It was found that coordination defects (NBO, Si^3) were converted to silanols during the initial geometry optimization while other ring structure defects (2-Ring, 3-Rings) were only partially removed during the simulation times. The limited 2-Ring defect removal is due to the restricted movement of water molecules through the porous structure and a slightly higher energy barrier reported for Si-O bond breakage on concave surfaces [88].

The observed mechanism for 2-Ring defect removal is consistent with previously proposed mechanisms that relies on the formation of the Si^5 defects before the opening of the ring structure. The Si^5 intermediate defect resulted in the charge transfer from the absorbed water molecule onto the silica surface and their continued development

throughout the simulation is confirmed through bond angle-bond distance correlation plots. Though the formation of Si^5 defects continued until the end of the AIMD simulations, the energy required to break the siloxane bond was not present. Analysis of the silanol concentrations with time suggested that full hydroxylation of the system is estimated to occur after 60-470ps of simulation time for the nanoporous silica systems and ~1100ps of simulation time for the flat surfaces.

CHAPTER 4

VALIDATION OF REAXFF CLASSICAL MOLECULAR DYNAMIC FORCEFIELD FOR INVESTIGATION OF SILICA HYDROXYLATION

4.1 Abstract

Characterization of water-silica interactions on the internal surfaces of nanoporous silica is critical to investigating the stability of silicate systems when in contact with water. Recently, the dissociative bond order based classical molecular dynamic (MD) potential ReaxFF was developed by van Duin et al., and has been extensively applied to the investigation of water-silica systems due to its ability to simulate complex reactions, and after parametrization by Fogarty et al. (ReaxFF-Fogarty), which has been recently improved by Yeon and van Duin (ReaxFF-2015). Hydrated nanoporous silica systems and cluster calculations of strained and unstrained silica dimers were simulated for 30ps using both ReaxFF potentials as well as *ab initio* molecular dynamic (AIMD) methods to provide information for the validation of the ReaxFF potentials.

The ReaxFF-2015 parameterization resulted in improvements in the activation energy for the breakage of strained siloxane bonds, which occur in two-membered ring (2-Ring) defects, from -0.16eV in ReaxFF-Fogarty to 0.72eV in ReaxFF-2015, along with improved stability of three-bonded oxygen defects while maintaining the hydroxylation rates of ~8.2 silanol/ns for ReaxFF simulations. Reaction mechanisms for 2-Ring defect removal includes the formation of an over bonded silicon (Si^5) defect through water absorption in the AIMD simulations along with the bonding of a hydrogen onto a bridging oxygen in the ReaxFF parametrizations with shorter intermediate defect lifetimes in ReaxFF-2015.

Additionally, analysis of strained and unstrained silica dimers used in the ReaxFF-2015 parametrization were consistent between ReaxFF and density functional theory methods (DFT), with the exception of a slight distortion in strained bond angles resulting in a less symmetric 2-Ring defect structure.

Overall, the parametrization of the ReaxFF potential by Yeon and van Duin is an improvement over the parametrization by Fogarty et al. resulting in more consistent reactions mechanisms, hydroxylation rates, and decreasing defect concentrations when compared to the *ab initio* simulations.

4.2 Introduction

Nanoporous silica commonly occurs in both natural systems and engineered materials, and can be found in the display, biomedical, microelectronic, and environmental applications. The variable pore structure, in both size and morphology, makes nanoporous silica well suited to applications such as catalysis support, separation of gaseous exhaust streams, hydrogen storage, and thermal insulation, all of which require high surface areas and adjustable pore sizes [243-245]. Interactions between water molecules and the complex internal surfaces formed in nanoporous silica are of particular interest since water affects the long term stability and mechanical properties of the silica backbone structure.

Recent experimental work has identified a number of features of water-silica interactions including reaction rates for the hydroxylation of fractured silica surfaces [118,121], the structure and dynamics of interfacial water in nanoporous silica [60,133], and the identification of various bonding environments in silica [62] using secondary ion

mass spectroscopy (SIMS), nuclear magnetic resonance (NMR), and sum-frequency generation spectroscopy. Due to difficulties associated with the characterization of the amorphous structure and randomized pore morphology, as well as difficulty analyzing short reaction times, simulations provide additional information on water-silica systems not available from experiment. Of particular interest is the characterizations of the mechanisms responsible for bond breakage and formation, how different environments affect the stability of defect species, and the hydroxylation rate of reactive silica surfaces.

Both DFT and classical MD studies have been employed to perform atomistic characterization of water-silica systems. Recently, DFT simulations have been used to analyze the hydrogen bonding of water to silanol groups, the surface silanol concentration, the development of structured water at the water-silica interface, energetics of the formation of silica monomers and dimers, and the protonation of silanol groups [110,115,134,246]. Additionally, detailed reaction mechanisms and energy barriers responsible for siloxane bond breakage in strained and un-strained silica sites have been reported by Rimsza and Du [87], Zapol et al. [167], and Rimola and Ugliengo [93] demonstrating the importance of *ab initio* simulations in identifying details of the water-silica interface.

Despite the successes achieved through the implementation of DFT methods to water-silica interactions, classical MD simulations offer a clear advantage over DFT simulations in terms of the size and length scales which can be investigated. In an attempt to bridge the gap between DFT accuracy and classical MD efficiency, Du et al. used mixed QM/MM (quantum mechanical/molecular mechanical) methods to

investigate water interactions with silica surfaces [105,106]. The reaction of water with two-membered ring (2-Ring) surface defects was analyzed and results indicated that system size and the amount of the surface treated with quantum mechanical methods have a significant effect on the dissociation energies [105,106]. The complexities involved with using QM/MM methods and the sensitivity to system size results in variation in the results and affects the application of these methods to the investigation of surface reactions. The ability to simulate from tens of thousands to millions of atoms for microseconds, several order of magnitudes larger than what can be simulated using DFT methods, makes classical MD simulations an extremely attractive option in the modeling of water-silica systems, especially in the study of the dissolution process, interfacial behavior, and gel structure evolution, where larger length and longer time scales are more desirable.

The primary drawback from the use of classical MD simulation is the development of potentials which describe the interatomic forces. Water-silica systems have several difficulties which must be overcome in order to develop a realistic potential including separate chemical environments for the oxygen in the water and the silica, polarization of the water molecules, and changing charge states during hydroxylation reactions. Early potentials focused on the structure and properties of bulk silica including two-bodied Buckingham potentials by van Beest, Kramer, and van Santen (BKS) and Sanders, Leslie, and Catlow [84,247]. In some cases, additional regulation of the O-Si-O and Si-O-Si bond angles was included through the use of three-bodied terms as in the Stillinger-Weber potential and the Born-Meyer-Huggins potentials by Feuston and Garofalini [100,248]. The introduction of water to the system further

complicated potential development due to hydroxylation reactions occurring on the surface, as well as the formation of hydronium (H_3O^+) ions and proton transfer in bulk water.

One of the first water-silica simulations which used classical MD was performed with a dissociative water potential proposed by Feuston and Garofalini [100]. In their potential, the bond lengths and bond angles associated with the oligomerization of orthosilicic acid (SiO_4H_4) was included to allow for the formation of Si-OH bonds as well as *ab initio* data on interactions between water molecules and silica monomers [100]. One drawback was that only four different interactions were included, and it is likely that other reactions not explicitly described in the parameterization were being excluded by the potential. Du and Cormack developed a set of partial charge potentials to study the hydroxylation of silica and silicate surfaces [86]. In the potential set, short range interaction of silica and silicate was described using the Buckingham form while a Morse potential was used for O-H interaction. Screened harmonic three-body term was used to constrain the Si-O-H bond angle. Hydroxylation of the silica surface was modeled with close to experimental silanol concentration ($4.5/nm^2$) with the potentials; however, no water potentials was included in the potentials set.

Recently, Mahadevan and Garofalini published a dissociative water-silica forcefield which was based on potentials by Guillot and Guissani by adding intermolecular interactions and allowing the parameters to vary with temperature and pressure [101]. The Mahadevan-Garofalini potential was applied to water-silica systems to investigate the life time of hydronium ions [136], hydroxylation [90], thermal expansion of nanoconfined water [89], and silica dissolution [88] . Yet another potential

developed for water-silica simulations was published by Hassanali and Singer, who used a BKS model for the silica and a SPC/E model for the water with Buckingham interactions to describe the water-silica interface [102]. Intermolecular interactions were added through *ab initio* data on the structure of silanol groups, donor-acceptor pathways for siloxane bond interactions, and the SiO_4H_4 molecule [102]. Several other water-silica potentials have been developed [103,107,249]; however, truly reactive potential that can reproduce the bulk silica and water structures and properties as well as their reaction energetics are rare in the literature.

A critical development in the simulation of water-silica interactions was the proposal of ReaxFF, a reactive force field initially developed by Goddard, van Duin and coworkers [82,97]. ReaxFF is a bond-order based potential which uses a complex series of ten different partial energy terms to describe the system energy and the bonding states of a material [82]. ReaxFF utilizes a EEM (electronegativity-equalization method) to calculate geometry dependent charges and equilibrate the charge over the entire system. There are several advantages to the ReaxFF potential model - one of which is the indistinguishability of the atomic species in the forcefield, and that atoms are allowed to freely and smoothly transition from one chemical species to another [85]. This feature is particularly important in the case of water-silica interactions since oxygen atoms are present both in the aqueous solution and the silica structure. Additionally, charges in the systems are not fixed, but vary depending on the local geometry and chemical environment [85]. ReaxFF was first parameterized for water-silica systems in 2010 by Fogarty et al. (ReaxFF-Fogarty) and demonstrated its capability in reproducing structural features and diffusion coefficients for water and silica [85]. In 2015, the

parameters described by Fogarty et al. were adjusted by Yeon and van Duin (ReaxFF-2015) to provide greater accuracy in the hydroxylation energy barriers and identified the role of hydronium ions in the formation of surface silanol groups [98]. While not as straight forward to parameterize and implement as the simpler two- and three-body potentials described previously, the underlying chemistry of the ReaxFF potential allows for a higher accuracy with a small penalty in computational efficiency. In the relatively short time that the ReaxFF potential has been available, it has demonstrated its application in a variety of silica-related studies and has quickly become one of the most widely implemented silica potentials. Examples of its application in recent years include silica crack propagation [250,251], O_2 and H_2 interactions with silica surfaces [252,253], investigation of friction and wear on silica surfaces [254], as well as its use in the simulation of mixed silica-hydrocarbon systems [255,256].

Despite the well-established accuracy of ReaxFF in describing water-silica systems, and the use of *ab initio* data in the fitting process, comparisons between the results from ReaxFF based MD simulations with dynamic data from *ab initio* MD simulations is critical to establish the accuracy of the potential. The validation of these methods provides information for the future use of the forcefield in even more complex structures and dynamic processes. Here, the ReaxFF potential is validated with AIMD simulations not just in the comparison of local structures such as bond lengths and bond angles, but in more complex water-silica reaction mechanisms such as hydroxylation of defect species, lifetimes of coordination defects, and activation energies for siloxane bond breakage. Such data provides insight into the accuracy of the ReaxFF potential

and validates its future use in water-silica systems to investigate silica dissolution, the role of water in stress-corrosion cracking, and more.

This chapter is organized in the following way. After introducing the computational methodologies, the results on the test of the silica dimers is first reported. A comparison of activation energy for siloxane bond breakage between the ReaxFF potentials and *ab initio* simulations is then given. An analysis of the 2-Ring defect reaction mechanisms, the life times of three-bonded oxygen defects, and hydroxylation rates provide insight into the kinetics of water-silica interactions. Finally, discussion and conclusions are presented.

4.3 Computational Methods

Several computational methods were used in this work to develop the nanoporous silica structures and perform the classical MD and AIMD simulations. The use of multiple methods allowed for efficient treatment of the system when the nanoporous silica structures were being developed, followed by dynamic simulations of the hydrated nanoporous silica system to identify water-silica reactions that can be performed using both classical MD and AIMD simulation methods.

4.3.1 Nanoporous Silica Structure Generation

To investigate the hydroxylation process on complex internal surfaces, nanoporous silica structure models with intricate porosity were created through a series of linear lattice expansions. A classical MD potential parameterized by Teter for silica, which accurately produces dense silica structural features, was used for the generation

of the nanoporous silica [86]. A 99 atom dense silica model with a density of 2.2 g/cm^3 is used as the basis for the nanoporous silica, and was created through a melt and quench procedure. The use of small systems sizes allows the structures to be efficiently simulated using DFT methods. To introduce volume into the dense silica, a four step protocol was implemented.

First, the dense silica underwent a liner lattice expansion by 20%, increasing the cell volume and the Si-O bonds lengths from 1500Å^3 to 1800Å^3 and from 1.6Å to 1.9Å, respectively. Next, the expanded silica structure is relaxed with a NVT ensemble for 30ps with a 1fs time step at 300K using a Nosé-Hoover thermostat. Atomic movement recreated some of the SiO_4 tetrahedra and incorporated the added volume into the system as voids. After relaxation the system contains ~20% porosity scattered throughout the structure. To create higher porosity models the relaxed systems are expanded again, adding additional volume and increasing the porosity. By repeating the expansion and relaxation process iteratively, the desired porosity is reached.

The final step is an isothermal-isobaric (NPT) relaxation is performed with a Nosé-Hoover thermostat and barostat to bring the system to a thermo-mechanical equilibrium. This step is critical in removing the negative pressure regions which can form due to the added vacuum space in the simulation cell [257]. The final nanoporous silica systems are 30-70% porous with densities between 0.74-1.53 g/cm^3. Simulations were performed in triplicate with different initial dense silica structures to account for variances in the amorphous system and porosity. The same method of generating nanoporous silica was used for larger systems (~3000 atoms) and short and long-range structural features of those system are included in Reference [235].

Hydration of the nanoporous silica structure was performed by overlaying a simulation cell of pure water on the nanoporous silica models. Any water molecules outside the boundary of the simulation cell or overlapping with the silica backbone were removed resulting in a hydrated nanoporous silica structure with a water density of ~1 g/cm^3. Due to the larger volume of free space available in highly porous systems, the number of water molecules increases with porosity, and simulation sizes vary between 150-370 atoms. Snapshots of a nanoporous silica before and after hydration are included in Figure 0-1.

a).

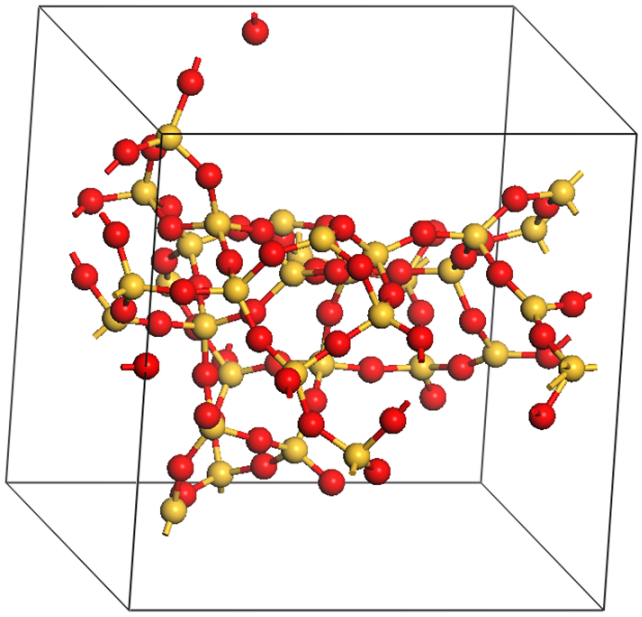

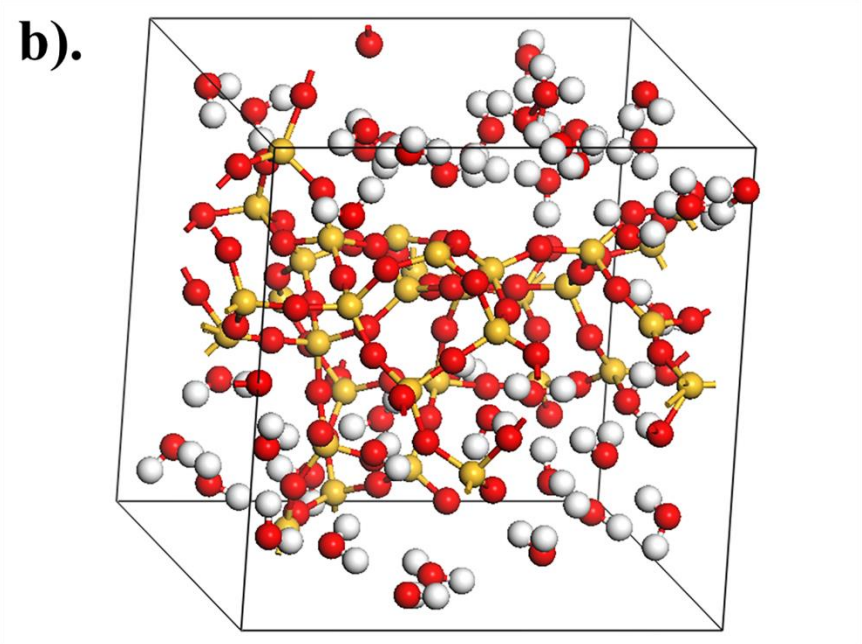

Figure 0-1: Snapshot of the 52% nanoporous silica systems (a) unhydrated and (b) hydrated. Red is oxygen, yellow is silicon, and white is hydrogen.

Due to inconsistencies in the minimization routines between the classical MD and DFT simulations, all the hydrated nanoporous silica systems underwent 500 steps of DFT geometry optimization before further simulations were performed. Details on the DFT methods used for the relaxation and AIMD simulations are included in Section 4.3.3. The initial geometry optimization steps allowed for removal of high energy structures formed by the introduction of water. An analysis of the effect of the geometry optimization on the system is included in Reference [87].

4.3.2 Reactive Force Field (ReaxFF) Methods

ReaxFF is a complex bond order based potential in which the system energy is the sum of several partial energy contributions (

Eq. 0-1) [82].

$$E_{system} = E_{bond} + E_{over} + E_{under} + E_{lp} + E_{val} + E_{pen} + E_{tors} + E_{conj} + E_{vdWaals} + E_{Coulomb} \quad \text{Eq. 0-1}$$

One of the primary benefits of using ReaxFF is that there are no fixed chemical bonds, and instead the bond order of an atom is calculated directly from the interatomic distances. The atomic bond order is evaluated at every step to allow for the formation and breakage of bonds during the simulation.

With the parameterization of ReaxFF for silica systems in 2003, additional terms were added separate from the original ReaxFF developed for hydrocarbons in 2001 [82,97]. These changes include separate disassociation energies for different bonding states (single, double and triple), an additional energy term for the treatment of lone pairs, and an adjusted valence angle term to account for the effect of the different bonding states [82]. Additional details and functional forms for these adjustments are included in the original paper, Reference [82].

Water-silica functionality in the ReaxFF potential was added by Fogarty et al. in 2010, and included parametrization to quantum mechanical data of water clusters and proton transfer in acidic and basic systems after which the silica parameters were refit to the silica training set from van Duin et al. [85,97]. Resulting water-silica simulations indicated excellent comparison between ReaxFF and DFT simulations as well as

experimental results on the structural features (bond lengths and bond angles), diffusion coefficients, and partial charge distributions [85]. ReaxFF-Fogarty was also used for the identification of water diffusion by proton transfer through a silica slab and polarization of the water molecules which interact with the silica surface [85]. One drawback with the ReaxFF-Fogarty potential was the low energy barrier for strained Si-O bond breakage which was corrected by the re-parametrization of ReaxFF by Yeon and van Duin [98]. In ReaxFF-Fogarty, the activation energy for siloxane bond breakage is underestimated, theoretically resulting in faster hydroxylation of strained Si-O bonds affecting the long-term stability of ring defects which is inconsistent with DFT data [85,98,256]. To correct this feature, reaction pathways for water with strained and unstrained siloxane bonds in silica dimers from DFT calculations were added to the training set for the ReaxFF potential parameterization. A discussion of the effect of the reparametrization on the activation energies for strained and unstrained siloxane bond breakage is included in Section 4.4.2.

Hydrated nanoporous silica systems were simulated using both ReaxFF-Fogarty and ReaxFF-2015 potentials for 30ps of classical MD using a 0.35ps time step at 300K controlled by a Nosé-Hoover thermostat. The ReaxFF simulations were performed in the MD simulation package LAMMPS using the USER-REAXC package [214].

4.3.3 Density Functional Theory (DFT) Methods

For comparison with ReaxFF classical MD simulations, DFT AIMD simulations were performed in parallel using the same initial nanoporous silica systems. A mixed Gaussian and plane wave basis set was implemented in the QUICKSTEP routine in

CP2K to provide increased efficiency over the use of pure plane wave codes while still allowing for efficient treatment of periodic boundary conditions [219,220]. The QUICKSTEP method in CP2K has been previously applied to the simulation of pure water, pure silica, and water-silica systems [54,78,110,134]. DZVP basis sets and the BLYP functional were used due to their ability to reproduce both the diffusional and structural properties of liquids [78] and silica [54] with an energy cut-off of 280 Ry. Similar computational parameters have been used to identify the structure of water inside a silica nanopore, the acidity of silanol species, and 2-Ring defect reactions [87,110,134]. Hydrated nanoporous silica underwent 30ps of AIMD using a 1fs time step at 300K, controlled by a Nosé-Hoover thermostat and requiring ~20,000 hours of simulation time per system.

4.4 Results

4.4.1 Structure of Strained and Unstrained Silica Dimers

Analysis of the strained and unstrained silica dimers provides insight into how the structure of the 2-Ring defects, which can be formed in the nanoporous silica systems, vary with simulation method. A silica dimer (Figure 0-2.a) and a hydroxylated 2-Ring defect structure (Figure 0-2.b) were selected as representative systems for unstrained and strained siloxane bonds. Similar models were used by Yeon and van Duin to reparametrize the ReaxFF potentials with improved energetics for 2-Ring opening (ReaxFF-2015 potential) [98]. The strained silica dimer is representative of a 2-Ring defect, which is a set of edge sharing SiO_4 tetrahedra, which has been hydrogen terminated. 2-Ring defects have been identified during the fracturing of silica in vacuum

conditions by SIMS and ^{29}Si dynamic angle spinning NMR experiments [65,118,120,138].

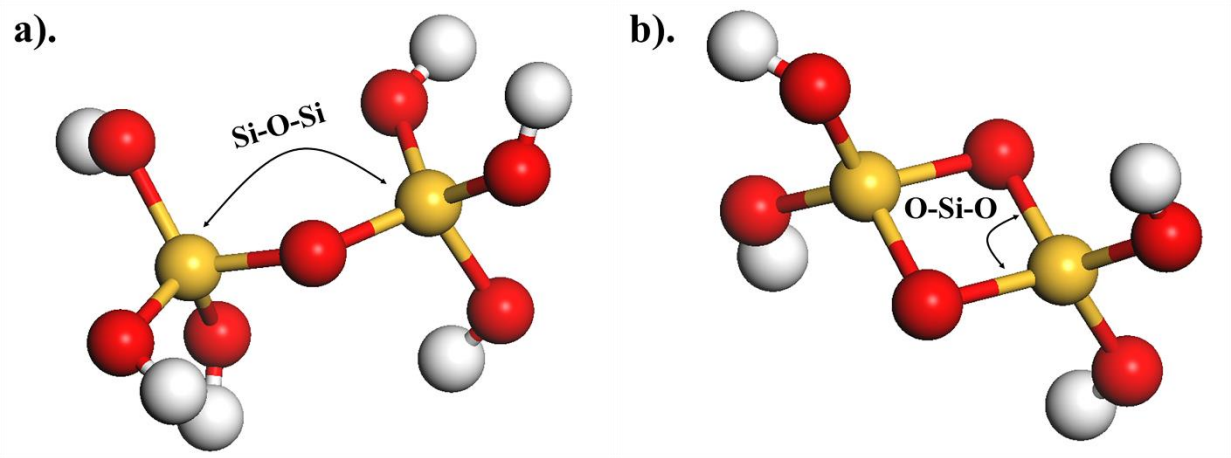

Figure 0-2: Snapshots of the (a) unstrained and (b) unstrained silica dimers. Red is oxygen, yellow is silicon, and white is hydrogen. Si-O-Si and O-Si-O bond angles are drawn schematically.

All simulations were performed in simulation cells with dimension of ~25Åx25Åx25Å and the energies of the structures were minimized through geometry optimization before analysis. To identify the equilibrium bond lengths and bond angles at 300K, bond angle distributions (BAD) and pair distribution functions (PDF) were generated from a 15,000 step NVT classical MD or AIMD simulation, to account for variations in the bond length due to thermal vibrations. Interatomic distances and bond angles are reported as the peak of the BAD or PDF value, as well as the full-width-at-half max (FWHM) of the peak in Table 0-1 and Table 0-2.

Table 0-1: Structural features of the unstrained silica dimer.

Property	AIMD		ReaxFF-Fogarty		ReaxFF-2015	
	Dimer	Surface	Dimer	Surface	Dimer	Surface
Si-O dist. (Å)	1.64 (0.08)	1.65 (0.08)	1.55 (0.07)	1.58 (0.09)	1.57 (0.09)	1.59 (0.11)
O-O dist. (Å)	2.68 (0.22)	2.68 (0.20)	2.55 (0.19)	2.56 (0.29)	2.58 (0.38)	2.58 (0.30)
O-H dist. (Å)	0.97 (0.02)	1.01* (0.08)	0.96 (0.07)	0.99* (0.07)	0.98 (0.05)	1.01* (0.08)
Si-Si dist. (Å)	3.13 (0.22)	3.20 (0.32)	2.91 (0.06)	3.06 (0.12)	3.06 (0.11)	3.12 (0.15)
Si-O-Si angle (º)	136 (22)	142 (38)	140 (9)	150 (22)	153 (26)	154 (37)
O-Si-O angle (º)	110 (12)	108 (12)	108 (11)	108 (17)	109 (12)	108 (15)
Si-O-H angle (º)	116 (13)	117* (17)	107 (7)	112* (9)	124 (9)	123* (7)

*from Si-OH located on internal surface are of nanoporous silica systems

The primary structural features of both the strained and unstrained siloxane bonds are consistent for the two simulation methods in terms of Si-O, O-O, O-H, and Si-Si interatomic distances (Table 0-1). In the unstrained system there is a decrease in the Si-O-Si bond angle for the silica dimer simulated using AIMD, which is a slight underestimation of the bond angle compared to experimental values of ~142º from NMR for bulk silica [258]. Alternatively, the Si-O-Si bond angles in the ReaxFF simulations are slightly overestimated as compared to the experimental value, which may arise from

significant variation in the strain states of the Si-O-Si bridges in the nanoporous silica. Additionally, the Si-O-Si bond angle appears to be contracted in the dimers relative to the dense silica for all simulation methods with angles decreasing by an average of 6^{o} and limited differences in the other bond angles in the system. Previous DFT methods have identified that the Si-O-H bond angle is ~119^{o} suggesting that ReaxFF-Fogarty had a slight underestimation of the bond angle while ReaxFF-2015 experienced a slight overestimation in both models studied [259]. The Si-O-H bond angle from AIMD simulations of this work is close to earlier DFT calculations while the difference between DFT and ReaxFF simulations is also within 5%.

In the strained silica structure the Si-Si interatomic distance is 2.4Å by AIMD methods, ~0.40Å smaller than the ReaxFF simulation values of ~2.8Å in both the dimer and the dense systems (Table 0-2) and consistent with previous DFT investigations using Gaussian 6-31G basis sets [139]. Additionally, in the AIMD simulations both the Si-O-Si and O-Si-O bond angles experience strain with bond angles of 90-94^{o}, significantly less than ~145^{o} and ~109^{o} reported for Si-O-Si and O-Si-O unstrained bond angles respectively [86]. Compression of both bond angles to ~90^{o} is consistent with previous DFT calculations [139,239,260]. In the ReaxFF methods both angles are compressed by ~35^{o} in the 2-Ring defects, with O-Si-O and Si-O-Si bond angles of ~74^{o} and 105^{o}, respectively. Therefore, the 2-Ring defects in the AIMD calculations are primarily symmetric with the O-Si-O bond angle only being compressed by ~20^{o} compared to ~50^{o} for the Si-O-Si bond angles. In previous simulations of nanoporous silica surfaces using classical MD methods with a silica forcefield and fixed partial

charges parameterized by Teter, the O-Si-O and Si-O-Si bond angles were ~85^{o} and ~90^{o}, respectively, which is consistent with the AIMD data present here [235].

Table 0-2: Structural features of the strained silica dimer.

Property	AIMD		ReaxFF-Fogarty		ReaxFF-2015	
	Dimer	Surface	Dimer	Surface	Dimer	Surface
Si-O dist. (Å)	1.69 (0.07)	1.66 (0.13)	1.59 (0.09)	1.56 (0.08)	1.57 (0.10)	1.58 (0.09)
O-O dist. (Å)	2.81 (0.16)	2.68 (0.20)	2.70 (0.45)	2.56 (0.29)	2.68 (0.42)	2.58 (0.30)
O-H dist. (Å)	0.97 (0.06)	1.01* (0.08)	0.97 (0.07)	0.99* (0.07)	0.98 (0.07)	1.01* (0.08)
Si-Si dist. (Å)	2.40 (0.10)	2.42 (0.09)	2.82 (0.08)	2.83 (0.06)	2.76 (0.06)	2.80 (0.08)
Si-O-Si angle(^{o})	91 (5)	91 (4)	106 (5)	105 (6)	104 (6)	103 (6)
O-Si-O angle(^{o})	89 (4)	89 (4)	74 (5)	74 (4)	76 (5)	76 (6)
Si-O-H angle(^{o})	117 (13)	117* (17)	108 (8)	112* (9)	124 (9)	123* (7)

*from Si-OH located on internal surface are of nanoporous silica systems

Discrepancies between the ReaxFF simulations and the AIMD data may be caused by the lack of a three-bodied term in the potential to regulate the bond angles, a strict distribution of charges which prevents the formation of a Si-Si unsupported pi-bond described by Hamman [239], or control of a Si-Si interatomic distances which limits the ability of the systems to form fully strained 2-Ring defects. While the effect of the varying strain on the O-Si-O and Si-O-Si bond angles on the reactivity is unknown,

future users of the potential should be aware that some small structural details of the interatomic angles are inconsistent between AIMD and the ReaxFF potentials while the bond distances are well represented.

4.4.2 Activation Energies for Siloxane Bond Breakage

A number of *ab initio* computational studies have been performed to investigate the activation energies related to 2-Ring defect removal and values between 0.32eV (7kcal/mole) and 1.27eV (29kcal/mole) are reported (Table 0-3). The identification of the exact activation energies for 2-Ring siloxane bond breakage is complicated due to variation in the methods used, the size of the surface models, the number of water molecules involved in the reaction, and the location of the 2-Ring defects in the system. For instance, 2-Ring defect structures located on concave surfaces are reported as having a higher activation energy [88] while Du et al. suggested that when more water molecules are involved in the reaction the energy barrier lowered a phenomenon also noted by Tilocca and Cormack [106,261]. Additionally, the use of small dimer structures, cluster calculations, or bulk surfaces models has been shown to have an effect on the activation energy of 2-Ring defect removal, as does the type of reaction mechanism [106].

When the ReaxFF-Fogarty forcefield was used to simulate water reactions with the strained silica dimer (Figure 0-2.b) an activation energy of -0.16eV (-15 kcal/mole) was identified, far below the range reported by *ab initio* methods (Table 0-3). For the ReaxFF-2015 parametrization, the reaction pathway for Si-O bond breakage in a strained silica dimer using DFT with a B3LYP functional and a 6-311++G(d,p) basis set, which had an activation energy of ~0.87eV (84 kcal/mole) was included [98]. The result

is an activation energy of 0.72eV (17kcal/mole) for the opening of the 2-Ring defect in a strained silica dimer using ReaxFF-2015, well within the range of previous investigations.

As a comparison, single point calculations of the reaction were performed using the AIMD methods described in Section 4.4.2, to identify differences in activation energies between ReaxFF and AIMD along the same reaction pathway for Si-O bond breakage. The strained siloxane bond activation energy is 1.7eV (Figure 0-3.a), higher than previous *ab initio* simulations and ReaxFF, which may be due to the use of the dimer structure and a single water molecule in the reaction. Additionally, the single point calculation geometries were derived from the reaction mechanism outlined in Reference [98], which may not be the minimum energy pathway for the AIMD simulations. The difference in the transition states between the two simulation methods also suggests that there is variation in the preferred both breakage mechanisms which may be responsible for the disparity in the activation energies. For the hydroxylation of unstrained siloxane bonds (Figure 0-2.b), the activation energy for ReaxFF-2015 and the AIMD methods used is 1.4eV and 1.13eV, respectively, which may again be the result of using single point calculations, rather than more accurate methods, such as nudged elastic band (NEB) calculations. A comparison of the energies for the single point reactions for water reaction with strained and unstrained silica dimers (Figure 0-2) are included in Figure 0-3.

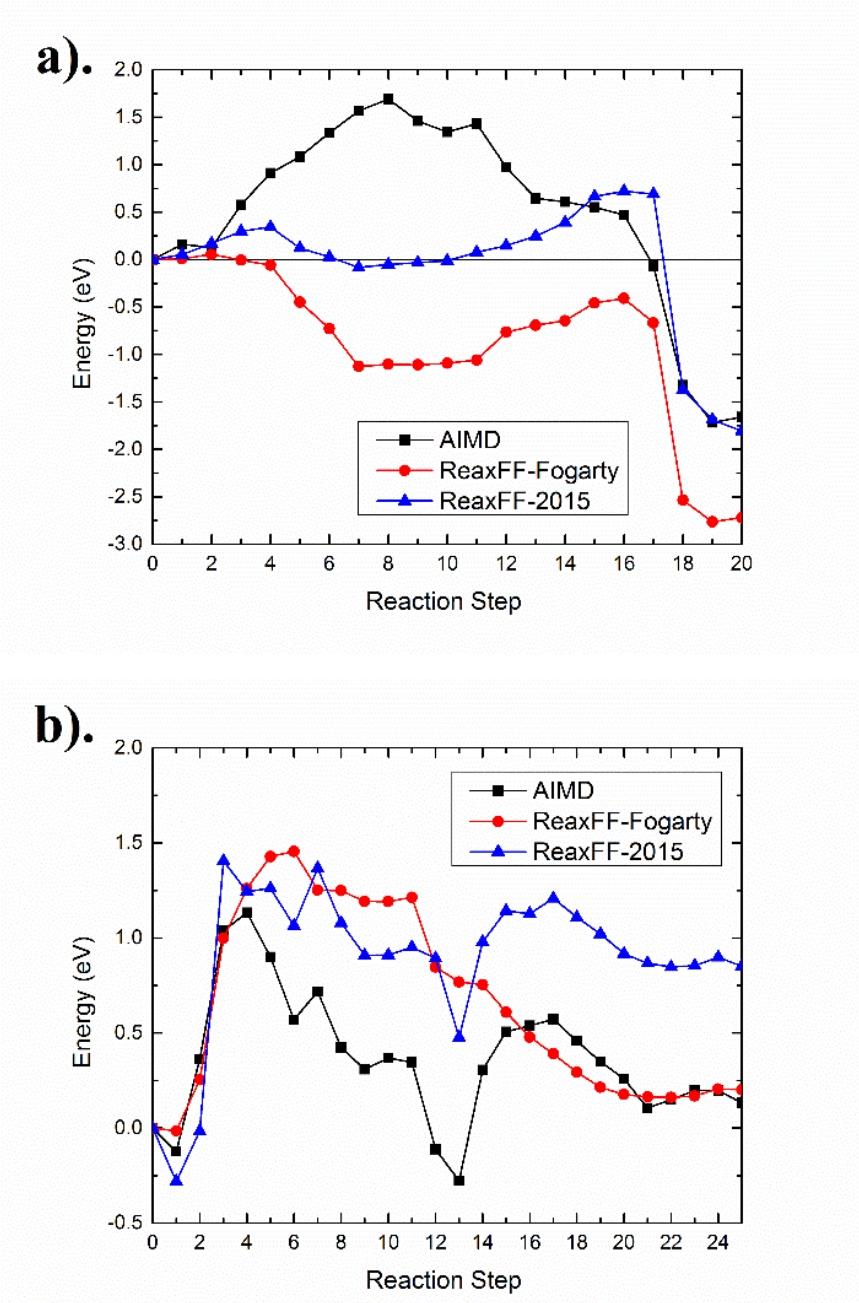

Figure 0-3: Energy barrier for the hydroxylation of a (a) strained and (b) unstrained silica dimers using AIMD simulation methods and the ReaxFF-Fogarty and ReaxFF-2015 classical MD potentials.

Table 0-3: Activation energies for siloxane bond breakage in a 2-Ring defect structure by classical MD and *ab initio* simulation methods.

Author	E_a (eV)	System	Method	Ref.
This Work (AIMD)	1.69	Dimer	DFT	
This Work (ReaxFF-2015)	0.72	Dimer	Classical MD	
This Work (ReaxFF-Fogarty)	-0.16	Dimer	Classical MD	
Rimola and Uglinego	1.08-1.27	Cluster	DFT	[93]
Walsh, Wilson, and Sutton	0.71-1.11	Cluster	DFT	[94]
Masini and Bernasconi	0.32-1.1	Bulk surface	CPMD*	[152]
Mischler et al	0.9	Bulk surface	CPMD*	[153]
Du et al.	0.41	Bulk surface	QM/MM	[106]

*Carr-parrinello molecular dynamics

4.4.3 Two-Membered Ring Defect Removal Mechanisms

Reaction energies for strained siloxane bonds are found to vary with the reaction mechanism responsible for the opening of the 2-Ring defect as well as the position of the 2-Ring defects in the system. This is due to kinetic limitations, which affect the accessibility 2-Ring defect sites by one or more water molecules which are involved in the reaction. Experimental reaction rates suggest that, regardless of the reaction mechanism, 2-Ring defects are removed from surfaces through the formation of silanol groups within the first few seconds of the surface being in contact with the atmosphere including ambient humidity [118]. In computational time frames (<1ns) 2-Ring defects have some stability due to their high activation energies relative to the energy gain associated with their removal.

Table 0-4 demonstrates the varying stability of 2-Ring structures across all the hydrated nanoporous silica systems investigated here with different rates of 2-Ring removal depending on the computational methods used. Since not all 2-Ring defects are removed, there are kinetic or structural barriers to these reactions, so that either the 2-Ring defect site is inaccessible or the interplay between the water molecules and the defect is affecting the ring stability. The mechanisms which are responsible for the removal of 2-Ring defects provide insight into this process.

Table 0-4: Number of 2-Ring defects structures in the hydrated nanoporous silica systems across all porosities with time and simulation method.

Time (ps)	0	5	10	15	20	25	30	Δ (0-30ps)
AIMD	23	14	13	13	13	11	9	14
ReaxFF-Fogarty	23	20	20	20	20	20	20	4
ReaxFF-2015	23	21	20	20	20	20	19	4

Previous first principles calculations have shown two different mechanisms responsible for the 2-Ring breakage in water-silica systems [152]. The most common is the absorption of a water molecule onto one of the silicon ions causing the formation of a Si^5 defect that eventually leads to the breakage of the Si-O bond and the opening of the 2-Ring structure. Of the fourteen 2-Ring defect reactions which occur in the AIMD simulations, all of them are the result of this mechanism. An analysis of this reaction mechanism is summarized in Reference [87], and it has been identified in a number of other *ab initio* simulation studies [93,94,106]. A proton from the absorbed water molecule can be transferred to the non-bridging oxygen (NBO) formed from the Si-O bond scission, so that a single water molecule causes the opening of a 2-Ring defect

and the formation of two silanols [93]. Alternatively, when two or more water molecules are present, a proton is transferred through the water to terminate the NBO with the rate of proton transfer depending on the location of the water molecules in the system.

The second and less common reaction mechanism of 2-Ring opening is the absorption of a proton onto one of the bridging oxygens (BO) in the 2-Ring defect, causing the simultaneous generation of a silanol group during the Si-O bond scission, which is discussed by Masini and Bernasconi [152]. The absorption of a proton onto a BO is reported as having an activation energy of ~0.32eV for the entire defect, compared to 1.1eV for the Si-O bond breakage with the formation of a Si^5 intermediate defect. The initial formation of the Si^5 intermediate defect has an activation energy of only 0.11eV, so that the Si^5 defects are preferentially formed suggesting that this mechanism is more common [152].

Interestingly, when 2-Ring defects are opened in the ReaxFF simulations, the most common reaction mechanism is a combination of the two discussed above. It includes the formation of both a Si^5 intermediate defect and the absorption of a hydrogen onto a BO. Absorption of the hydrogen onto the BO results in an extension of the Si-O bond from ~1.6Å to ~2.2Å and an expansion of the Si-O-Si bond angle to ~125^o, which may relieve strain in the defect structure allowing for an energetic drive for the formation of the intermediate defect. Snapshots of an example of a combined reaction for 2-Ring defect removal is included in Figure 0-4.a-d.

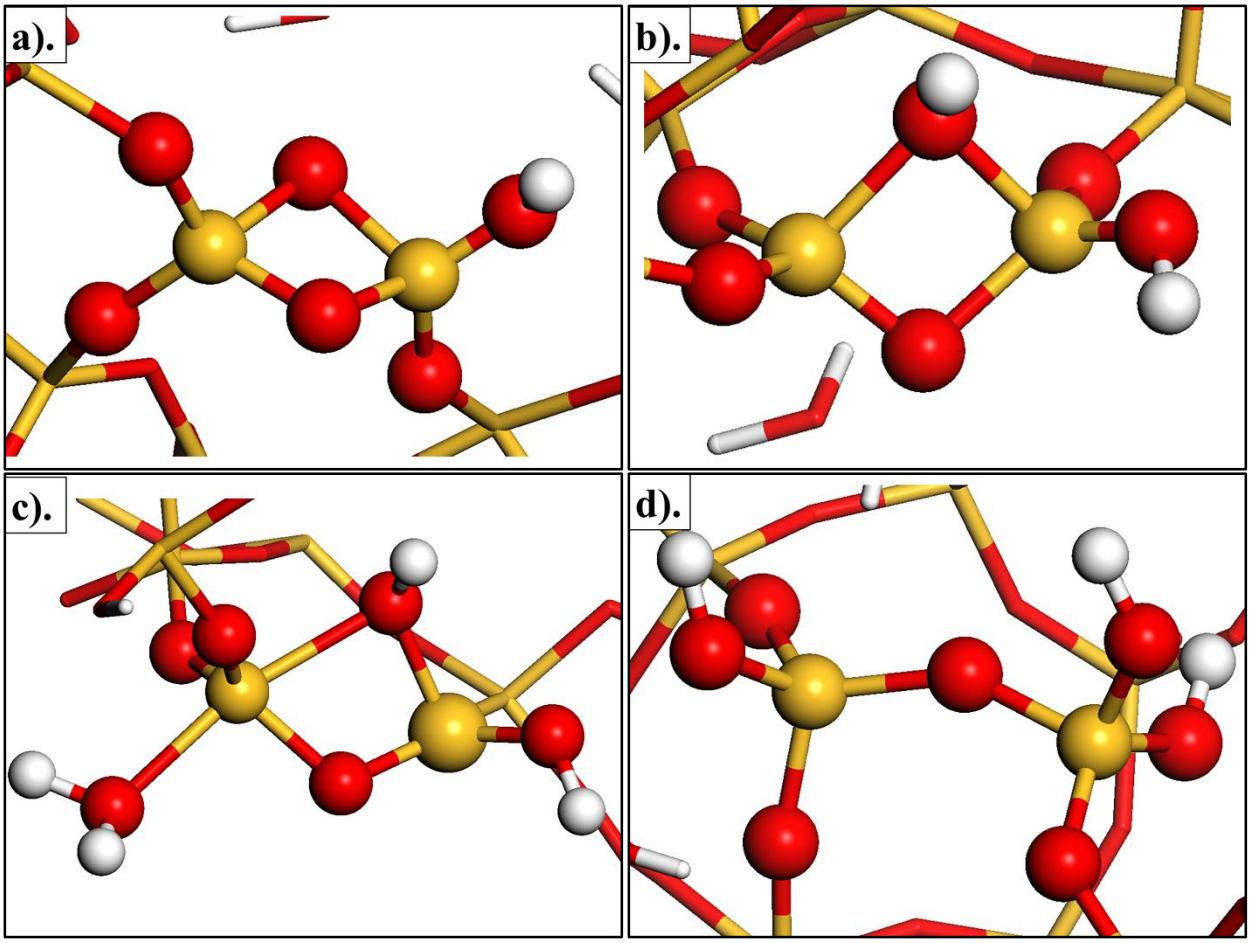

Figure 0-4: Snapshots of the four steps in the mechanism of 2-Ring defect breakage in a 42% hydrated nanoporous silica system simulated using the ReaxFF-2015 potential. Red is oxygen, yellow is silicon, white is hydrogen.

The removal of a 2-Ring defect (Figure 0-4.a) begins with the absorption of a hydrogen onto a bridging oxygen (Figure 0-4.b) which is stable for ~17ps. This is followed by the absorption of a water molecule onto a silicon forming a Si^5 bond (Figure 0-4.c) which is quickly followed by Si-O bond breakage, opening the 2-Ring defect and forming two silanol groups (Figure 0-4.d). There is significant variability in terms of which defect is formed first (the Si^5 intermediate defect or the absorption of the hydrogen onto the BO) and the lifetime of each defect before the 2-Ring defect opens. The lifetimes of the

intermediate defects are variable, and in some cases the intermediate defect structure survives until the end of the simulation. Variation in the life times and types of defects formed in the reactions are outlined in Figure 0-5.

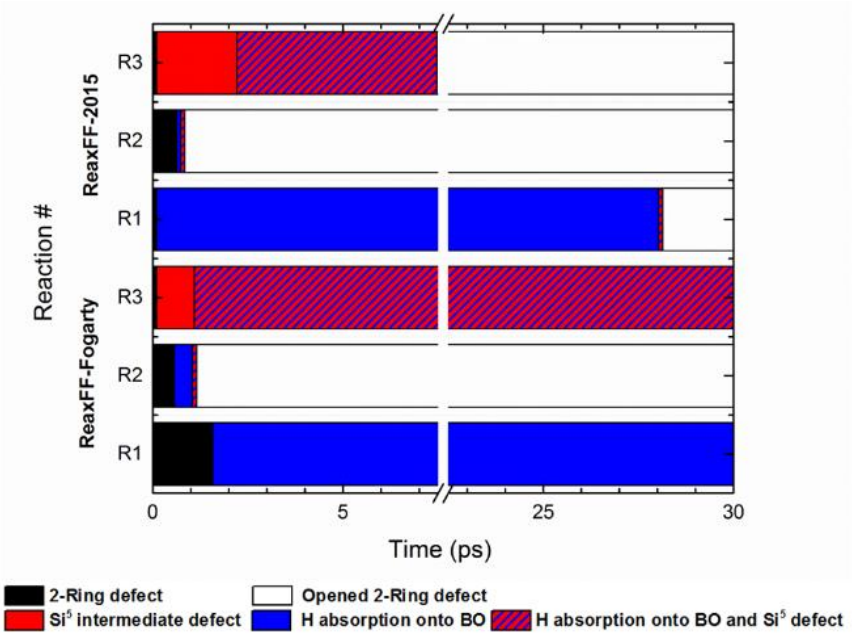

Figure 0-5: Lifetimes of the intermediate defect structures in 2-Ring defect reactions mechanisms in nanoporous silica simulated using the ReaxFF-Fogarty and ReaxFF-2015 classical MD potentials.

In order for the 2-Ring defect to be removed, both the Si^5 intermediate defect and the absorption of a hydrogen onto a BO need to occur, which happens more readily in the simulations using the ReaxFF-2015 potential (Figure 0-5). This may be due to the inclusion of the reaction pathway in the ReaxFF-2015 parametrization which contains both intermediate defect structures creating an energy drive for their formation. While the activation energy for the removal of the 2-Ring defect species is higher in ReaxFF-2015, the lifetimes of the intermediate defects appears to be shortened, the opposite of the expected outcome. Despite the differences in the activation energies, it appears that

the incorporation of the trajectory for 2-Ring defect removal in the ReaxFF-2015 parametrization has resulted in an improved reaction mechanism compared to the AIMD simulations.

4.4.4 Stability of Three-Bonded Oxygen Defects

During the formation of the nanoporous silica systems a number of high energy surface defects are generated including under bonded silicon (Si^3), NBO, and the aforementioned ring structure defects. Another rarely occurring defect is the three-bonded oxygen (TBO) or oxygen tricluster, which occurs when an oxygen is bonded with three network formers in a glasses. In the nanoporous silica systems studied here, low concentrations of TBO (<1%) were identified across the different porosities (Figure 0-6).

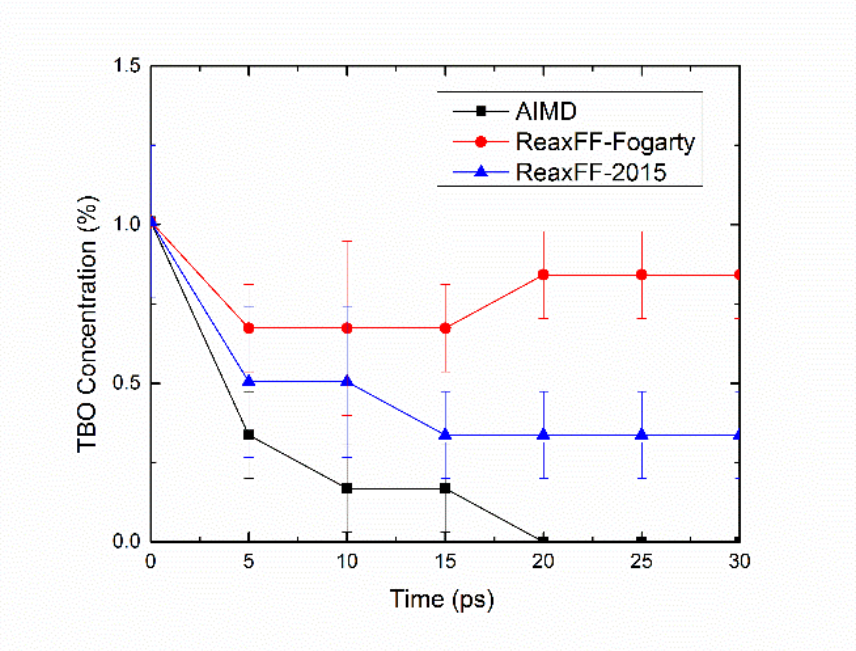

Figure 0-6: Concentration of three-bonded oxygen (TBO) in the hydrated nanoporous silica systems simulated using AIMD or classical MD (ReaxFF-Fogarty and ReaxFF-2015).

TBO are known to occur in other amorphous oxide systems, such as sodium aluminosilicates, with concentrations as high as 30% identified by NMR [262,263]. However, classical MD simulations on sodium aluminosilicates performed by Xiang et al., noted that the oxygen in the TBO were always bonded to a minimum of one aluminum atom, and that the formation of TBO bonded exclusively to silicon does not occur [262]. This is due to the role of the TBO as a charge compensating mechanism for a lack of available Na^+ to neutralize the NBO associated with an AlO_4 tetrahedron [262]. In the nanoporous silica systems studied here, the TBO defect is unstable, and should be removed very early on in the simulations for both the AIMD and ReaxFF simulations.

In the AIMD simulations TBO are stable for the first 20ps, with a consistent decrease in their concentration with time (Figure 0-6). For the ReaxFF simulations, there is additional stability of the TBO with the ReaxFF-Fogarty potential demonstrating an increase in their concentration after 15ps (Figure 0-6). The ReaxFF-2015 parametrization is an improvement in the stability of the TBO over the ReaxFF-Fogarty version with lower concentration of TBO which decrease with time.

Examination of the location of the TBO indicate that they occur primarily as part of a 2-Ring defect (Figure 0-7.a), which was also identified in classical MD simulations by Winkler et al. [264]. The existence of stable TBO in pure silicate systems may be due to the decrease in energy associated with a perturbation of the highly strained 2-Ring structure caused by the TBO. There is an expansion of one of the Si-O-Si bond angles from ~ 105^o to ~125^o, as well as elongation of the Si-O bonds to ~2.2Å, relieving some of the strain. After varying amounts of simulation time one of the Si-O bonds from

an adjacent Si^5 defect breaks off and rotates to terminate the newly formed Si^3 defect due to the removal of the TBO (Figure 0-7.b). After the reaction is completed all of the silicon are four-coordinated and the oxygen are two coordinated, forming complete SiO_4 tetrahedra (Figure 0-7.c). The removal of the TBO does not require a water molecule to facilitate the reaction, and is caused by a thermodynamic drive to decrease the energy of the system.

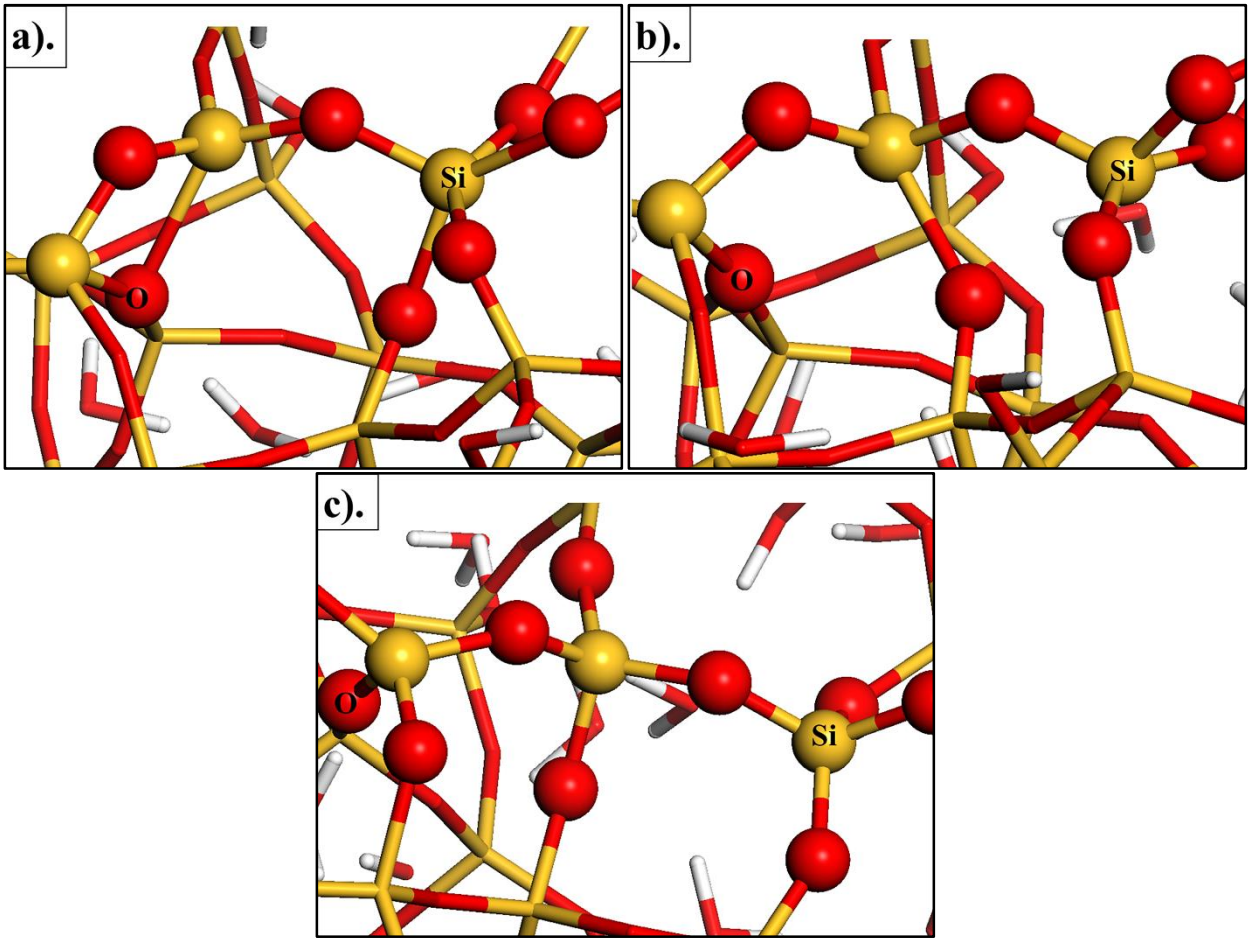

Figure 0-7: Snapshots of three-bonded oxygen (TBO) defects in the hydrated nanoporous silica systems including its reaction with an over bonded silicon. Red is oxygen, yellow is silicon, and white is hydrogen.

4.4.5 Hydroxylation Rates in Nanoporous Silica

Hydroxylation rates of the unreacted internal surface area of the nanoporous silica structures provide insight into the dynamics of the water-silica interface and the energy gain associated with their removal. Previous computational and experimental work has identified the silanol concentration on silica surface to be ~4.6/nm^2 due to the termination of coordination and ring structure defects in the systems [86]. The AIMD simulations have a final silanol concentration of 3.85±0.22 silanol/nm^2 slightly lower than the experimental value and ~0.3 silanol/nm^2 higher than in the ReaxFF simulations (Table 0-5). Due to the time frames of the simulations, it is not expected that the surface would be fully hydroxylated, and previous studies indicated that between 50-500ps of AIMD simulation time is required for the hydroxylation of nanoporous silica systems depending on the porosity [87].

Additionally, reaction rates were calculated using a first order reaction rate equation, which was suggested by D'Souza and Pantano and implemented by Rimsza and Du for describing the fast hydroxylation behavior in computational and experimental systems [87,118,121]. The reaction rate is described by Eq. 0-2, with C(t) as the silanol concentration at t=0.03ns (30ps), C_0 as the concentration at the beginning of the MD simulation time, t as the elapsed time (0.03ns), and k as the reaction rate[121]:

$$C(t) = C_o e^{kt} \qquad \text{Eq. 0-2}$$

The hydroxylation rate of 11.7 silanol/ns for the AIMD simulation is slightly higher than values of 8.4 silanol/ns for the ReaxFF systems, but overall there is a reasonable agreement between the two methods. Additionally, the re-parameterization of the ReaxFF forcefield does not appear to have made a difference in the hydroxylation rate

between ReaxFF-Fogarty and ReaxFF-2015 potentials, which is surprising since there was a significant change in the activation energy for the removal of 2-Ring defects, which affects the silanol concentration. Since hydroxylation rates are dependent on the termination of defect species, analysis of changing defect concentrations with time can highlight varying defect stability in the nanoporous silica structures.

Table 0-5: Silanol concentration with time for hydrated nanoporous silica systems using AIMD methods and classical MD potentials ReaxFF-Fogarty and ReaxFF-2015. Concentrations are averaged (Avg) over all porosities with the standard error (SE).

	Time (ps)	0	5	10	15	20	25	30	Reaction Rate (silanol/ns)
AIMD	Avg	2.74	3.58	3.78	3.76	3.80	3.90	3.85	11.7
	SE	0.21	0.20	0.21	0.20	0.20	0.21	0.22	
ReaxFF-Fogarty	Avg	2.74	3.43	3.47	3.51	3.55	3.55	3.53	8.4
	SE	0.21	0.21	0.22	0.22	0.23	0.22	0.23	
ReaxFF-2015	Avg	2.74	3.12	3.31	3.29	3.35	3.43	3.51	8.2
	SE	0.21	0.19	0.19	0.20	0.19	0.18	0.21	

Defect concentrations are broken down into coordination defects (Si^3, Si^5, NBO) and ring structure defects (2-Ring and 3-Ring defects), and are included in Figure 0-8. The decreasing concentration of coordination defects in the structure is well represented by both ReaxFF methods and is in close agreement with the AIMD simulations (Figure 0-8.a). This indicates that the initial rate of hydroxylation is consistent between the two methods, and that there is little tendency to maintain the coordination defects (beyond the low levels of TBO which were discussed previously). For the ring structure defects, the AIMD simulations appear to be more reactive

resulting in a greater decrease in 2-Ring and 3-Ring defect concentrations with time. Rate of 2-Ring removal is consistent between both ReaxFF-Fogarty and ReaxFF-2015 methods, but the ReaxFF-2015 potential exhibits an improvement in the 3-Ring concentration with time over the ReaxFF-Fogarty forcefield (Figure 0-8.b). Overall, the ReaxFF-Fogarty and ReaxFF-2015 potentials results in similar hydroxylation rates, which slight improvements in the 3-Ring removal rate in the ReaxFF-2015 version in comparison to the AIMD simulations.

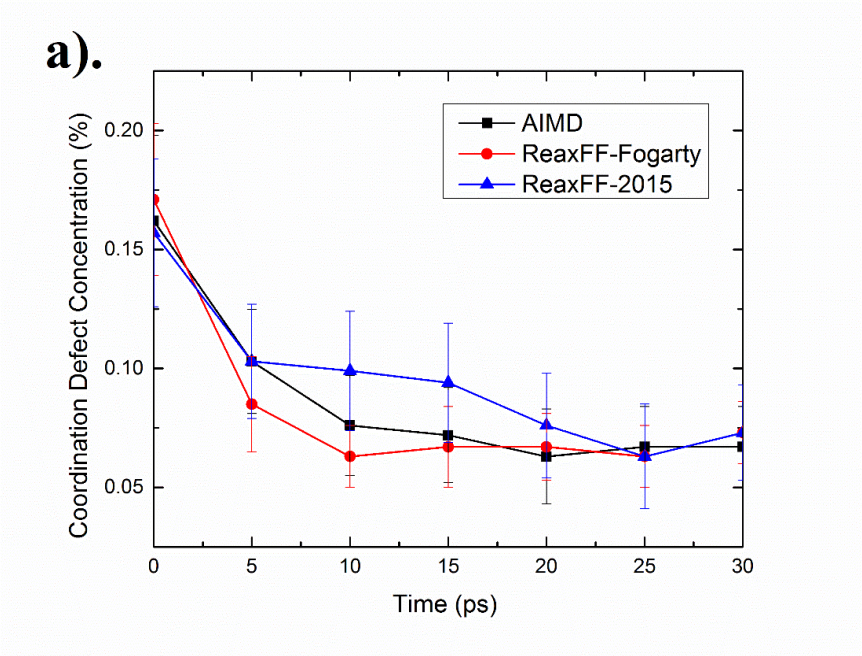

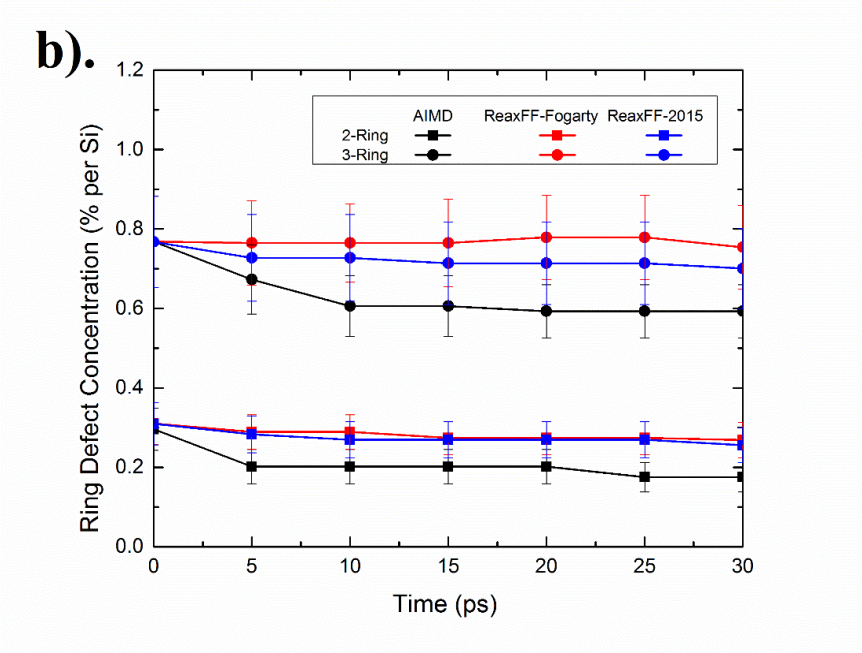

Figure 0-8: Concentration of (a) coordination defects (Si^3, Si^5, NBO) and (b) ring structure defects (2-Ring and 3-Ring defects) with time. Error bars are the standard error.

4.4.6 Water Diffusion Through Nanoporous Silica

An important aspect of water-silica interactions is the movement of water molecules and individual protons through the internal pore space in the nanoporous silica structure, which can have a significant effect on the diffusion rate. Diffusion also affects the reaction rate between water and silica since the water molecule needs to diffuse towards the coordination or 2-Ring defect before it can be terminated or removed. Another important aspect of water diffusion is the movement of hydrogen atoms through the solution separate from the diffusion of the entire water molecule, a method of atomic transport termed hydrogen hopping [136].

Several previous studies using NMR [58,60,63] and DSC [124] have identified a region of frozen or structured water located next to silica surfaces, which results in

slower atomic movement and diffusion compared to the bulk values. Simulations suggest that the region of water affected by the existence of nearby silica surfaces extends a minimum of 10Å into the liquid [59,134]. Based on this criterion, nearly all of the water molecules in the nanoporous silica studied here would be considered interfacial water, and the diffusion coefficient is expected to be lower than in bulk water systems. Changes in the diffusion coefficient of water are most extreme within the first monolayer of water due to the formation of a hydrogen bond network between the water molecules and the surface silanol groups limiting atomic movement [128]. The limited diffusion of water next to silica surface is most extreme for the first monolayer, and the farther a water molecule is from the surface, the less of an affect is seen on the orientation and diffusion of the water molecule [130]. Therefore, as more free space is introduced into the system, the diffusion of water is expected to increase since less of the water molecules will be hydrogen bonded to the surface silanol groups.

Diffusion rates in the hydrated nanoporous silica systems were calculated through the use the mean squared displacement (MSD) and the Einstein diffusion equations, discussed in Section 2.5.2, to identify diffusion rates of different atomic species in the system. The oxygen in the water and in the silica are separated, as is the hydrogen and the oxygen in water molecule, to allow for the identification of changing diffusion rates between atomic types.

Overall the water present in the nanoporous silica has much slower diffusion coefficients than bulk water (Table 0-6) due to the formation of the aforementioned hydrogen bonding network which slows atomic movement. It is expected that the diffusion coefficient would increase for the hydrogen and oxygen in the water with

increasing porosity due to few water molecule being in contact with the surface (Figure 0-9). In the classical MD simulations, the diffusion coefficients demonstrate this trend with an almost linear increase with porosity. The trend in the AIMD data is more complex (Figure 0-9) which does not exhibit as clear a trend possibly due to the higher reactivity of the surface which results in the oxygen and hydrogen atoms in the water molecules reacting with the surface, forming silanols. Once the atoms have bonded with the surface, the diffusion coefficient would drop significantly, resulting in inconsistent diffusion coefficients. Comparatively, in the ReaxFF simulations, the water molecules may interaction less with the surface resulting in a linear increase in the diffusion constants with more available free space.

The relative diffusion coefficients of the hydrogen atoms compared to the oxygen indicates that the hydrogen diffuses faster than the oxygen atoms at all porosity levels and in all the simulation methods used. This is due to the aforementioned proton transfer in the solution, and ReaxFF potentials are capable of replicating this complex and important feature of bulk water systems, an important requirement in the modeling of water-silica interactions [85].

Table 0-6: Diffusion coefficients (10^{-9} m^2/s) of hydrogen and oxygen in the water molecules in the hydrated nanoporous structures reported as the average of three simulations with the standard error.

	AIMD			ReaxFF-Fogarty			ReaxFF-2015		
Porosity (%)	D_H	D_O	D_H-D_O	D_H	D_O	D_H-D_O	D_H	D_O	D_H-D_O
31	0.52 ±0.05	0.48 ±0.02	0.04 ±0.03	0.34 ±0.06	0.29 ±0.03	0.05 ±0.05	0.40 ±0.03	0.27 ±0.01	0.13 ±0.04
42	0.31 ±0.12	0.18 ±0.12	0.14 ±0.01	0.69 ±0.11	0.53 ±0.14	0.16 ±0.03	0.49 ±0.04	0.33 ±0.03	0.16 ±0.03
52	0.57 ±0.09	0.28 ±0.01	0.29 ±0.10	0.78 ±0.13	0.65 ±0.15	0.13 ±0.04	0.75 ±0.06	0.63 ±0.07	0.12 ±0.01
60	0.67 ±0.16	0.62 ±0.18	0.05 ±0.02	1.08 ±0.10	0.96 ±0.09	0.13 ±0.03	1.01 ±0.09	0.86 ±0.09	0.15 ±0.01
67	0.45 ±0.03	0.40 ±0.03	0.05 ±0.01	1.22 ±0.11	1.06 ±0.11	0.17 ±0.01	1.18 ±0.22	1.01 ±0.17	0.17 ±0.05
100 (H_2O)	3.13 ±0.03	2.94 ±0.02	0.19 ±0.01	2.73 ±0.38	2.59 ±0.35	0.14 ±0.03	2.90 ±0.73	2.82 ±0.72	0.09 ±0.03

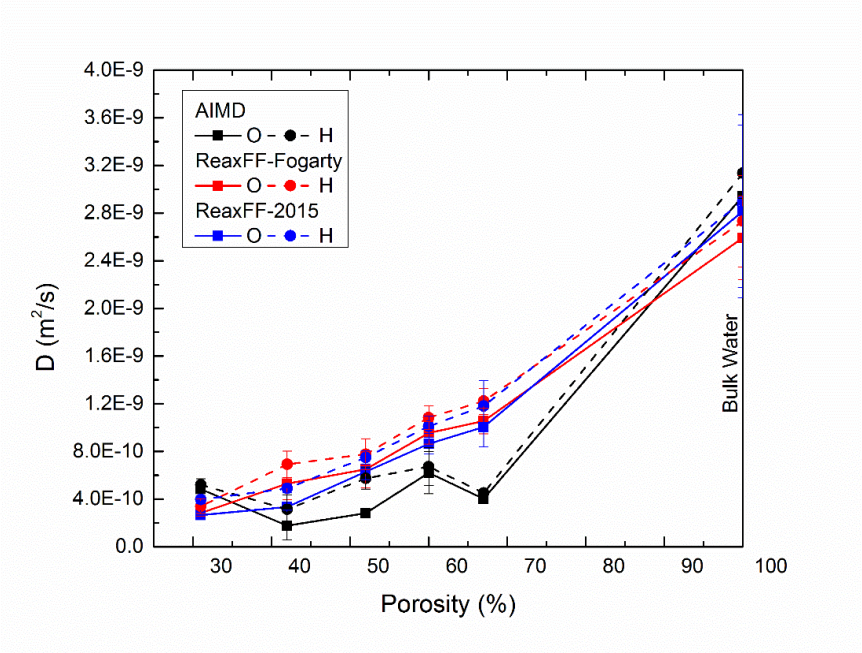

Figure 0-9: Diffusion coefficient for water molecules, separated into hydrogen and oxygen atoms, in hydrated nanoporous silica systems.

4.5 Conclusions

Two versions of ReaxFF water-silica parametrizations by Fogarty et al. (ReaxFF-Fogarty) and Yeon and van Duin (ReaxFF-2015) were used to model the structure and the dynamic properties of water-nanoporous silica interactions while parallel AIMD simulations were performed using the CP2K code (AIMD) to validate the classical MD potential ReaxFF [85,98].

Structural analysis of strained and unstrained silica dimers used for parametrization of water-silica reactions in the ReaxFF-2015 potential indicated that there is excellent agreement in interatomic distances of the clusters and ~10^{o} difference in the O-Si-O and Si-O-Si bond angles. The bond angle differences are possibly due to a lack of Si-Si bond formation indicated in previous DFT calculations [239] or by a constraint in the Si-Si bond distances.

Activation energies for the breakage of strained and unstrained siloxane bonds are ~0.72eV in the ReaxFF-2015 simulations in agreement with previous *ab initio* investigations and a significant improvement over the value of -0.16 eV reported for the ReaxFF-Fogarty potential.

Study on the reaction mechanisms for 2-Ring defect removal from ReaxFF based simulations demonstrates that both a Si^5 intermediate defect and the absorption of a proton onto the BO is required in order to break the Si-O bond and open the 2-Ring defect. DFT based AIMD simulations only exhibit the formation of the Si^5 intermediate defect during 2-Ring opening. The formation of both defect structures in the ReaxFF simulations are consistent with the reaction pathway used in the parametrization of the ReaxFF-2015 forcefield. Additionally, the ReaxFF-2015 potential results in shorter lifetimes for both intermediate defect species which is more consistent with the AIMD simulations.

Low levels (~1%) of three-bonded oxygen (TBO) were also observed in all the nanoporous silica systems studied with increased stability of the defect noted in the ReaxFF-Fogarty potential over the ReaxFF-2015 version. In comparison, TBO has a much shorter lifetime in AIMD simulations of hydroxylated nano-porous silica and all TBO defects are removed after around 20 ps in AIMD simulations. The differing stability of the TBO may be related to the stability of the hydrogen absorbed onto a BO in the 2-Ring defect removal mechanism both of which cause changes to the Si-O-Si and O-Si-O bond angles and Si-Si interatomic distances in the 2-Ring defect structure.

Hydroxylation rates for the three methods are between 8.2-11.7 silanol/ns and are described using first order reaction kinetics, with the higher reaction rates in the AIMD

simulations being the result of the increased reactivity of the 2-Ring defects due to the long life times of the intermediate defect species. Hydroxylation rates of the coordination defects (Si^3, Si^5, NBO) are consistent between AIMD, ReaxFF-Fogarty, and ReaxFF-2015 simulations.

Overall, the refinement of the parametrization of the ReaxFF potential by Yeon and van Duin (ReaxFF-2015) shows clear improvement over earlier parameterization by Fogarty et al. Inclusion of the water reaction with a 2-Ring defect (strained silica dimer) in the training set results in water-silica reactions in better agreement with *ab initio* MD simulations in terms of activation energy, reaction mechanism and the rate of TBO defect removal.

CHAPTER 5

INTERFACIAL AND HYDRATED SILICA GEL STRUCTURE MODELS BY CLASSICAL MD SIMULATION

5.1 Abstract

The development of interfacial silica gel layers plays a critical role in controlling the stability of the water-silica interface and the residual dissolution rate hence characteristics and layer structure of the gel is one of key unanswered questions in understanding the dissolution of silicate and related oxide glasses. In this chapter, the silica gel structure models were developed using atomistic computer simulations. A three-component interface model consisting of dense silica, silica gel, and bulk water was created to mimic the development of alteration layers during glass dissolution. Two methods were used to create the gel structures: one from de-polymerization of dense silica with silicon removed and the remaining dangling bonds saturated with hydrogen to form silanol groups; and, the other one from the remnant of a multicomponent silica glass by removing the soluble species such as B and Na. The former was used in the creation of the interfacial models.

The silica-gel-water (SGW) interface structure model was developed through the formation of a silica gel in contact with dense silica with a smooth transition from dense silica to silica gel, and then bulk water creating a water-silica gel interface and a pure water region to allow for the dissolution of silica. Through high temperature classical molecular dynamic (MD) simulations with the ReaxFF dissociative water-silica potential, the SGW models were allowed to evolve resulting in the growth of the silica gel into the water region of the model while the dense silica remains stable. The short range

features such as bond angles and interatomic distances of the gel layer experience littler variation while medium range structure features such as Q_n and ring size distributions become more consistent with dense silica due to the increases in fully coordinated SiO_4 tetraheda and the development of five-, six-, and seven-membered rings. Dissolved silica was formed in the water region with over 50% existing as silicic acid monomers (SiO_4H_4). The development of SGW models enables detailed understanding of the role of complex interfacial model systems plays in the dissolution of silicate glasses in aqueous environments.

5.2 Introduction

The long term stability of silica and silicate systems in aqueous environments has gained increased interest in recent years due to their wide spread use as catalyst supports and hydrogen storage materials [13,265-268] as well as their role in the regulating the stability of the earth's crust and other geological formations [1,4,5]. One of the critical technical applications of silica-based glasses is their role in the immobilization of nuclear waste, where the high composition tolerance and chemical stability, as well as relatively easy processing make these amorphous materials well-suited for the immobilization of medium and high level nuclear waste materials to solve the earth's most important energy and environmental challenges.

Silica dissolution has been characterized as a series of stages corresponding to the changes in the surface composition of the glass depending on the length of time the glass has been in contact with the water. The first two stages are relatively immediate surface effects including ion exchange of the cations in the glass with proton or

hydronium ions resulting in a fully hydroxylated surface which is depleted in network modifiers [178]. Once the initial surface changes have occurred, slow breakage of Si-O-Si linkages and similar bonds results in the formation of a silica gel surface layers and saturation of silica in the solution adjacent to the surface. At this stage the dissolution rate is slowed, and the glass is in temporary equilibrium with the surrounding aqueous solution resulting a residual rate of dissolution. Through unknown mechanisms, secondary precipitation phases can form on the surface of the gel structure and silica dissolution resumes which is known as the resumption rate stage. The precipitation of silicate crystalline phases that follow the Ostwald rule of stages is a result of the alteration layers trending toward more thermodynamically stable structures [269].

The residual dissolution rate is heavily influenced by the diffusion rate of the water molecules through the various gel/passivation/alteration layers which form at the water-silica interface. Despite the importance of these interfacial structures, details on the structure and properties of the silica gel layers are missing in the literature, and understanding of the gel layer and associated interfaces remains a grand challenge in understanding the dissolution behaviors of glasses.

Several recent experimental investigations on the dissolution of silicate glasses and the generation of interfacial phases have been reported using isotopically tagged glass samples to allow for an analysis of the movement of atomic species from the glass to solution and vice versa [185]. At this point, the number of interfacial phases that form (1-3), the width of the interfacial gel region (1-10+ microns thick), as well as how the gel layer affects the residual glass dissolution rate, is unknown, though it has been predicted that the interfacial silica gel layers are protective in nature [184,185,269].

From previous experimental studies on nuclear waste glasses, it has been suggested that the alteration layer is not a precipitate from the solution, but instead is the result of the reorganization of the remaining glass structure, which is modified after the removal of mobile and soluble species [147,185,270,271]. The silica rich gel has been analyzed by Raman spectroscopy to identify the changing connectivity of the silicon in the gel and the results indicated changes in the internal bonding environment of the network forming species [269]. The gel structure can have pore sizes less than 1 nm and decrease as they approach the surface, suggesting that the alteration layers acts as a molecular sieve that controls and regulates the diffusion of water and other mobile species through the gel layer [185].

Despite some recent progress gained of the gel layer through experimental studies, many questions remain concerning the structure and properties of silica gel layer formed during the dissolution of silicate glasses. These questions include the possible formation of multiple interfacial layers, how the structure and properties of the gel vary with the initial glass composition, and the change of activity of soluble species [178,272]. Additionally, due to the complex structure and nano-porosity of the silica gel at different stages of the glass dissolution process, analyzing the features of the interfacial layers is a great scientific challenge. Isotope tracing experiments combined with NMR (nuclear magnetic resonance) and FTIR (Fourier transform infrared spectroscopy) allow for the identification of some structural features, but difficulties with differentiating between atomic species in the water and the silicate, the effect of dehydration, and the long experimental time frames (26+ years) are still being overcome.

Computational methods provide insight into the glass dissolution process due to their ability to model the silica-water interactions with atomic accuracy that provides extremely detailed insight into the processes and reactions that govern silicate dissolution in aqueous environments.

Thus far, the majority of the computational investigations on water-silica systems has focused on the interactions between water and flat silica surfaces, and has been limited in terms of system size and time frames. For instance, hydroxylation of the silica surface has been studied using both *ab initio* and classical MD methods [81,85,86,90,110,152] as have the energies associated with breaking individual siloxane bonds [93,115,155,167,273]. These studies have been beneficial in developing an understanding of the immediate processes that occur during the interaction between water and silicates, but it has not addressed some of the larger length scale features of silica-water interactions which govern the dissolution of silicate glasses. These features are however important in understanding the kinetics of these reactions and the role of water diffusion in facilitating siloxane bond breakage.

Similarly, analysis of silica gels has been undertaken due to the interest in nanoconfined water as well as aerogel structures [134]. The existence of this so-called frozen or structured water has been identified both experimentally [56,58,109,124,133,274] and computationally [59,127,132,275] with the mechanisms which are responsible for its formation, such as the development of hydrogen bond networks and organization of water based on the surface charges, being identified computationally. The decrease in the diffusion of nano-confined water suggests that the formation of silica gels on the surface maybe passivating by limiting the diffusion of

water through the system. Extensive proton transport through the nanoconfined water has also been identified. It allows for movement of hydrogen species through the systems without requiring molecular diffusion [136]. However, the effect of bulk water next to the gel and the ability of the confined water to cause Si-O bond breakage have not been studied.

In addition, investigations on the solubility and polymerization of silica in water have been performed to identify if the silica gel structure was formed from an oversaturated solution [276,277]. The topic of silica solubility has been extensively studied experimentally due to its interest in the geological community with evaluation of the solubility limit of silica and its variation with temperature [27,162,278-280] as well as the formation of different polymeric forms in the saturated solution [157,158]. Computationally, due to limitations in simulation time frames combined with low silica reaction rates, especially in dilute conditions, there are relatively few studies on silica polymerization. Some *ab initio* work has been done on the varying stability of silica monomers, dimers, and trimers in water [246,281,282] as well as a study of polymerization reactions in ultra-saturated conditions using classical MD simulations [276,277]. All of the above studies have investigated the spontaneous polymerization of silica monomers in water, and do not account for the role of interfaces that may facilitate or hinder the polymerization reactions. Additionally, many of the theories which govern silicate dissolution in water suggest that the dissolution process slows when the water is silica saturated [178,186], but whether that is due to an increase in the activation energy for siloxane bond breakage, or an increase in polymerization reactions on the surface, has not been identified.

Limited investigation of the gel structures when in contact with water and dense silica has been performed almost exclusively through the use of kinetic Monte Carlo (KMC) method. KMC is a stochastic method of predicting evolution of a system based on known reaction mechanisms and reaction rates. KMC models have been effective in identifying different water diffusion regimes in nuclear waste glasses and the role of structural features such as non-bridging oxygen (NBO) and boroxyl rings on the rate of interfacial gel formation [95,168,202,203]. The drawbacks of using KMC is that it lacks atomic level details, and it does not provide mechanisms that govern the surface reorganization, but instead they are based reaction rates from experimental or theoretical studies.

While the above computational work has made significant progress in understanding certain aspects of the processes during silicate glass dissolution such as the investigation of the initial hydroxylation and hydrolysis process on flat silica surfaces, the limited diffusion kinetics of nano-confined water, and polymerization of silica in solution, they are each evaluated independently from one another and often under different context and circumstances. How these simultaneous processes govern the silicate glass dissolution in aqueous environment is unclear. This is especially critical since silica-gel and gel-water interfaces can have an impact on the structure and dynamics of the water molecules through the interface. What is missing from the literature is an understanding of the role that the interface plays in the dissolution of silicate glasses, and how the silica-water reactions, water and hydration species diffusion, and changing concentration of dissolved silica affect each other. To our knowledge, this is the first model of its kind that uses reactive force field (ReaxFF)

based classical MD simulations to develop an interfacial model consisting of not just bulk water and dense silica, but also an interfacial silica gel region, to understand the important role that the alteration layers play in the dissolution of silicate glasses. The development and analysis of the interfacial models will provide information on the interfaces, how the gel evolves during its interaction with water, the flux of water and silica through the interface, and more. In this chapter, the development of interfacial gel structures are investigated, and then input into a three component model consisting of dense silica, silica gel, and bulk water regions. The effect of these regions on the structure of the silica and gel layers are examined as the system evolves as a function of time and temperature.

5.3 Simulation Methods

5.3.1 Computational Simulation Methods

The classical MD simulations in this work were performed using the dissociative water-silica potential ReaxFF, developed by van Duin, Goddard, and coworkers and parametrized by Yeon and van Duin [82,97,98]. The use of ReaxFF allows for the simulation of bond breakage and formation since the interatomic distance between atomic pairs identifies the bonding states, and is revaluated at every frame to allow for a smooth transition from bonded to unbonded systems. The ability to simulate reactions without specifically including them in the parametrization is due to a complex potential consisting of ten individual energy terms which account for different bonding conditions, all of which decrease smoothly with distance, avoiding sudden step-wise changes in system energy [82,98]. Parametrization of the ReaxFF potential for water-silica systems

used here is an improvement over a version by Fogarty et al. in 2010 which resulted in negative activation energies for the breakage of strained siloxane bonds, which was corrected in the version by Yeon and van Duin [85,98]. ReaxFF has been used with success in a wide variety of water-silica systems identifying the role of humidity on surface structures [283], the formation of silica nanocages [284], the structure of hydrated calcium silicates [132], and water confined in the silicate [285]. In this work, ReaxFF implemented in the open source code LAMMPS, a classical MD code distributed by Sandia National Laboratories, was used in the simulations due to its high computational efficiency [214].

5.3.2 Silica Gel Structure Formation

Due to the uncertainty in the experimental literature describing the structure of the interfacial gels in silica dissolution, two different methods were used to create silica gel structures, which were compared in detail in this work with an aim to identify which is consistent with the available experimental data. Both methods rely on the concept that the silica-enriched gel interfacial layers are remnants of the initial multi-component glass structure as identified by Gin et al. [185]. In the first method, a de-polymerization process was used that is based on the assumption that silica dissolves in aqueous environments from the formation of individual SiO_4H_4 in the solution, and SiO_4 units are removed one at a time [88]. To create this de-polymerized silica gel structure, a 3000 atom dense silica glass system was used as the basis from which silicon atoms were randomly removed one by one, and the remaining non-bridging oxygen ions were hydrogen terminated creating silanol (Si-OH) groups. By varying the number of silicon

atoms removed, the connectivity and amount of free volume introduced to the structure was controlled. Of the 1000 silicon atoms present in the structure either 20% (200 Si), 40% (400 Si), or 60% (600 Si) were removed, forming DSG-20, DSG-40, or DSG-60 nanoporous silica systems. Once the nanoporous silica was generated, the system was hydrated by overlaying the simulation cell with a large box of water molecules at a density of 1 g/cm^3. Any water molecules within 1Å of atoms in the gel structure or which were outside the simulation cell were removed which ensures that the system is fully hydrated. Due to the randomized and unique structure of different silica models with the same composition, all simulations were performed in triplicate with each generated from different random processes, and final structure and properties are presented as an average of three simulations with the standard deviation. Final systems vary depending on the number of silica (20%, 40%, 60%) removed and data on system sizes and silica concentrations included in Table 0-2.

Another method of the gel structure generation is from the boroalumiosilicate glass structure generated from MD simulations [193]. This is based on the hypothesis that the nanoporous silica gel is the remnant (relic) structure from the dissolution of soluble species such as sodium, calcium, and boron, as well as other network modifiers and formers from the multicomponent borosilicate glasses used for nuclear waste immobilization. This results in a silica rich gel layer, the aspects of which are still under debate in the literature [178]. To mimic this process, a classical MD potential was developed and used to create a multicomponent glass model at a composition similar to those used in the immobilization of nuclear waste from which non-silica components will

be removed leaving behind a silica rich gel layer. The gel structures generated from this method are compared to the de-polymerized gel structures discussed previously.

Unfortunately, most classical MD potentials currently available do not contain the functionality for the simulation of boron, aluminum, and silicon that has been a significant barrier in the simulation of complex multi-component oxides. A recent potential by Deng and Du has been developed which is capable of replicating both three-fold and four-fold coordination of boron along with aluminum, silicon, and sodium parameters using a Kieu potential framework which was used here [193]. It should be noted that simulation of the dissolution of multicomponent glasses cannot be performed with the potential by Deng and Du, because it does not include parametrization for water interactions. For the selection of the initial composition, effort was made to obtain multicomponent glass structures similar to the proposed international simple glass (ISG) composition, which was selected by an international consortium to standardize investigation of the dissolution of nuclear waste glasses [26]. Based on the available classical MD potentials, a further simplification of the ISG composition was created, simplified ISG (sISG), to approximate the relative concentration of network formers and modifiers to mimic the structure of ISG compositions. Compositions for the ISG and sISG glasses are included in Table 0-1, and additional information on the structure and properties of the sISG compositions simulated with the potential by Deng and Du is included in Reference [193].

Table 0-1: Simplified ISG and ISG glass compositions [66].

	SiO_2 (wt%)	B_2O_3 (wt%)	Na_2O (wt%)	Al_2O_3 (wt%)	CaO (wt%)	ZrO_2 (wt%)
sISG	54.6	23.6	16.3	5.5	0.0	0.0
ISG	60.2	16.0	12.6	3.8	5.7	1.7

sISG structure models containing 3396 atoms were obtained from Deng and Du and used to create the remnant silica gels [193]. To simulate the removal of the mobile species in the glass and create a silica gel, all the sodium, boron, and aluminum, were removed, and any resulting NBO were terminated with hydrogen. In experimental studies, it was found that sodium ion exchange with proton or hydronium ions occurs in the first stages of water-silica interactions, which is followed by the removal of boron due to its high water solubility [178,269]. Aluminum has shown some stability, and can remain in the gel structure where it may have an effect on the dissolution rate [178,269]. Since the dissolution of pure silica is the focus of this study, the aluminum atoms are also removed, but aluminum could be kept in the system for future studies. The result is a fragmented nanoporous silica structure, which was then hydrated by overlaying a box of water molecules at a density of $1 g/cm^3$ and removing any molecules which overlapped with the nanoporous silica. System details for the silica gels developed from the de-polymerized silica process (DSG) and from the remnant of the sISG systems (RSG) are included in Table 0-2, and the schematic outline of the development of both gel structures is included in Figure 0-1.

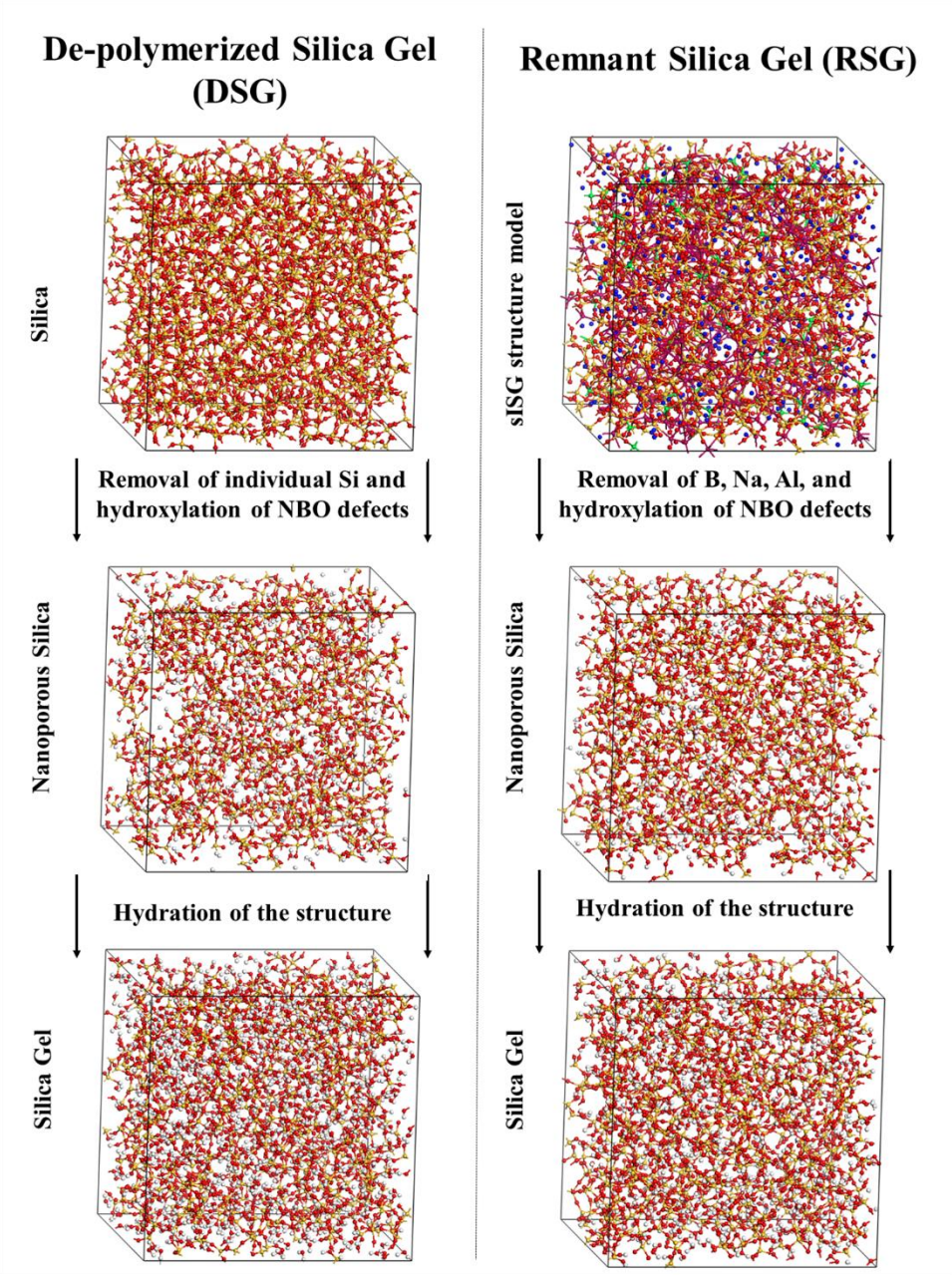

Figure 0-1: Outline of the generation of DSG or RSG systems. Red is oxygen, yellow is silicon, white is hydrogen, aluminum is green, boron is purple, and sodium is blue.

Table 0-2: Composition and density for DSG and RSG silica gel structures. The standard deviation is from three unique silica gel systems.

	% Network Formers Removed	Mole % SiO_2	Mole % H_2O	Density (g/cm^3)
DSG-20	20 (Si)	62.26±1.19	37.74±1.19	1.91±0.01
DSG-40	40 (Si)	40.77±0.06	59.23±0.06	1.57±0.01
DSG-60	60 (Si)	23.66±0.07	76.34±0.07	1.25±0.01
RSG	36 (Al, B)	45.28±1.28	54.72±1.28	1.66±0.02

After the DSG and RSG systems were created, MD simulations with ReaxFF force field were performed for 30ps using a 0.25 fs time step. The temperature was controlled through the use of a canonical (NVT) ensemble, which controls the number (N), volume (V), and temperature (T) of the simulation through the use of a Nosé-Hoover thermostat with a damping time of one hundred time steps. The relaxed silica gel systems were then analyzed for differences in structure between the two methods as well as compared to the available literature on silicate gels. Details of this comparison is included in Section 5.4.1.

5.3.3 Silica-Gel-Water (SGW) Interface Model Formation

A multi-phase silica dissolution model was developed in order to allow for the investigation of the role of a silica gel interfacial layer on the dissolution of pure silica glass. The SGW model is composed of three sections, silica with a density of 2.2 g/cm^3, a gel structure with a density of ~1.6 g/cm^3, and bulk water, with a density of 1 g/cm^3. To create the SGW model, first, a 3000 atom dense silica model (35Åx35Åx35Å simulation cell) was created from a melt-and-quench procedure using the classical MD

parameters described by Teter [86]. To create the dense 6000 atom silica system the structure was repeated in the z-dimension, forming the 3000 atom dense silica region and a second 3000 atom block of dense silica which is the basis of the silica gel structure (35Åx35Åx70Å). Next, the de-polymerization methods of creating silica gels, discussed in Section 5.3.2, was performed on one half of the dense silica model, removing 400 of the 1000 silicon present and hydroxylating the NBO. A snapshot of the resulting structure is included in Figure 0-2.b. This formed a dense silica system in one half of the model, connected to a fragmented nanoporous silica structure in the other half, with a continuous interface between the two regions. By extending the z-dimension by 35Å, a vacuum region and a set of interfaces was created, one in contact with dense silica, and the other with nanoporous silica. Then the structure was hydrated by overlaying a large box of pure water molecules on the combined silica and nanoporous silica structure, and removing any water molecules outside the simulation cell or overlapping with the initial structures. The final model has a simulation size of 35Åx35Åx105Å and contains 11692 atoms. A schematic of the development of the SGW model is included in Figure 0-2.

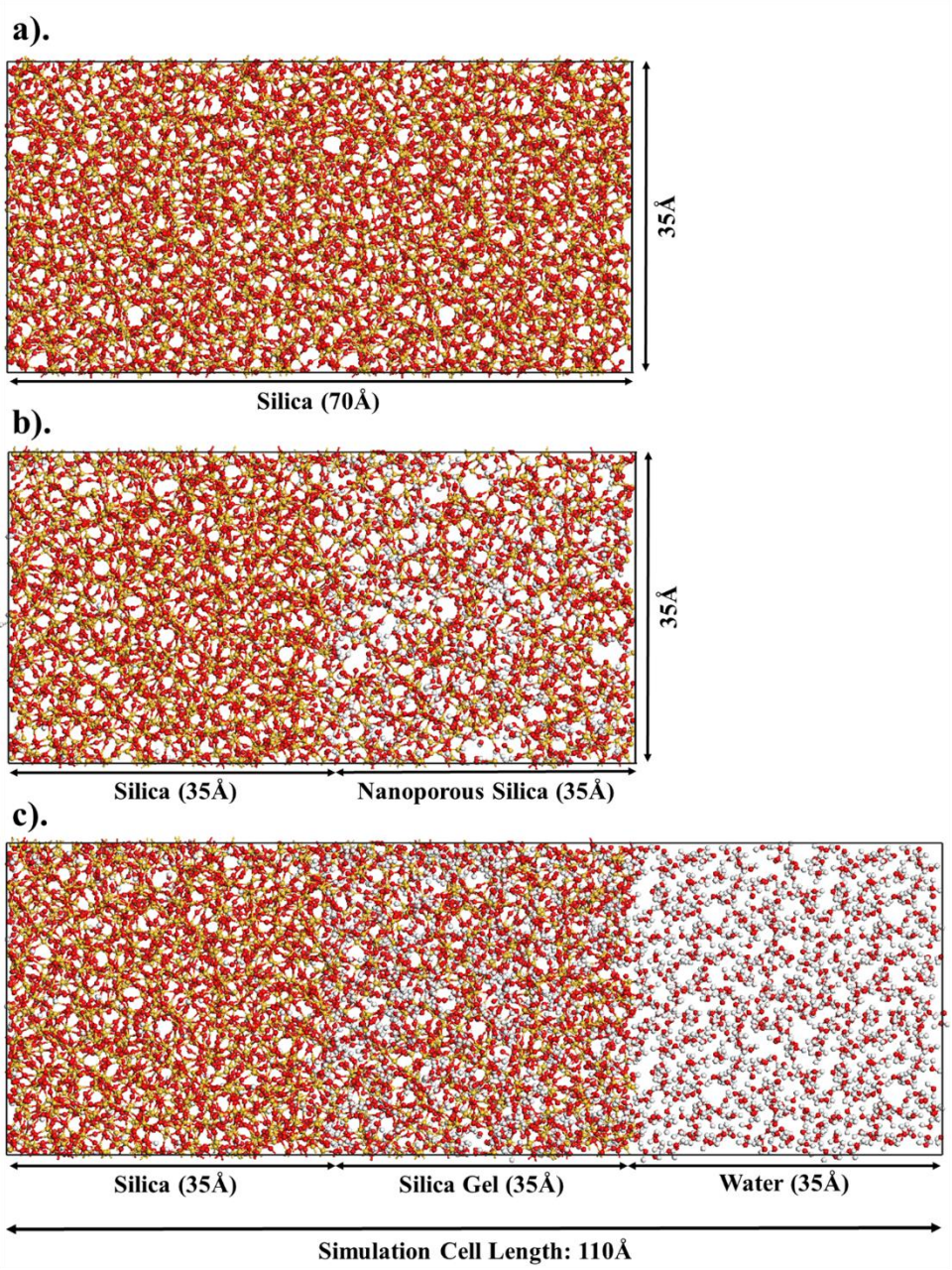

Figure 0-2: Schematic outline of the generation of the SGW model systems. Red is oxygen, yellow is silicon, and white is hydrogen.

For the dynamics of the SGW model, the system underwent classical MD simulation using the aforementioned ReaxFF forcefield for 1 ns using a 0.25 fs time step, to control the fast dynamics of the light hydrogen atoms in the system. In order to

accelerate the dynamics of the water-silica reactions the temperature for the simulation was increased to 300K, 500K, 700K, or 900K and regulated by a Nosé-Hoover thermostat with a damping time of one hundred time steps. By increasing the temperature during the simulation longer time frames can be accessed by speeding up the dynamics, in a process termed temperature-accelerated dynamics (TAD) [286]. Since the breakage of siloxane bonds are rare events, especially in the small time frames and systems sizes investigated by computational methods, increasing the temperature (even to values greater than 1100K) decreases the reaction energy barriers, allowing for the faster evolution of the structure [286] . TAD methods have been used for the evaluation of surface diffusion, studies of crystal growth, and the simulation of proteins [286-288]. TAD simulation methods typically require a screening of individual reactions which may occur, since by increasing the temperature, as was used here, the reactions as well as the rate constants are affected, resulting in differences in the ratio of high- and low-barrier reactions [286]. In the case of the evolution of the SGW, since the amount of reorganization is significant and the final structure is of primary interest, the differences in the reaction rates and rate constants are not considered. Therefore, by running the simulations at 300K-900K it is expected that the system at 900K will have evolved for longer than the simulation which was ran at 300K, resulting in greater reorganization of the structure and a more reactive interface and defect sites. Once the SGW structure models have been relaxed for 1 ns at 300-900K the temperature is then decreased to 300K, and 30ps of NVT relaxation is preformed to cool down the systems and remove any high temperature vibrations which may affect analysis. The final relaxation at 300K also allows for the deconvolution of any

high temperature structures which may have been inadvertently developed during the simulation. The changing temperature over the course of the simulations are outlined in Figure 0-3. Analysis of the structural changes in the SGW model after cooling is discussed in Section 5.4.3.

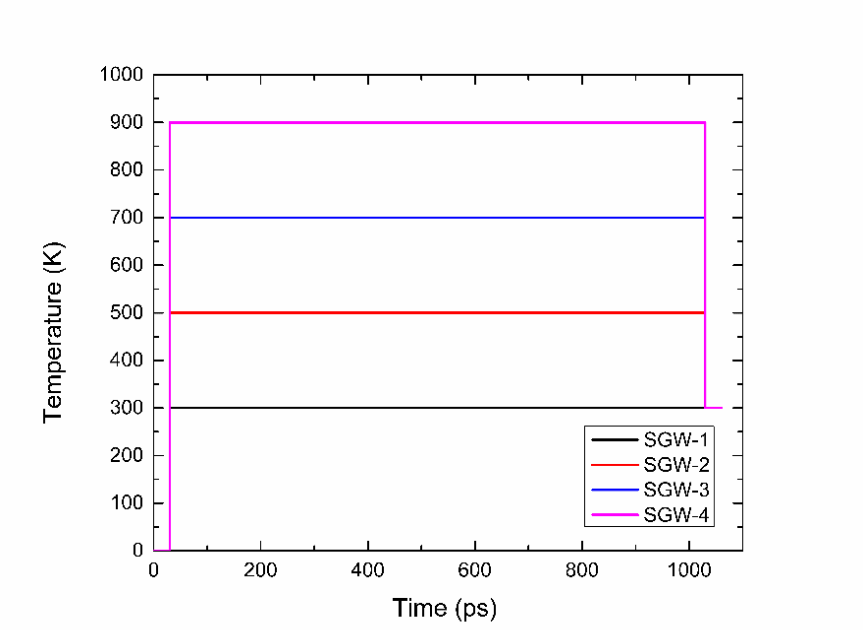

Figure 0-3: Changing temperature with time for the four different SGW model structures.

5.4 Results

5.4.1 Silica Gel Structures

The structure of the interfacial gel layer is critical to regulating the dissolution process of silica, and there is limited knowledge in the literature of the different hydrated alteration and interfacial gel layers. Based on what is known about the silica gel, two different computational methods were used to develop silica gel layer structure with one of which being the result of the de-polymerization of a dense silica structure and the other being a silica remnant of the simplified ISG glass. Data from the study of silica

dissolution in ISG indicated that only 1:600 silicon atoms in the gel structure had been deposited from polymerization in solution, and it is therefore expected that the remnant structure would be more consistent with what is seen experimentally for the dissolution of multicomponent glasses [185]. The identification of a gel structure which exhibits the features of the remnant silica gel formed on the surface of ISG was explored with an aim to develop a structure model which exhibits relevance to silica gels from multicomponent glass dissolution. Snapshots of two different silica gel structures are included in Figure 0-1, and the method developing silica gels is discussed in Section 5.3.2, with a detailed analysis of their structures is included below.

Characterization of the similarities and differences between the two methods of creating silica gel structures is used as justification for using one over the other in the SGW model, whose development is discussed in Section 5.3.3 and analyzed in Section 5.4.2 and 5.4.3. An analysis of the short range features of the silica gel models including the internal structure of the SiO_4 tetrahedron, such as bond angles and distances, provides insight into the perturbation of the localized structure due to pressure or temperature affects in the gel, and also speaks to the accuracy of the classical MD potential used in the simulations. Analysis of the bond angles and bond distances was collected from compiling interatomic distances from 30,000 snapshots of the silica gel structures collected from the 30ps NVT run to develop bond angle distributions (BAD) and pair distribution functions (PDF) using a cut-off of 2.25Å. Oxygen atoms located in the silica and water were separated for analysis to identify features which may be unique to one phase or the other. BAD and PDF analysis takes into account variation in the interatomic distances and angles due to vibration of the atomic positions from

temperature and the amorphous nature of the material, and is therefore commonly used in the analysis of glassy systems. The peak and full-width-half-max (FWHM) values for the BAD and PDF data of different atomic pairs of interest are included in Table 0-3, as well as values for pure silica, water, and experimental data.

For the silica gel structures many of the interatomic distances and bond angles show no change with the method of silica gel development because their existence in a gel rather than in bulk water or silica, or compared to experiment, and include Si-O, O_w-H_w, (w=water) and H_w-H_w interatomic distances as well as, O-Si-O, Si-O-Si, and H_w-O_w-H_w bond angles (Table 0-3). Several of the other structural features experience some variation including the Si-OH bond angle which is ~124º in the work here compared to ~118º from *ab initio* methods, and is a result of the use of the ReaxFF potential (Chapter 4 Section 4.4.1). The primary effect of the structure on the bond angles and bond distances appears in the O_w-O_w interatomic distance which increases slightly with decreasing silica concentration (Table 0-3) in the DSG structures from 2.73Å to 2.88Å, with an experimental and bulk value of ~2.85Å. A shorter O_w-O_w distance of 2.73±0.02Å was identified as the O_w-O_w interatomic distance in the formation of a distorted hexagonal layer in frozen water suggesting that there may be some solidification or crystallization of the highly confined water in the systems with the highest silica concentration [289,290]. Alternatively, the lengthening of the O_w-O_w distance may be the result of small isolated cluster of water molecules which have been reported to have O_w-O_w bond lengths of 2.94Å by *ab initio* simulations [73].

A similar trend is seen in the low O_w-H_w-O_w angle in the silica gels relative to the bulk water and experimental values, with O_w-H_w-O_w angles of ~155º in ice monolayers

formed during the nanoconfinement of water using classical MD methods while O_w-H_w-O_w angles in bulk water continue to be ~164^o [291]. The ~11^o difference in the O_w-H_w-O_w bond for pure water from simulation (165^o) and experiment (174^o) may be a result of the classical MD potential with *ab initio* simulations reporting O_w-H_w-O_w angles between 171.6^o-174.5^o depending on the exchange-correlation functional used [76,292]. Even so, the difference of the O_w-H_w-O_w bond angle up to 11^o between the bulk and nanoconfined water in the gel region is still significant, even when accounting for the approximation due to in the ReaxFF potential. The formation of frozen or structured confined water at ambient conditions has been identified by proton NMR and neutron diffraction and is noted to occur within 10Å of silica surface by simulations [58-61]. Interestingly, no change in the H_w-O_w-H_w bond angle from 104^o as would be expected for liquid water, to 109^o, which was observed in hexagonal ice, occurs suggesting that there exists some ordering of the water molecules in the confined region, but the structure is not the crystalline form of ice [293,294]. A conclusive statement on the structure of the water inside the silica gel is under investigation for future studies, but it appears that confinement of the water causes some structural changes in the hydrogen bonded water network.

Table 0-3: Interatomic distances and bond angles for the DSG and RSG silica gels structures as well as bulk water, silica, and experimental data. The peak of the BAD or PDF is presented along with the FWHM value in parenthesis.

	DSG-20	DSG-40	DSG-60	RSG	H_2O/SiO_2	Expt.
Si-O dist. (Å)	1.58 (0.13)	1.58 (0.14)	1.58 (0.13)	1.58 (0.15)	1.58 (0.11)	1.61[a]
O-O dist. (Å)	2.58 (0.34)	2.58 (0.31)	2.59 (0.31)	2.58 (0.34)	2.55 (0.26)	2.65[b]
Si-Si dist. (Å)	3.11 (0.18)	3.10 (0.18)	3.10 (0.16)	3.12 (0.18)	3.06 (0.14)	3.1[c]
O-Si-O angle (°)	108 (18)	109 (17)	109 (17)	108 (18)	108 (16)	109.4[b]
Si-O-Si angle (°)	154 (30)	156 (28)	153 (28)	156 (28)	152 (22)	153[b]
Si-O-H angle (°)	124 (11)	124 (11)	124 (11)	123 (13)	N/A	118.1[d]
O_w-H_w dist. (Å)	0.97 (0.10)	0.97 (0.11)	0.97 (0.08)	0.97 (0.11)	0.97 (0.06)	0.98[e]
O_w-O_w dist. (Å)	2.73 (0.94)	2.85 (1.20)	2.88 (1.60)	2.71 (1.40)	2.82 (0.41)	2.85[f]
H_w-H_w dist. (Å)	1.53 (0.20)	1.51 (0.20)	1.51 (0.19)	1.56 (0.24)	1.54 (0.12)	1.56[g]
O_w-H_w-O_w angle (°)	152 (42)	152 (43)	152 (41)	154 (42)	165 (25)	174[h]
H_w-O_w-H_w angle (°)	104 (16)	104 (17)	103 (18)	105 (18)	104 (15)	104.5[f]

[a]Neutron diffraction [39] [b]Electron diffraction [32] [c]Large angle x-ray scattering [295] [d]DFT with 6-31G** Gaussian basis set [236] [e]Electron diffraction [296] [f]Neutron scattering [297] [g]Neutron diffraction [298] [h]Molecular beam electric resonance spectroscopy [292].

To evaluate longer range features of the silica gel, the Q_n speciation of the backbone structure is performed which provides insight into the connectivity of the silica by identifying the number of bridging oxygen, n. As the number of silicon that are removed from the structure is increased in the DSG models, the concentration of Q_n

species changes from a peak in Q_3 concentration in DSG-20, which still contains 80% of the original silicon, to Q_2 in DSG-40 and Q_1 in DSG-60 (Figure 0-4.a). This is due to the introduction of broken siloxane bonds with the removal of silicon. For the RSG model, both Q_3 and Q_2 species are most common at ~38%, and its Q_n distribution matches closely with the DSG-40 model with comparable concentrations of Q_1, Q_2, and Q_4 species (Figure 0-4.a). The increased concentration of Q_3 species in the RSG may be due to the sodium in the original ISG structure since sodium with a positive charge can break one bridging oxygen forming Si-O---Na, resulting in a preference for Q_3 species [185]. This demonstrates that there is an effect of the initial glass composition on the silica structure after the formation of silica gel systems.

Analysis of the ring structure distribution provides insight into the intermediate range order of the glasses with a ring identified by the number of silicon it contains [223]. With decreasing silicon concentration, the ring structure breaks down which is seen in the DSG systems with changing silica contents (Figure 0-4.b). For the DSG-20 structure, which has the highest silicon concentration, the ring structure distribution has a clear peak at six which is the most common ring structure formed in pure silica glasses as well as cristobalite [193,235,299]. In the DSG-40 and DSG-60 models, the ring structure has fragmented with much lower concentrations of all ring structures in the DSG-40 system and only ring sizes less than seven for DSG-60. As an interesting note in the DSG-60 system, which only contains 24 mole percent silica, there is an increase in the number of two-membered rings that are surface defects which form preferentially on silica surfaces [86,87,148]. The stability of two-membered rings has been included in the parametrization of the ReaxFF forcefield that may cause their

formation during the de-polymerization of the structure [98]. For the RSG model, the ring-size distribution matches most closely with the DSG-40 system, which has a comparable distribution. The primary difference is a higher concentration of five-membered rings in the RSG system which may be due to the remnant of the ISG glass from which the gel is formed. Ring structure analysis of the sISG composition had a peak concentration of seven-membered rings across all the network formers in the system (Si, B, Al), and silicon may be more prevalent in five membered rings or the removal of a single boron from a six-membered ring may allow for the formation of a smaller five membered ring composed of pure silica accounting for its increased concentration in RSG systems [193]. Without more in depth analysis of the ring size distribution of the initial sISG structure, which is outside the scope of this paper, the nature of the peak at five-membered peak in the RSG ring size distribution cannot be analyzed further.

Overall, the RSG system is most consistent with the DSG-40 structure, in terms of both short range order, such as interatomic distances and bond angles, slightly longer range coordination features, such as Si Q_n distributions, and in the intermediate range order in the ring structure analysis. Therefore, the DSG-40 model is used as the silica gel in the development of the SGW interfacial models.

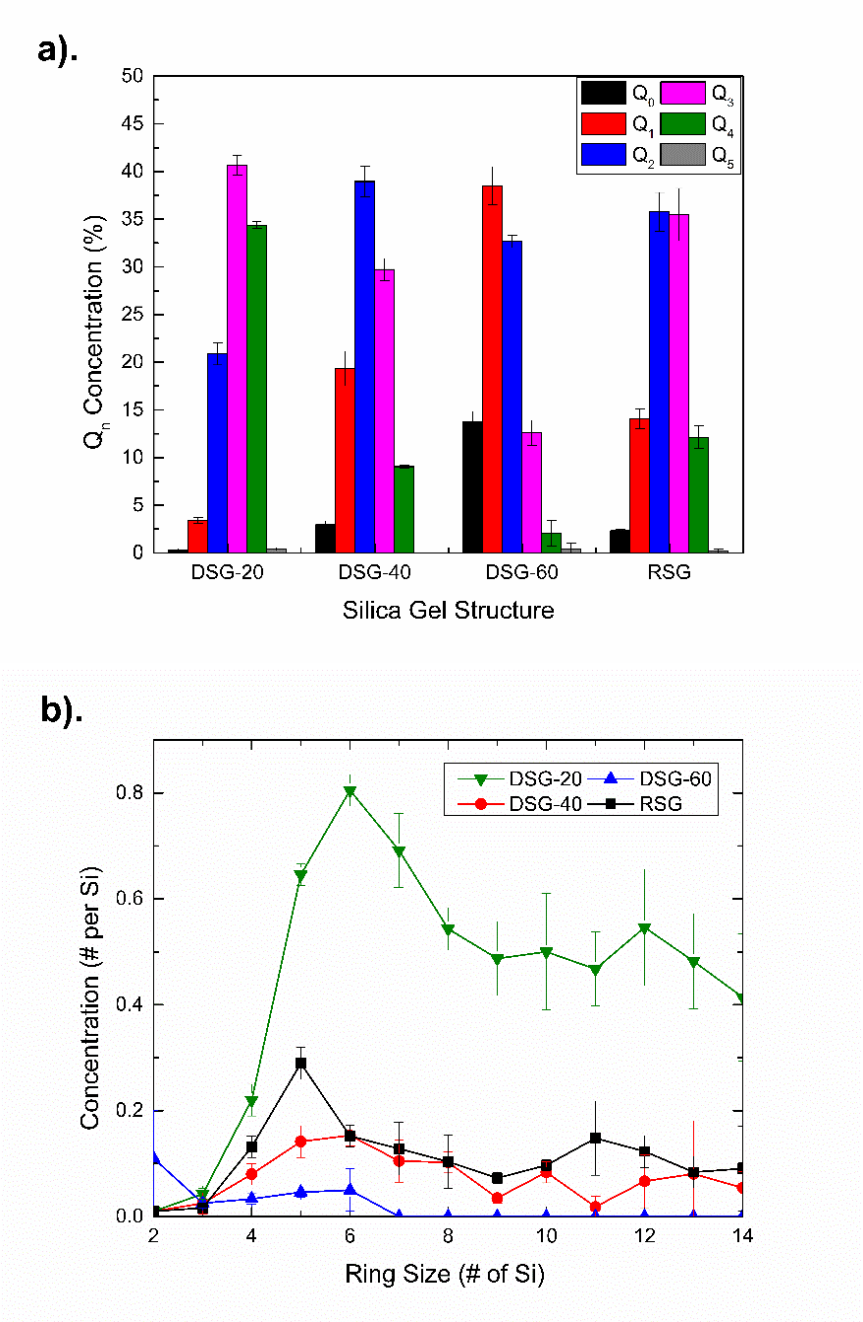

Figure 0-4: (a) Qn distribution and (b) ring size distribution of the DSG and RSG silica gel structures. Error bars are the standard deviation of three unique simulations.

During the course of the simulations, reactions between the aqueous solution and the surface occur that can cause the disassociation of the water molecules. The formation of OH^- and H_3O^+ species caused by splitting of water molecules has an

activation energy of 0.44eV reported using *ab initio* Car-Parinello molecular dynamic computational methods for water in clusters, and the effect may be exacerbated when water is located in small pores, with limited opportunities to recombine [135]. Additionally, when significant reorganization is occurring H_2 or O_2 molecules may form due to an excess of protons or oxygen in the solution, and stable concentrations of dissolved gases exist in natural aqueous systems [300]. During analysis of the water inside the gel structures it was found that the majority of the solution is molecular water, 97%+ in DSG systems and ~95% in the RSG system (Table 0-4). The remaining was composed of either hydroxide (OH^-), hydronium (H_3O^+), hydrogen (H_2) or oxygen (O_2) molecules.

In the DSG systems low levels of OH^- and H_3O^+ ions were identified, with H_3O^+ ions being ~2x the concentration of the OH^-, suggesting that the systems is slightly acidic. This is also confirmed by an enrichment of the solution in hydrogen atoms over the entire solvent with increasing H:O ratios with decreasing silica concentrations. Stable concentrations of H_3O^+ molecules have been identified in a number of different computational studies since diffusion of protons via hydrogen hoping requires their formation as intermediate states [75,136]. The higher concentration of H_2 in the solution may be counteracted by low levels of coordination defects, such as NBO, which can result in a silica structure with slightly elevated concentrations of hydrogen or oxygen.

The analysis of the remnant structure is more complicated since the use of the initial ISG composition generates a system rich in oxygen relative to hydrogen since there is a high concentration of NBO's which are terminated by the Na^+ network formers removed during the formation of the gel. In the RSG systems the water molecule

concentration in the solute is slightly lower, at 95%, and rather than forming H_3O^+ ions and H_2 molecules, OH^- and O_2 molecules are formed indicating that the system is basic. The dissolution rate of silicates is known to vary with pH with residual dissolution rates in solution with pH less than seven being lower than in the basic conditions with pH values up eleven resulting in faster dissolution [27,165,301,302]. In many experimental studies of long term dissolution of silicate based glasses buffering solutions are used to bring the pH to seven in order to remove any of the aforementioned pH affects [184,185]. Therefore, the higher concentration of pure water molecules seen in the DSG structures is preferred over the RSG systems in order to remove any pH effects in the systems. If RSG systems are used in the future, care should be taken to remove any of the extra OH^- and O_2 molecules which are spontaneously formed, and an attempt to develop a mass-balance based on the Q_n speciation of the silica should be considered.

Table 0-4: Composition of aqueous solution in DSG or RSG silica gel systems. The error bars are equal to the standard deviation of three different structures.

Mole (%)	H_2O	OH^-	H_3O^+	H_2	O_2	H:O Ratio
DSG-20	97.82±0.75	0.63±0.52	1.05±0.60	0.42±0.30	0.00±0.00	2.01±0.01
DSG-40	98.17±0.62	0.63±0.52	1.05±1.08	2.95±0.60	0.11±0.15	2.06±0.01
DSG-60	98.90±0.38	0.42±0.60	0.00±0.00	5.06±1.03	0.42±0.60	2.08±0.02
RSG	94.85±1.86	3.38±0.79	0.00±0.00	0.00±0.00	3.90±1.87	1.82±0.07

5.4.2 Growth Silica, Gel, and Water Regions in SGW Models

Through comparison of silica gel structures, a system that is most comparable to those formed from the remnant of a multicomponent glass was selected as the interfacial region between the dense silica and bulk water regions of the model. Once

the SGW models have been developed (described in Section 5.3.3), an analysis of their changing structure during the evolution of the model was conducted to provide insight into how the silica-gel and gel-water interfaces evolve as a function of time and treatment temperature. For example, the growth of the gel region into either the dense silica or water can be identified as well as changes in silica concentrations indicating from where in the system the silica is dissolving into the water. During the course of the simulation, growth and shrinkage in different regions is expected as atoms diffuse from one region to each other. Snapshot of the final structures for the SGW models are included in Figure 0-5.

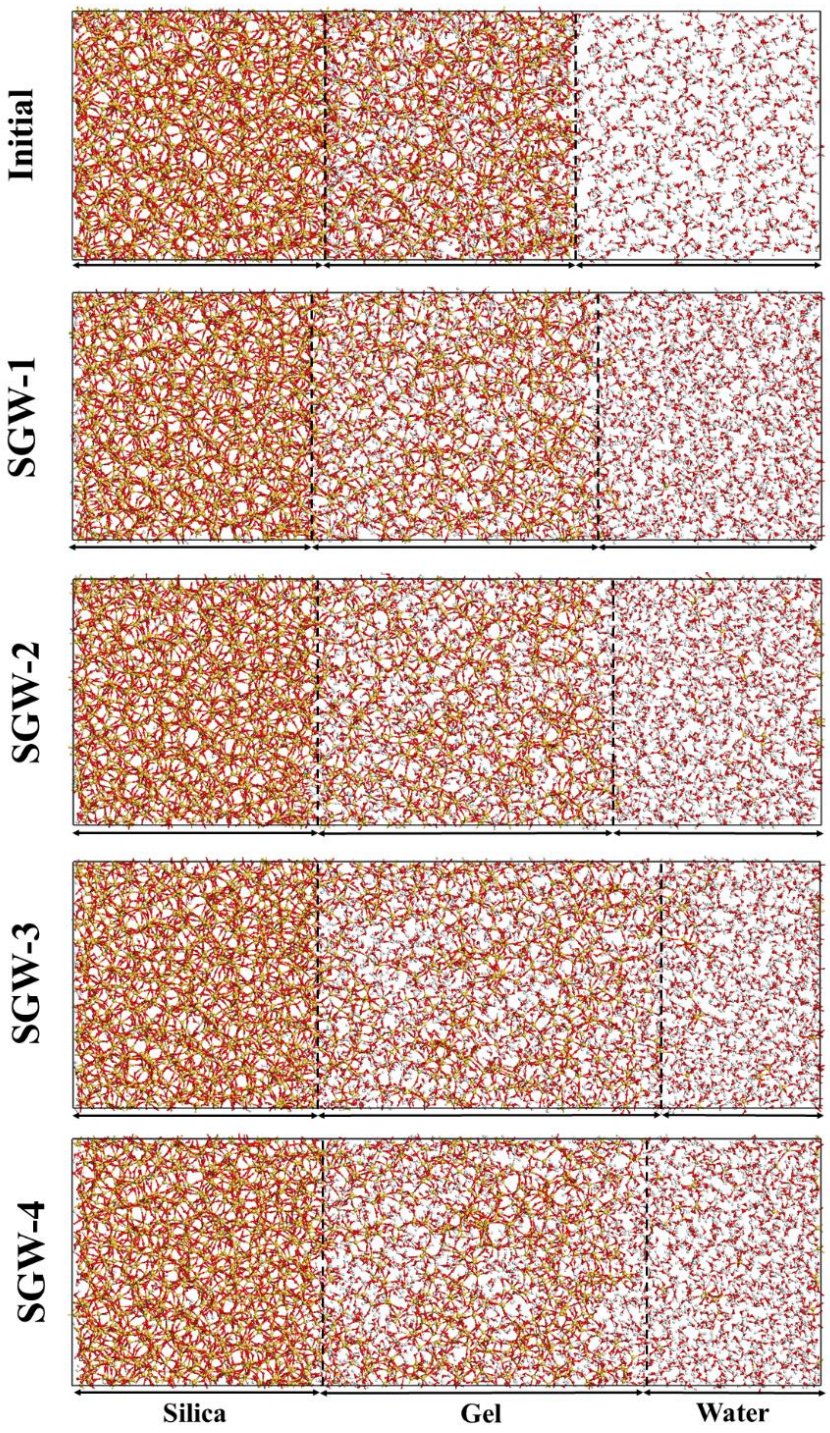

Figure 0-5: Snapshot of the final SGW structures as well as the initial configuration. Red is oxygen, yellow is silicon, and white is hydrogen. Dotted lines represent the transition between the silica-gel regions (left) and gel-water regions (right).

To separate the regions into silica and gel regions, the analysis of silica density as a function of depth from the surface was used by slicing the simulation into 2Å sections along the z-axis, and then counting the number of SiO_4 tetrahedra in each region. In order to be classified as a silica region, the density of SiO_2 had to be greater than 2 g/cm^3, ninety percent of the density of experimental silica (2.2g.cm^3), and the gel region had a silica density of greater than 1.0 g/cm^3, 10% less than half the density of silica. During the course of the simulations, silica diffuses away from the gel surface and into the bulk water resulting in a measurable quantity of silica in the aqueous region. Therefore, regions of the structure which had a silica density of less than 0.2g/cm^3 were considered to be water regions due to their low concentration of silica species. The selection of these cut-off value corresponds to naturally occurring breaks in the Z-density profile of the silica species between the regions (Figure 0-6).

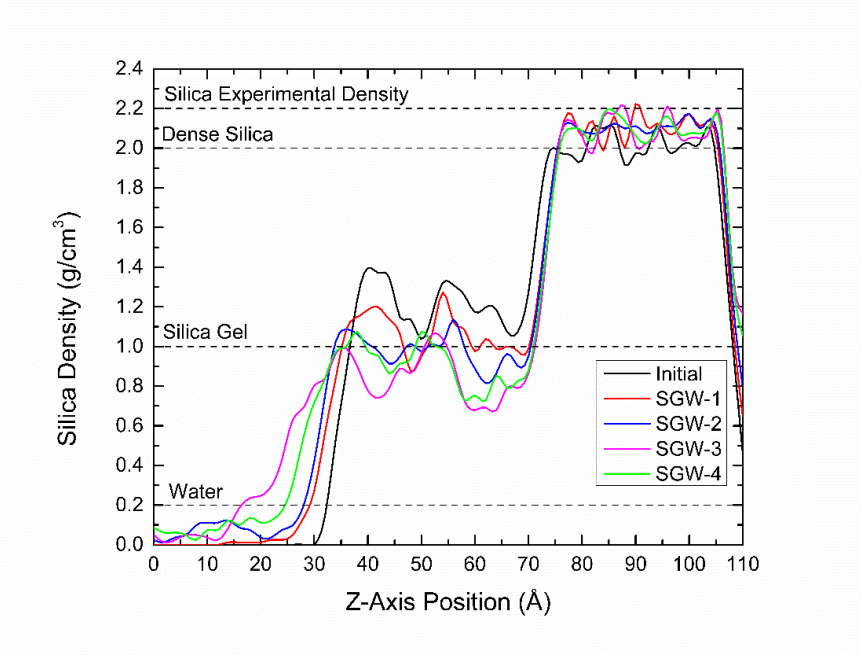

Figure 0-6: Z-density profile of silica density in SGW models.

Even for the SGW-4 simulation, the structure that has undergone the most evolution at a high temperature relaxation, differentiation between the three regions is clear with the silica region being the most stable with a consistent width of 30Å and a silica density of 2.07±0.02g/cm^3. Rather, the majority of the structural rearrangement occurs in the gel and water regions with an advancement of the gel-water interface into the water region. In Figure 0-7 and Table 0-5, the gel region expands into the water region due to the diffusion of silica species away from the surface and into the water resulting in a decrease in the width. Some of the increase in the gel region and decrease in the water region is due to the expansion of the gel-water interface with an initial thickness of ~4Å consistent with the initial thickness of the silica-gel interface (Table 0-5). The gel-water interface increases as the simulation evolves to 18Å in the SGW-3 model and then slightly contracts to 14Å for the SGW-4 structure. The lack of the development of a wider gel-silica interface or dissolution of bulk silica may be due to the inability of water molecules to diffuse through the interface into bulk silica, a process which might take a much longer time than those sampled in these simulations (around 1 ns). Not surprisingly, this indicates that the water-gel interface is more unstable than the gel-silica interface, and to gain a detailed understanding of the process by which silica dissolves into solution, a more in-depth analysis of silica-gel interfaces is required.

Table 0-5: Width of the silica, gel, and water regions and their interfaces in the SGW models as well as the initial SGW structure.

Region	Water (Å)	Water-Gel (Å)	Gel (Å)	Gel-Silica (Å)	Silica (Å)
Initial	32	4	32	6	32
SGW-1	28	8	34	6	30
SGW-2	26	8	36	6	30
SGW-3	16	18	36	6	30
SGW-4	24	14	32	6	30

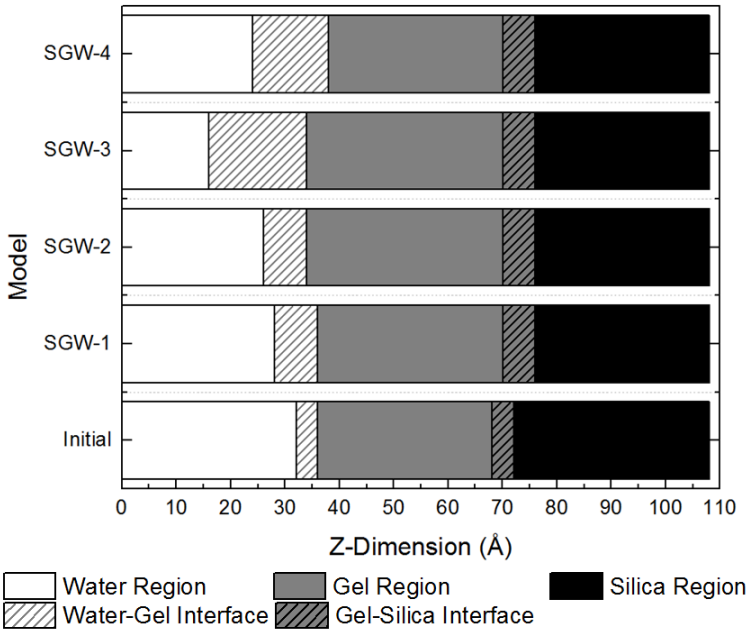

Figure 0-7: Schematic outline of width of the silica, gel, and water regions of the SGW model and their interfaces.

5.4.3 Structural Analysis of the SGW Models

The evolution of the structural parameters of the silica, gel and water regions of the SGW can identify the amount of atomic rearrangement caused by the diffusion of water and silica species through the structure. To differentiate between the silica, gel,

and water regions, changes in the density of silica were used as in Section 5.4.2, for a consistent identification of regions during analysis. Bond angle and bond distance data for the three sections of the model are included in Table 0-6 and Table 0-7.

The structural parameters for the SiO_4 tetrahedra in the silica and gel regions of the model (Si-O, O-O, and Si-Si interatomic distances and O-Si-O and Si-O-Si bond angles) have differences of less than 1% indicating that there is limited distortion of the silica structure. A similar trend is observed for the water molecules with comparable O_w-H_w and H_w-H_w interatomic distances and O_w-H_w-O_w bond angles for molecules in both the gel and the bulk water that are comparable to experimental values (Table 0-6). There is a slight transition in the O_w-H_w-O_w bond angle for the water molecules in both the gel and bulk water regions towards the bulk water value of 164^o, but is consistent with previous computational investigations of the structure of water in increasing cluster size [303]. The O_w-O_w interatomic distances continue to show tendencies toward the formation of structured water due to nanoconfinement effects which is more extreme in the silica gel region with smaller O_w-O_w distances as noted in Section 5.4.1. Overall, the short range structure around silicon and oxygen such as the bond angle and bond distances remain largely unchanged suggesting that the SiO_4 tetrahedra and water molecules do not experience any significant changes in the evolution of the gel structures.

Table 0-6: The silica bond distances and angles in the SGW models, the initial structure, and from experiment. The peak of the BAD or PDF is presented along with the FWHM value in parenthesis.

	Silica					Gel					
	Initial	SGW-1	SGW-2	SGW-3	SGW-4	Initial	SGW-1	SGW-2	SGW-3	SGW-4	Expt.
Si-O dist. (Å)	1.60 (0.10)	1.59 (0.10)	1.59 (0.10)	1.59 (0.11)	1.59 (0.10)	1.58 (0.09)	1.58 (0.09)	1.58 (0.09)	1.58 (0.09)	1.58 (0.09)	1.61[a]
O-O dist. (Å)	2.57 (0.30)	2.57 (0.31)	2.57 (0.30)	2.57 (0.31)	2.57 (0.29)	2.59 (0.25)	2.61 (0.25)	2.61 (0.25)	2.61 (0.26)	2.61 (0.25)	2.65[b]
Si-Si dist. (Å)	3.14 (0.14)	3.14 (0.15)	3.13 (0.15)	3.13 (0.15)	3.13 (0.15)	3.12 (0.13)	3.12 (0.12)	3.12 (0.12)	3.12 (0.11)	3.11 (0.11)	3.1[c]
O-Si-O angle (°)	107 (16)	107 (17)	107 (16)	107 (17)	107 (16)	109 (13)	109 (12)	109 (12)	109 (12)	109 (12)	109.4[b]
Si-O-Si angle (°)	157 (26)	156 (27)	156 (27)	156 (27)	156 (27)	158 (25)	159 (23)	159 (23)	159 (23)	159 (23)	153[b]

[a]Neutron diffraction [39] [b]Electron diffraction [32] [c]Large angle x-ray scattering [295]

Table 0-7: The water bond distances and angles in the SGW models, the initial structure, and from experiment. The peak of the BAD or PDF is presented along with the FWHM value in parenthesis.

	Gel					Water					
	Initial	SGW-1	SGW-2	SGW-3	SGW-4	Initial	SGW-1	SGW-2	SGW-3	SGW-4	Expt.
O_w-H_w dist. (Å)	0.97 (0.07)	0.98 (0.09)	0.97 (0.07)	0.97 (0.06)	0.97 (0.05)	0.98 (0.05)	0.97 (0.07)	0.97 (0.07)	0.97 (0.06)	0.97 (0.06)	0.98[a]
O_w-O_w dist. (Å)	2.84 (0.67)	2.68 (0.25)	2.68 (0.26)	2.68 (0.24)	2.68 (0.27)	2.74 (0.36)	2.80 (0.44)	2.73 (0.51)	2.71 (0.54)	2.70 (0.54)	2.98[b]
H_w-H_w dist. (Å)	1.53 (0.17)	1.53 (0.15)	1.53 (0.14)	1.53 (0.14)	1.52 (0.14)	1.55 (0.11)	1.54 (0.14)	1.53 (0.14)	1.53 (0.14)	1.53 (0.13)	3.1[c]
O_w-H_w-O_w angle (°)	162 (30)	164 (27)	163 (27)	163 (27)	163 (28)	167 (23)	164 (25)	164 (27)	164 (126)	164 (26)	174[d]
H_w-O_w-H_w angle (°)	104 (17)	104 (15)	104 (14)	104 (15)	104 (15)	105 (13)	104 (15)	104 (15)	104 (15)	104 (15)	104.5[a]

[a]Electron diffraction [296] [b]Molecular bean electric resonance spectroscopy [292] [c]Large angle x-ray scattering [295] [d]Molecular beam electric resonance spectroscopy [292]

In addition to the changes in the localized structural features of the silica and water present in the silica, gel and water regions of the model, slightly longer range features such as Q_n distribution and ring size analysis can also provide insight into the amount of reorganization that occurs in the different regions. During the dissolution of silica, it is predicted that the removal of silica from the surface through the formation of a SiO_4H_4 molecule or hydroxylated Q_0 species, follows a series of sequential steps. This starts as a Q_4 species and then transitions to a Q_3, then a Q_2, a Q_1, and, finally, a Q_0, which is suggested through the formation of primarily silica monomers in solution [88,157,158].

Through analysis of the changing Q_4, Q_3, Q_2, Q_1, and Q_0 concentrations, the breaking of siloxane bonds and the formation of silica dissolution products can be identified. The connectivity (C) is also used which describes the average number of bridging oxygens associated with a silicon, with perfect dense silica having a connectivity of four. As the silica structure evolves, the Q_n distribution remains relatively consistent (Figure 0-8.a) with changes in connectivity of less 0.02 from the initial model to the SGW-4 model, which experiences the most structural rearrangement. The slight increases in the Q_1 and Q_2 concentrations are most likely on the interfaces with the conversion of Q_4 and Q_3 species to lower Q_n values.

In the gel region there is significantly more adjustment with an increase in connectivity of 0.26 between the initial structure and SGW-4, a change of 12%. Initially, a decrease in connectivity was expected as the gel evolved since more siloxane bond breakage would result in a lower connectivity and a higher Q_0 concentration. What is identified from the data in Table 0-8 and Figure 0-8.b is that there is a decrease in Q_0

concentration, as the silica monomers diffuse into the water region of the model. Similarly, decreases in Q_1 species indicate that the $Q_1 \rightarrow Q_0$ conversion, which has the lowest activation energy, 12% lower than the $Q_4 \rightarrow Q_3$ or $Q_3 \rightarrow Q_2$ transition, as identified from classical MD simulations by Kagan and Garofalini, results in the creation of additional monomers or dimers that become part of the dissolved silica [88,155]. *Ab initio* computational investigation of the hydrolysis of siloxane bonds with different Q_n species suggested that the $Q_3 \rightarrow Q_2$ transition has the highest activation energy, which may describe why the gel has a decrease in Q_0 and Q_1 species, but increases in Q_2, Q_3, and Q_4, which are more stable [88,155] . As a result it is predicted that as the simulation continues to evolve, the gel structure will increase in connectivity as Q_0 and Q_1 species are removed leaving behind a more interconnected structure. The changing Q_n distribution in silica gel was evaluated by NMR, and found that after 7 days the concentration of Q_2 and Q_3 increases as was seen here on much shorter time frames, and that after 21 days there is a rise in the Q_4 species [56]. Therefore, the formation of crystalline compounds on the surface may be due to the removal of the lower coordination structures, such as Q_1-Q_3 species, allowing for the fully coordinated silicon to condense into crystalline phases.

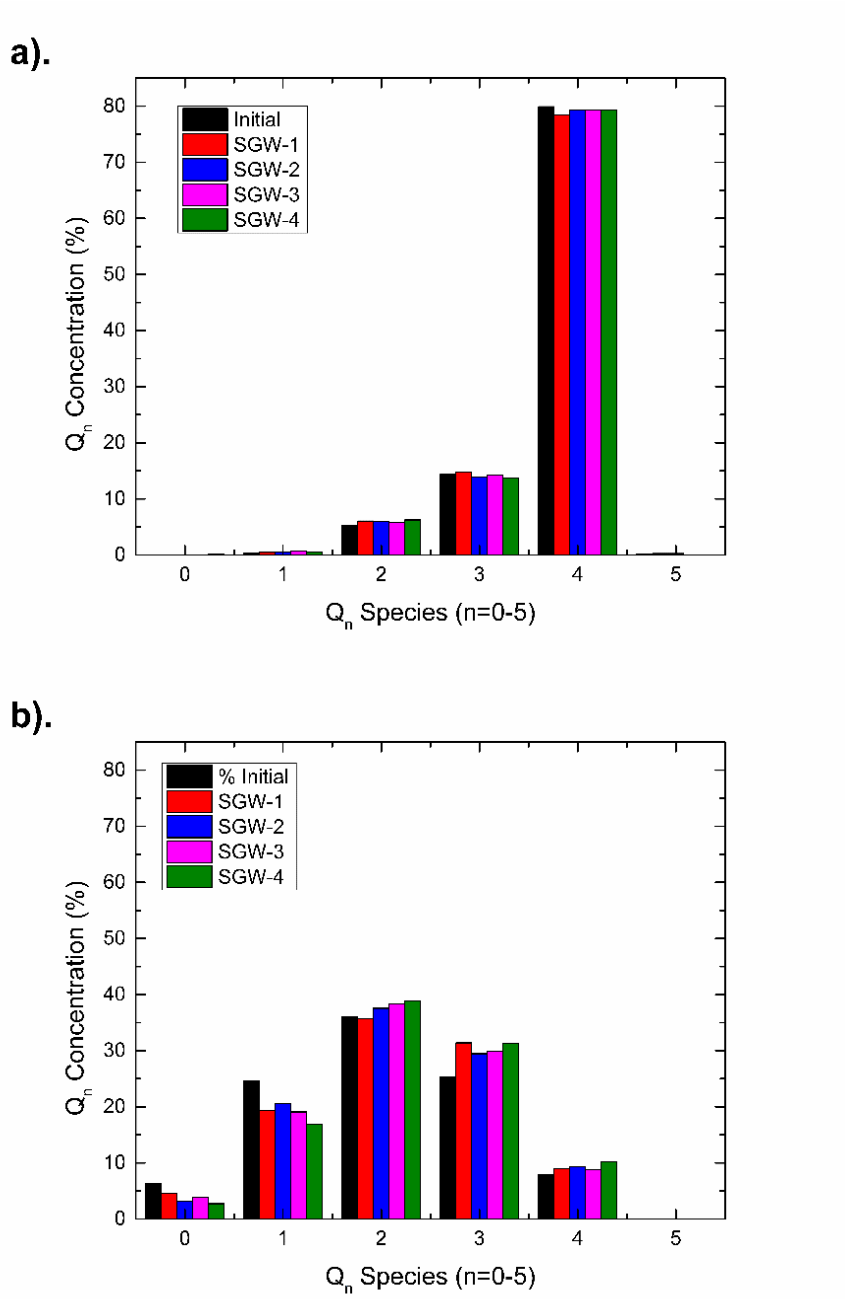

Figure 0-8: Qn distribution of the (a) silica and (b) gel regions of the SGW models.

Table 0-8: Qn distribution and connectivity (C) in the silica and gel regions of the SGW models.

	Silica						Gel					
	Q_1	Q_2	Q_3	Q_4	Q_5	C	Q_0	Q_1	Q_2	Q_3	Q_4	C
Initial	0.33	5.21	14.33	79.91	0.22	3.74	6.27	24.56	36.06	25.26	7.84	2.04
SGW-1	0.47	6.05	14.79	78.46	0.23	3.72	4.57	19.40	35.66	31.38	8.99	2.21
SGW-2	0.59	5.97	13.92	79.30	0.22	3.73	3.11	20.56	37.57	29.44	9.32	2.21
SGW-3	0.71	5.81	14.22	79.27	0.00	3.72	3.82	19.09	38.33	29.96	8.81	2.21
SGW-4	0.59	6.24	13.77	79.29	0.00	3.72	2.71	16.87	38.86	31.33	10.24	2.30

Analysis of the intermediate structure of the silica and gel regions further demonstrates the stability of the silica with a ring size distribution with a maximum of seven that does not appear to have any significant changes during the simulations (Figure 0-9.a). There may be a slight decrease in the six-membered ring concentrations from the initial system compared to the other models that indicates that some restructuring is occurring, though it is low relative to the bulk of the material. This is not the case for the gel region which, as indicated by the changing Q_n distribution, does experience significant alteration of the structure (Figure 0-9.b). In particular, the ring size distribution shows an increase in the five-, six- and seven-membered rings which indicates a reformation of dense silica since pure silica has a peak concentration of six-membered rings [223,235]. This effect increases when more restructuring occurs with higher concentration of five-membered rings from the SGW-4 model compared to early structures (SGW-1, SGW-2, and SGW-3) as well as higher six- and seven-membered rings. This data further suggests that the gel which remains is becoming more similar to the silica in terms of Q_n and ring size distribution as the gel evolves.

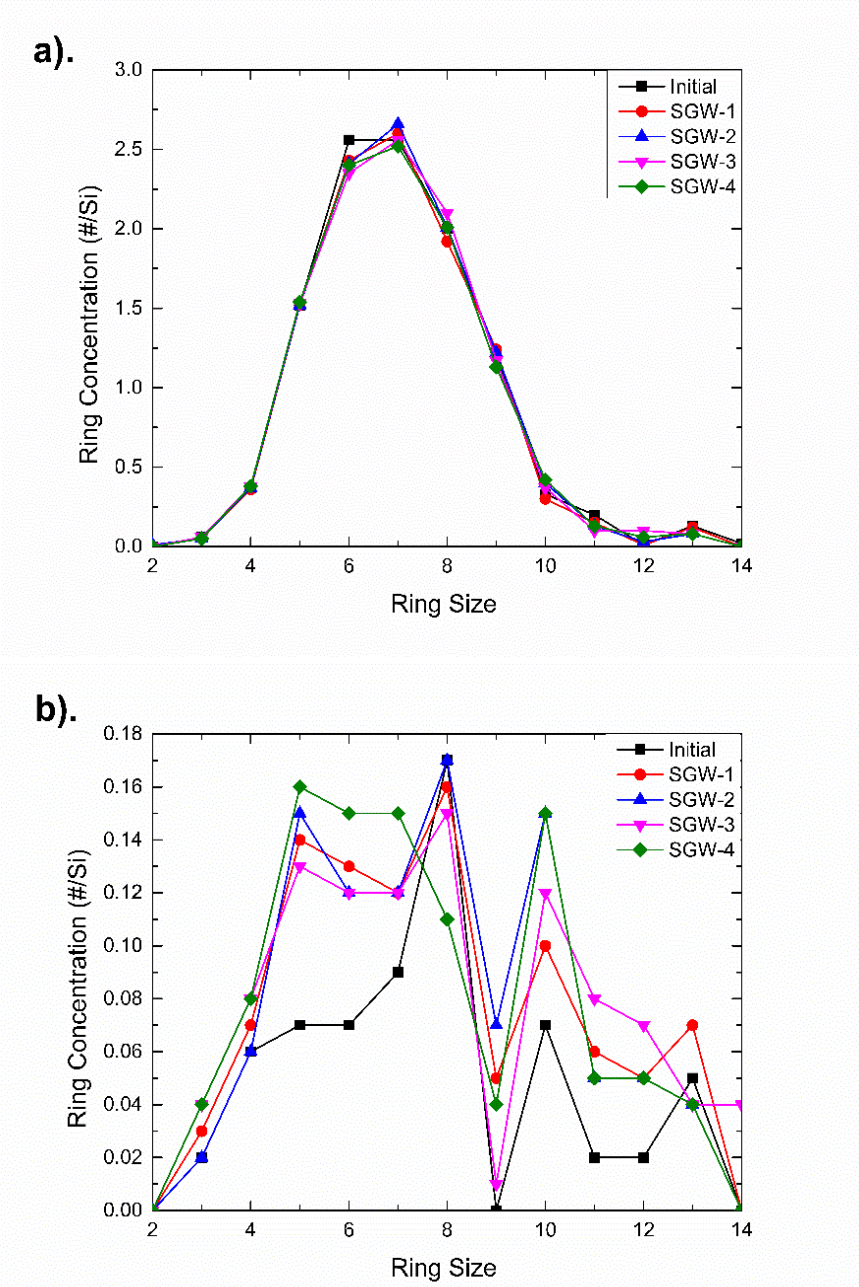

Figure 0-9: Ring size distribution for the (a) silica and (b) gel regions of the SGW models and the initial structure.

5.4.4 Dissolved Silica

An analysis of the changing composition of the water region can provide insight into the dissolution of silica gel and change of the aqueous solution concentration. In

particular, the concentration of silica species in solution is a common method of identifying how fast silicate glasses are dissolving with dilute concentrations of the elements being measured from the bulk solution after the glass sample has been immersed in water for a set amount of time often on the order of days, months, or years [185]. Based on the dimensions of the system studied here, the existence of a single silicon atom in the aqueous region will result in a silica concentration far beyond what would occur in much larger experimental systems. Therefore, analysis of silica concentration in this work only considers the extreme interfacial region of the silica gel. Even so, an analysis of the silica concentration can provide insight into what the equilibrium concentration of silicon is at these system sizes. Previous work on the dissolution of SON68, a thirty component nuclear waste glass, identified final silica concentrations of 50-120ppm (0.05-0.12 g/L) by inductively-coupled plasma mass spectroscopy with the development of supersaturation conditions of 240ppm silicon indicating a decrease in the glass dissolution rate [304,305]. In the study of sodium borosilicate glasses dissolution, it was reported that a stable silica concentration of 600-700ppm (0.6-0.7g/L), much higher than what is reported for more complex multicomponent glass [304,305], was observed [184]. Other experimental investigation of pure silica indicate that at 300K the maximum silica solubility or the solubility limit of silica in water is ~1500ppm (1.5g/L) for amorphous silica while quartz having half of that value [278].

In this work, the amount of dissolved silica is ~5 g/L for the SGW-1 model and then increases to ~40g/L for SGW-4 (Table 0-9). The level of dissolved silica is one to two orders of magnitude higher than what would be expected, but the initial rapid

increase in silica concentration (in the SGW-1 model) followed by a slower increase for the models equilibrated at higher temperatures. It is worth noting that high concentrations of soluble species have been identified in naturally occurring systems, such as sulfate concentrations of ~760g/L in acidic mine waters at the Richmond Mine in California [306] and that artificially high ion concentrations occur adjacent to surfaces during pitting and crevice corrosion [307]. The high concentration of silica in solution is the result of limited bulk water to allow for further movement of dissolved silica away from the surface resulting in a peak silica concentration adjacent to the gel-water interface. Experimental investigations by Zotov and Keppler used Raman spectroscopy to identify monomeric silica (SiO_4H_4) as the primary form of silica in solution at low temperature, and noted that at higher temperatures (greater than 900K) more complex polymeric species were present [157,158]. Monomeric silica is also noted to be the most common form of dissolved silica in solution after the dissolution of multicomponent glass while AIMD studies suggested that both monomers, dimers, and trimers are stable at temperatures as high as 900K [185,246]. Evaluation of the stability of silica monomers, dimers, and trimers in the gas phase by high level of computational theory, MP2, indicates the formation of a dimer is favorable in the gas phase and only slightly less favorable when hydrated, an effect which decreases with increasing temperature and pressure [282]. The polymerization of highly oversaturated water-silica mixture (composed entirely of monomers) was studied using classical MD methods, and the spontaneous polymerization of silica with the formation of dimers, followed by a linear trimers, and continuing on in the formation of a network structures were reported [246].

In the water region of the SGW model, the identification of the structure of the dissolved species is complicated by the increasingly diffuse nature of the water-gel interface. Therefore, silica species that have diffused greater than 3Å away from the surface are considered to have been completely transferred into the water region of the structure. The silica concentration is evaluated in 2Å thick sections of the water region as defined in Section 5.4.2. Due to the wide range of silica concentrations in the water region, data is reported using standard error included in Eq. 0-1 with SE as the standard error, SD as the standard deviation, and n as the number of observations/iterations.

$$SE = \frac{SD}{\sqrt{n}} \qquad \text{Eq. 0-1}$$

Throughout the SGW models, a number of silica species form including monomers, dimers, trimers, as well as longer silica chains, containing up to eleven silicon. All are fully hydroxylated, and the majority of the molecules are monomers, making up 50%, 53%, 86%, and 77% of the dissolved silica in the SGW-1, SGW-2, SGW-3, and SGW-4 models respectively (Figure 0-10.a.). Overall 84%+ of the silica clusters in the water region are either monomers or dimers with the balance being composed of longer chain structures. The concentration of large polymerized silica clusters may be the result of the small model size that develops oversaturation conditions that stabilize silica chains. Additionally, some of the silica appears to be dissolved and diffuse into the water region in larger silicon clusters or chunks with weaker Q_1 and Q_2 linkages breaking allowing for higher coordination of the dissolved silica. At 300K the silica chains are expected to be unstable, and they can either re-polymerize on the silica surface or break up to form smaller clusters or monomers, which diffuse through the solution faster than large molecules [246].

If only the monomeric silica is considered since experimentally all the stable silica in water is reported to be SiO_4H_4 the concentration of silica increases from 3.47 g/L in SWG-1 up to 11.90g/L in SGW-4 and plateaus suggesting saturation conditions. This is in contrast with much higher concentration of dissolved silica when larger clusters are considered. (Figure 0-10.b). Despite the high silica concentration levels, the trend is consistent with experiment, an initial high development of dissolved silica species, followed by a tapering off of silica concentration once a saturation condition is reached. The stabilizing of dissolved monomer concentration suggests that the model is approaching an equilibrium with a balance between dissolving and re-polymerizing silica species occurring at the gel-water interface though further analysis of the structure for more evolved SGW models will need to be performed to confirm this assertion.

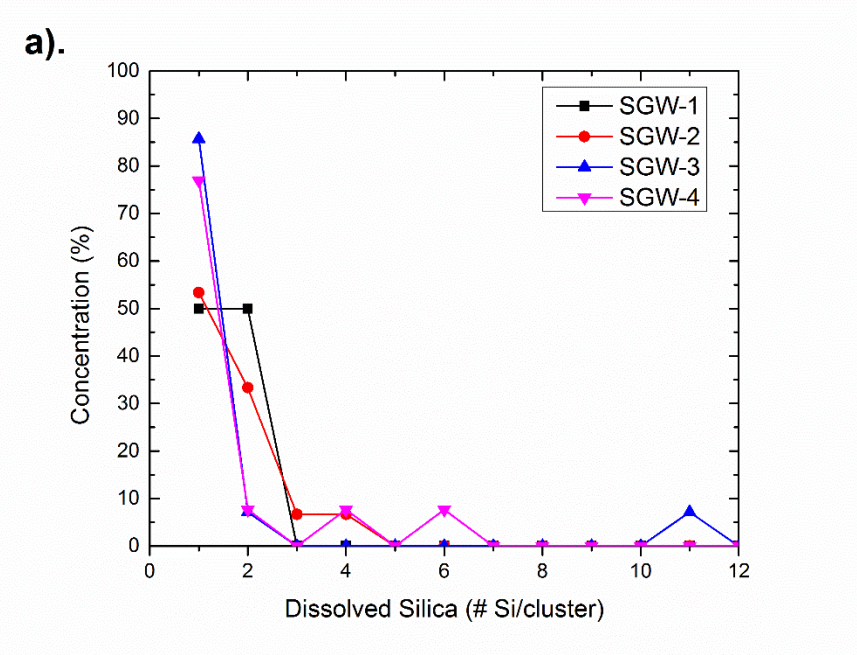

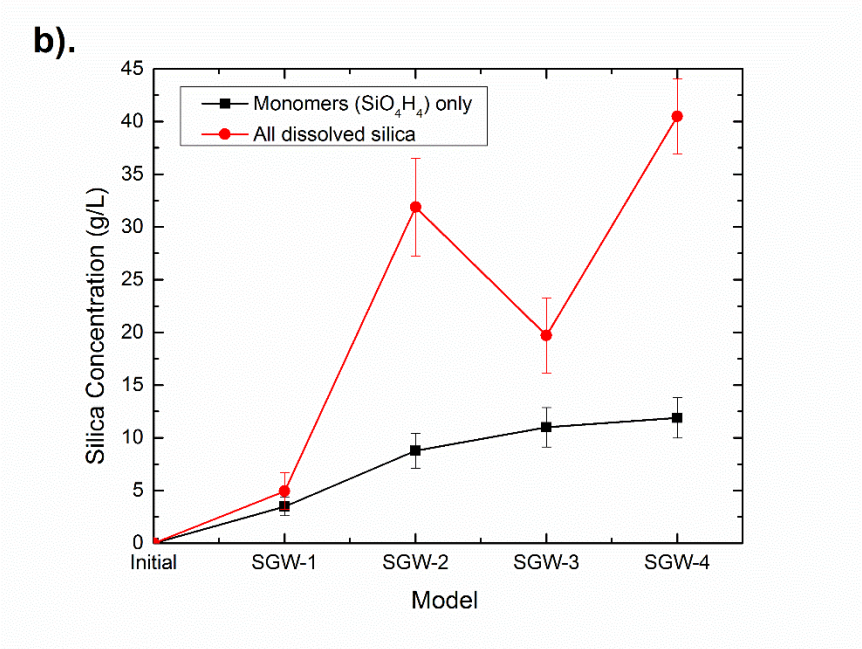

Figure 0-10: (a) Dissolved silica concentration in the SGW models as either monomers or larger silica polymer chains, and (b) distribution of dissolved silica molecules by the number of silicon atoms in a cluster. Error bars are the standard error.

Table 0-9: Silica concentration in either the water region (g/L) and in the gel, silica, and interface regions (g/cm^3). The variation is the standard error.

	Water Region: All Si	Water Region: Monomers	Water-Gel Interface	Gel Region	Gel-Silica Interface	Silica Region
Units	(g/L)	(g/L)	(g/cm^3)	(g/cm^3)	(g/cm^3)	(g/cm^3)
Initial	0.00±0.00	0.00±0.00	0.34±0.14	1.21±0.03	1.65±0.17	2.02±0.03
SGW-1	4.94±1.73	3.47±0.87	0.69±0.15	1.06±0.02	1.71±0.18	2.10±0.02
SGW-2	31.89±4.65	8.77±1.65	0.60±0.60	0.97±0.02	1.70±0.19	2.10±0.01
SGW-3	19.71±3.57	11.00±1.87	0.57±0.09	0.84±0.03	1.62±0.22	2.05±0.04
SGW-4	40.49±4.44	11.90±1.93	0.78±0.10	0.88±0.02	1.62±0.20	2.06±0.04

There is also silica enrichment of the water-gel interface with the amount of silica in that region doubling through the simulations from 0.35 g/cm^3 to 0.78 g/cm^3 compared to a similar decrease in the silica concentration in the gel transitioning from 1.21 g/cm^3 in the initial structure to 0.88 g/cm^3 in the SWG-4 model. Comparatively, the silica concentration in the gel-silica interface and the silica region remained constant at ~1.65 g/cm^3 and ~2.05 g/cm^3 in the equilibration steps. Therefore, the majority of the movement of silica is transferring from the gel to the water region with almost no silicon transferring from the silica to the gel region. Overall, the water-gel interfacial region and the gel are responsible for the development of silica saturation conditions, and that further re-structuring of the surface including re-polymerization of silica onto the gel surface may be occurring once the system reaches equilibrium conditions.

5.5 Conclusions

Classical MD simulations with the Reactive Force Field (ReaxFF) potential were used to create three-component glass dissolution models consisting of silica, gel and water regions (SGW), as well as two important interfaces: the water-gel and the gel-silica.

Due to the limited information in the literature concerning the structure of silica gels, an analysis of the silica gel systems was performed first before the development of the SGW models. Two different methods of creating silica gel structures were used, one of which is the remnant of a multicomponent glass (RSG) and the other uses a dense silica basis from which silicon atoms are randomly removed resulting in a de-polymerization of the structure (DSG). The results indicate that the RSG models are

best represented by a silica gel structure which has had 40% of the original silicon removed (DSG-40), resulting in a fragmented nanoporous silica which, when hydrated, has comparable Q_n and ring size distribution, as well as localized features such as interatomic distances and bond angels. The DSG-40 gel model was used as an interfacial layer between the dense silica and bulk water in the SGW models.

The development of the SGW model included the formation of the gel structure in contact with both water and dense silica, ensuring a defect free interface between the silica and the silica gel structures. The SGW models was allowed to evolve at 300K, 500K, 700K, and 900K for 1 ns to simulate the progression the gel layer. The results indicate that there is a growth of the gel region into the water resulting in dissolution of silica into the water from the gel while the dense silica remains intact at these temperatures. Limited changes in the bond angels and interatomic distance in both the water and the silica were observed in the silica, gel, and water regions indicating that though the silica concentration is changing and the water-gel interface advances into the water, the local structure of the water and silica are unchanged. It is worth noting that the average H-O..H bond angle that measures the hydrogen bonding network of water in the gel region is about 11 degrees smaller than bulk water suggesting water molecules confined in the nanopores in the gel regions have slightly different structure (and reactivity) than those in the bulk water.

The Q_n and ring size distribution of the gel were analyzed, and the results suggest that the evolution of the structure results in a gel with a silica backbone more consistent with dense silica. This indicates that the most defective sites in the gel, such as Q_1 and Q_2 species, are removed resulting in an enrichment of the Q_3 and Q_4. This trend

towards network silica may be indicative of a tendency of the gel to form more ordered and stable phases rather than the initial highly fragmented structure [269]. Similar trends were observed in the ring size distribution with the formation of five-, six-, and seven-membered rings as the gel evolves which are more consistent with silica with a peak in the ring size distribution at six-membered rings [235].

During the course of the simulations, the water regions experience an enrichment in silica concentration due to both individual silica monomers and chunks of silica breaking from the gel surface and diffusing into the water. Of the dissolved species, the majority (50%+) are monomers, and their concentration increasing to over 70% for more evolved systems. If the monomer concentration only is used to calculate the silica concentration in water values vary from 4g/L to 12 g/L, 3-8x the experimental values for pure silica dissolution of ~1.5g/L [278]. This value is about two orders of magnitude higher than experimental solubility limit of silica in water. This is due to the region modeled is very close to the surface where high concentration of silica is possible while it will be diluted in the bulk water lowering silica concentration in experimental measurements. The silica concentration experiences an initial rapid increase before stabilizing at ~12g/L suggesting that the model has fully relaxed and reached a saturation condition for silica in aqueous solutions.

The atomistic model of the gel structure and associated interfaces generated in this work provides structural details and properties of these complex systems that help the understanding of the key steps controlling the dissolution, especially the residual rate behaviors, of silicate glasses.

CHAPTER 6 CONCLUSIONS AND FUTURE WORK

6.1 Conclusions

In this dissertation, classical molecular dynamics (MD) and density functional theory (DFT) atomistic simulation methods were used to investigate the water-silica surface and the reaction mechanisms and processes which are responsible for silica dissolution in water. Highly accurate DFT methods were used to analyze the details of water interactions with the complex internal porosity in nanoporous silica structures, followed by a validation of a dissociative classical MD water-silica potential that was used in the simulation of multicomponent silica dissolution models for analysis of the silica-gel and gel-water interfaces.

The study of water reactions with the unhydroxylated internal surfaces of nanoporous silica systems was performed using DFT *ab initio* MD (AIMD) simulations that ensures an accurate description of bond breakage and formation. The fast termination of coordination defects resulting in the creation of silanol (Si-OH) groups was identified as was the stability of strained two-membered and three-membered rings during the course of the 30ps simulations. Limited two-membered ring removal was predicted to be the result of slow water diffusion through the confined regions of the nanoporous silica structures as well as changes in the energy barriers due to the location of Si-O bonds on the surface. The mechanism for strained Si-O bond removal includes the formation of five-membered silicon through hydrogen bonding of a water molecule to the silicon resulting in the breakage of the Si-O bond.

Using the information on the reaction rates and mechanisms between water and nanoporous silica systems from AIMD simulations, two dissociative classical MD

potentials in the framework of Reactive Force Field (ReaxFF) were used to simulate the water-silica system. The more computationally expensive AIMD simulations provide validations of the ReaxFF results that show that they are capable of identifying the features of water interactions with complex internal silica surfaces. Overall, the ReaxFF potential parametrized by Yeon and van Duin [98] was found to accurately simulate the structural features of both water and silica, improved activation energies for strained siloxane bond removal compared to earlier forcefields [85]; similar hydroxylation rates, and the removal of three-bonded oxygen defects. Variation in the siloxane bond breakage mechanism occurred with DFT simulations resulting in the formation of overcoordinated silicon as intermediate defects compared to the absorption of hydrogen onto the bridging oxygen in the ReaxFF simulations possibly due to use of water interaction with silica dimers for the parametrization of the classical MD potential. The structure of the two-membered ring surface defects that include strained Si-O bonds, was less symmetric than in the DFT simulations which may affect their reactivity, and was noted for future studies.

The validated classical MD potential ReaxFF was used to investigate the more complex structure of silica gels and their interfaces in individual systems and as part of three-component glass dissolutions models consisting of silica, gel, and water (SGW) regions. Silica gel structure models were created from two different methods, one which is the silica remnant of a multicomponent glass systems after dissolution as is suggested to occur in nuclear waste glasses, and the other which approximates this process for pure silica glasses through the removal of individual SiO_4 tetrahedra from dense amorphous silica structures. A silica gel which best approximates the silica

remnant structure was used as an intermediate phase in the development of the silica dissolution model. These are the first atomistic structure models that we are aware of which includes the existence of a silica gel layer between dense silica and bulk water to investigate the effect of intermediate phases in dissolution.

Through high temperature simulation of the SGW model, the structures were allowed to evolve resulting in the growth of the silica gel into the water region while other interfaces remained stable indicating the reactivity of the gel-water interface. Localized structural features of the silica gel remain unchanged with comparable interatomic distances and bond angels in the SiO_4 units and water molecules in the dense silica, silica gel, and bulk water regions. Intermediate features, such as bridging oxygen concentration and ring size distributions, identified that the gel becomes similar to dense silica as the system evolves through the removal of reactive silicon. This results in increases in the concentration of five-membered and six-membered rings as well as fully bonded silica tetrahedra. Dissolution of the surface is indicated by increasing silica content in the water region with dissolved silica species primarily composed of hydroxylated monomers (SiO_4H4) as in experimental systems.

Overall, the work in this dissertations focuses on application of multiple classical and first principles atomistic simulation methods to investigate the structure and reactivity of complex water-nanoporous silica systems. Insights of the key processes of water interactions with internal pore surfaces and silica-gel and gel-water interfaces which is critical in developing a complete understanding of the reaction mechanisms and kinetics which govern silica dissolution were obtained from the detailed atomistic models. The development of silica gel structures which mimic the interfacial layers

formed during silica interaction with water, and the role of secondary phases between dense silica and bulk water on the dissolution process was also investigated, and these new models add to the knowledge of the fundamental processes of water-silica interactions and the dissolution of glasses.

6.2 Future Work

Based on the work completed in this dissertation, several other avenues of investigation have been identified to provide insight into water interactions with silica within a similar simulation framework used this dissertation, and are worthy of future investigation.

1. While the changing stability of strained siloxane bonds in nanoporous silica has been suggested as the result of their location on concave surfaces, a systematic study of this effect would be valuable in quantifying the role of the changing silica surface microstructure on siloxane bond reactivity.
2. Through validation of the ReaxFF potentials, several differences were noted in the DFT and classical MD results. Through collaboration with the developer of the force field, it is possible to provide DFT data for the potential parameterization to remove some of the inconsistencies either in the water-silica version or in other multicomponent silicate based systems.
3. While silica gels were created for pure silica systems, experimental analysis of gel structures formed during the dissolution of multicomponent glasses noted that aluminum is also stable in the gel, and the structural effects aluminum should be examined on the evolution of the silica rich gel.

4. Changing diffusion rates of water in the gel and bulk regions of the SGW will provide information on the passivating effect of the gel that is predicted to occur due to the limited water diffusion through the structure.
5. The structure of the interfaces, such as the formation of additional coordination or ring defects at the silica-gel and gel-water interfaces, would provide insight into the growth mechanisms of the gel.
6. Varying porosities of the silica gel can also be investigated since the silica content of the gel changes over time in experimental systems and may indicate a ripening of the gel and effect of kinetics of development of crystalline phases.
7. The role of dissolved silica on the growth of the gel-water interface, such as the possibility of polymerization reactions occurring in the water and then reattachment of the silica to the gel surface, can provide information on the existence of surface nucleation sites, and the development of crystalline phases on the surface.

APPENDIX A

LIST OF PUBLICATIONS

My PhD work yielded the following journal publications:

1. Rimsza, J. M., and Jincheng Du. "Structural and mechanical properties of nanoporous silica." Journal of the American Ceramic Society 97.3 (2014): 772-781
2. Rimsza, J. M., J. A. Kelber, and Jincheng Du. "Mechanisms of oxygen plasma damage of amine and methyl terminated organosilicate low-k dielectrics from ab initio molecular dynamics simulations." Journal of Physics D: Applied Physics 47.33 (2014): 335204.
3. Kazi, Haseeb, et al. "Ar ions and oxygen plasma interactions of amine terminated organosilicate glass: A combined experimental and ab initio simulations study." Journal of Vacuum Science & Technology A 32.5 (2014): 051301.
4. Rimsza, J. M., and Jincheng Du. "Surface reactions and structural evolution of organosilicate glass under Ar plasma bombardment." Computational Materials Science 110 (2015): 287-294.
5. Rimsza, J. M., and Jincheng Du. "Ab initio Molecular Dynamics Simulations of the Hydroxylation of Nanoporous Silica." Journal of the American Ceramic Society 98.12 (2015): 3748-3757.
6. Rimsza, J. M., et al. "Chemical bonding in carborane/aromatic co-polymers: a first-principles analysis of experimental photoemission spectra." Molecular Simulation 42.1 (2016): 39-46.
7. Rimsza, J. M., Lu Deng, and Jincheng Du. "Molecular dynamics simulations of nanoporous organosilicate glasses using Reactive Force Field (ReaxFF)." Journal of Non-Crystalline Solids 431 (2016): 103-111.
8. Kazi, H., et al. "Organosilicate glass dielectric films with backbone carbon: Enhanced resistance to carbon loss in plasma environments." Interconnect Technology Conference/Advanced Metallization Conference (IITC/AMC), 2014 IEEE International. IEEE, 2014.

REFERENCES

[1] N.I. Christensen, W.D. Mooney, Seismic velocity structure and composition of the continental crust: A global view, Journal of Geophysical Research: Solid Earth. 100 (1995) 9761-9788.

[2] I.A. Shiklomanov, Appraisal and assessment of world water resources, Water Int. 25 (2000) 11-32.

[3] S.L. Brantley, J.D. Kubicki, A.F. White, Kinetics of Water-Rock Interaction, Springer, 2008.

[4] E. Watson, D. Wark, Diffusion of dissolved SiO2 in H2O at 1 GPa, with implications for mass transport in the crust and upper mantle, Contributions to Mineralogy and Petrology. 130 (1997) 66-80.

[5] D. Griggs, Hydrolytic Weakening of Quartz and Other Silicates*, Geophysical Journal of the Royal Astronomical Society. 14 (1967) 19-31.

[6] J. Shoeb, M.J. Kushner, Damage by radicals and photons during plasma cleaning of porous low-k SiOCH. II. Water uptake and change in dielectric constant, Journal of Vacuum Science & Technology A: Vacuum, Surfaces, and Films. 30 (2012) 041304-041304-8.

[7] M.W. Lane, J.M. Snodgrass, R.H. Dauskardt, Environmental effects on interfacial adhesion, Microelectronics Reliability. 41 (2001) 1615-1624.

[8] S. Wagner, K. Hoeppner, M. Toepper, O. Wittler, K. Lang, A critical review of corrosion phenomena in microelectronic systems, (2014) 1-7.

[9] Y. Gu, C. Ogawa, J. Kobayashi, Y. Mori, S. Kobayashi, A Heterogeneous Silica-Supported Scandium/Ionic Liquid Catalyst System for Organic Reactions in Water, Angewandte Chemie. 118 (2006) 7375-7378.

[10] L.J. Alemany, M.A. Ban, E. Pardo, F. Martin, M. Galan-Fereres, J. Blasco, Photodegradation of phenol in water using silica-supported titania catalysts, Applied Catalysis B: Environmental. 13 (1997) 289-297.

[11] R. Davda, J. Shabaker, G. Huber, R. Cortright, J.A. Dumesic, Aqueous-phase reforming of ethylene glycol on silica-supported metal catalysts, Applied Catalysis B: Environmental. 43 (2003) 13-26.

[12] M. Nijkamp, J. Raaymakers, A. Van Dillen, K. De Jong, Hydrogen storage using physisorption–materials demands, Applied Physics A. 72 (2001) 619-623.

[13] Y. Li, R.T. Yang, Hydrogen storage in low silica type X zeolites, The Journal of Physical Chemistry B. 110 (2006) 17175-17181.

[14] S. Zheng, F. Fang, G. Zhou, G. Chen, L. Ouyang, M. Zhu, D. Sun, Hydrogen storage properties of space-confined NaAlH4 nanoparticles in ordered mesoporous silica, Chemistry of Materials. 20 (2008) 3954-3958.

[15] H. Yang, Z. Xu, M. Fan, R. Gupta, R.B. Slimane, A.E. Bland, I. Wright, Progress in carbon dioxide separation and capture: A review, Journal of Environmental Sciences. 20 (2008) 14-27.

[16] D.M. D'Alessandro, B. Smit, J.R. Long, Carbon dioxide capture: prospects for new materials, Angewandte Chemie International Edition. 49 (2010) 6058-6082.

[17] S. Kim, J. Ida, V.V. Guliants, Y. Lin, Tailoring pore properties of MCM-48 silica for selective adsorption of CO2, The Journal of Physical Chemistry B. 109 (2005) 6287-6293.

[18] C. Wang, C. Wu, Electrical sensing properties of silica aerogel thin films to humidity, Thin Solid Films. 496 (2006) 658-664.

[19] L.L. Hench, J.R. Jones, P. Sepulveda, Bioactive materials for tissue engineering scaffolds, Tissue Engineering: World Scientific Pub.Co Inc. (2002) 3-24.

[20] E. Jéquier, F. Constant, Water as an essential nutrient: the physiological basis of hydration, Eur. J. Clin. Nutr. 64 (2010) 115-123.

[21] L.L. Hench, The story of Bioglass®, J. Mater. Sci. Mater. Med. 17 (2006) 967-978.

[22] A. Hoppe, N.S. Güldal, A.R. Boccaccini, A review of the biological response to ionic dissolution products from bioactive glasses and glass-ceramics, Biomaterials. 32 (2011) 2757-2774.

[23] M.I. Ojovan, W.E. Lee, Glassy wasteforms for nuclear waste immobilization, Metallurgical and Materials Transactions A. 42 (2011) 837-851.

[24] C. Poinssot, S. Gin, Long-term Behavior Science: The cornerstone approach for reliably assessing the long-term performance of nuclear waste, J. Nucl. Mater. 420 (2012) 182-192.

[25] W. Lee, M. Ojovan, M. Stennett, N. Hyatt, Immobilisation of radioactive waste in glasses, glass composite materials and ceramics, Advances in Applied Ceramics. 105 (2006) 3-12.

[26] S. Gin, A. Abdelouas, L.J. Criscenti, W.L. Ebert, K. Ferrand, T. Geisler, M.T. Harrison, Y. Inagaki, S. Mitsui, K.T. Mueller, An international initiative on long-term behavior of high-level nuclear waste glass, Materials Today. 16 (2013) 243-248.

[27] K.B. Krauskopf, Dissolution and precipitation of silica at low temperatures, Geochim. Cosmochim. Acta. 10 (1956) 1-26.

[28] X.G. Zhang, Electrochemistry of Silicon and its Oxide, Springer, 2001.

[29] A.C. Lasaga, Kinetic Theory in the Earth Sciences, Princeton University Press, 2014.

[30] E.F. Vansant, P. Van Der Voort, K.C. Vrancken, Characterization and Chemical Modification of the Silica Surface, Elsevier, 1995.

[31] A.H. Church, XXII.—Observations on silica, Journal of the Chemical Society. 15 (1862) 107-110.

[32] R. Mozzi, B. Warren, The structure of vitreous silica, Journal of Applied Crystallography. 2 (1969) 164-172.

[33] M. Affatigato, Modern Glass Characterization, John Wiley & Sons, 2015.

[34] E. Lorch, Neutron diffraction by germania, silica and radiation-damaged silica glasses, Journal of Physics C: Solid State Physics. 2 (1969) 229.

[35] L. Börjesson, L. Torell, U. Dahlborg, W. Howells, Evidence of anomalous intermediate-range ordering in superionic borate glasses from neutron diffraction, Physical Review B. 39 (1989) 3404.

[36] J. Swenson, L. Börjesson, W. Howells, Structure of borate glasses from neutron-diffraction experiments, Physical Review B. 52 (1995) 9310.

[37] M. Tachez, R. Mercier, J. Malugani, P. Chieux, Structure determination of AgPO 3 and (AgPO 3) 0.5 (AgI) 0.5 glasses by neutron diffraction and small angle neutron scattering, Solid State Ionics. 25 (1987) 263-270.

[38] A.C. Wright, Neutron scattering from vitreous silica. V. The structure of vitreous silica: What have we learned from 60 years of diffraction studies? J. Non Cryst. Solids. 179 (1994) 84-115.

[39] A.C. Wright, Diffraction studies of glass structure, J. Non Cryst. Solids. 123 (1990) 129-148.

[40] C. Meade, R.J. Hemley, H. Mao, High-pressure X-ray diffraction of SiO 2 glass, Phys. Rev. Lett. 69 (1992) 1387.

[41] E. Matsubara, Y. Waseda, M. Ashizuka, E. Ishida, Structural study of binary phosphate glasses with MgO, ZnO, and CaO by X-ray diffraction, J. Non Cryst. Solids. 103 (1988) 117-124.

[42] M. Okuno, N. Zotov, M. Schmücker, H. Schneider, Structure of SiO 2–Al 2 O 3 glasses: combined X-ray diffraction, IR and Raman studies, J. Non Cryst. Solids. 351 (2005) 1032-1038.

[43] S.C. Ringwald, J.E. Pemberton, Adsorption interactions of aromatics and heteroaromatics with hydrated and dehydrated silica surfaces by Raman and FTIR spectroscopies, Environ. Sci. Technol. 34 (2000) 259-265.

[44] J.R. Bailey, M.M. McGuire, ATR-FTIR observations of water structure in colloidal silica: Implications for the hydration force mechanism, Langmuir. 23 (2007) 10995-10999.

[45] J. Żeglin, G.P. Piotrowski, R. Piękos, A study of interaction between hydrogen peroxide and silica gel by FTIR spectroscopy and quantum chemistry, J. Mol. Struct. 794 (2006) 83-91.

[46] V. Crupi, F. Longo, D. Majolino, V. Venuti, Raman spectroscopy: probing dynamics of water molecules confined in nanoporous silica glasses, The European Physical Journal Special Topics. 141 (2007) 61-64.

[47] P. Innocenzi, Infrared spectroscopy of sol–gel derived silica-based films: a spectra-microstructure overview, J. Non Cryst. Solids. 316 (2003) 309-319.

[48] H. Wakabayashi, M. Tomozawa, Diffusion of water into silica glass at low temperature, J Am Ceram Soc. 72 (1989) 1850-1855.

[49] K. Davis, M. Tomozawa, An infrared spectroscopic study of water-related species in silica glasses, J. Non Cryst. Solids. 201 (1996) 177-198.

[50] N. Yanagisawa, K. Fujimoto, S. Nakashima, Y. Kurata, N. Sanada, Micro FT-IR study of the hydration-layer during dissolution of silica glass, Geochim. Cosmochim. Acta. 61 (1997) 1165-1170.

[51] R. Stolen, G. Walrafen, Water and its relation to broken bond defects in fused silica, J. Chem. Phys. 64 (1976) 2623-2631.

[52] A. Bertoluzza, C. Fagnano, M.A. Morelli, V. Gottardi, M. Guglielmi, Raman and infrared spectra on silica gel evolving toward glass, J. Non Cryst. Solids. 48 (1982) 117-128.

[53] A. Anedda, C.M. Carbonaro, F. Clemente, R. Corpino, P.C. Ricci, Raman investigation of surface OH-species in porous silica, The Journal of Physical Chemistry B. 107 (2003) 13661-13664.

[54] M. Dračínský, L. Benda, P. Bouř, Ab initio modeling of fused silica, crystal quartz, and water Raman spectra, Chemical Physics Letters. 512 (2011) 54-59.

[55] B. Morrow, A. McFarlan, Surface vibrational modes of silanol groups on silica, J. Phys. Chem. 96 (1992) 1395-1400.

[56] B. Gouze, J. Cambedouzou, S. Parrès-Maynadié, D. Rébiscoul, How hexagonal mesoporous silica evolves in water on short and long term: Role of pore size and silica wall porosity, Microporous and Mesoporous Materials. 183 (2014) 168-176.

[57] N. Baccile, G. Laurent, C. Bonhomme, P. Innocenzi, F. Babonneau, Solid-state NMR characterization of the surfactant-silica interface in templated silicas: acidic versus basic conditions, Chemistry of materials. 19 (2007) 1343-1354.

[58] A. Pajzderska, P. Bilski, J. Wąsicki, Phase diagram of water confined in MCM-41 up to 700 MPa, J. Chem. Phys. 142 (2015) 084505.

[59] P. Bonnaud, B. Coasne, R.J. Pellenq, Molecular simulation of water confined in nanoporous silica, Journal of Physics: Condensed Matter. 22 (2010) 284110.

[60] D.R. Kinney, I.S. Chuang, G.E. Maciel, Water and the silica surface as studied by variable-temperature high-resolution proton NMR, J. Am. Chem. Soc. 115 (1993) 6786-6794.

[61] P. Gallo, M. Rovere, E. Spohr, Glass transition and layering effects in confined water: a computer simulation study, J. Chem. Phys. 113 (2000) 11324-11335.

[62] H.N. Kim, S.K. Lee, Atomic structure and dehydration mechanism of amorphous silica: Insights from 29 Si and 1 H solid-state MAS NMR study of SiO 2 nanoparticles, Geochim. Cosmochim. Acta. 120 (2013) 39-64.

[63] C.E. Bronnimann, R.C. Zeigler, G.E. Maciel, Proton NMR study of dehydration of the silica gel surface, J. Am. Chem. Soc. 110 (1988) 2023-2026.

[64] F. Mauri, A. Pasquarello, B.G. Pfrommer, Y.G. Yoon, S.G. Louie, Si-O-Si bond-angle distribution in vitreous silica from first-principles^{29} Si NMR analysis, Physical Review B. 62 (2000) 4786-4789.

[65] T. Charpentier, P. Kroll, F. Mauri, First-principles nuclear magnetic resonance structural analysis of vitreous silica, The Journal of Physical Chemistry C. 113 (2009) 7917-7929.

[66] C. Oberdorfer, P. Stender, C. Reinke, G. Schmitz, Laser-assisted atom probe tomography of oxide materials, Microscopy and microanalysis. 13 (2007) 342-346.

[67] T. Ohkubo, Y.M. Chen, M. Kodzuka, F. Li, K. Oh-ishi, K. Hono, Laser-assisted atom probe analysis of bulk insulating ceramics, 1231 (2009) 1231-NN02-09.

[68] G. Greiwe, Z. Balogh, G. Schmitz, Atom probe tomography of lithium-doped network glasses, Ultramicroscopy. 141 (2014) 51-55.

[69] E.A. Marquis, M. Bachhav, Y. Chen, Y. Dong, L.M. Gordon, A. McFarland, On the current role of atom probe tomography in materials characterization and materials science, Current Opinion in Solid State and Materials Science. 17 (2013) 217-223.

[70] D. Santhanagopalan, D.K. Schreiber, D.E. Perea, R.L. Martens, Y. Janssen, P. Khalifah, Y.S. Meng, Effects of laser energy and wavelength on the analysis of LiFePO 4 using laser assisted atom probe tomography, Ultramicroscopy. 148 (2015) 57-66.

[71] R. Hellmann, S. Cotte, E. Cadel, S. Malladi, L.S. Karlsson, S. Lozano-Perez, M. Cabié, A. Seyeux, Nanometre-scale evidence for interfacial dissolution–reprecipitation control of silicate glass corrosion, Nature materials. 14 (2015) 307-311.

[72] S. Gin, J.V. Ryan, D.K. Schreiber, J. Neeway, M. Cabié, Contribution of atom-probe tomography to a better understanding of glass alteration mechanisms: Application to a nuclear glass specimen altered 25years in a granitic environment, Chem. Geol. 349 (2013) 99-109.

[73] P.L. Silvestrelli, M. Parrinello, Structural, electronic, and bonding properties of liquid water from first principles, J. Chem. Phys. 111 (1999) 3572-3580.

[74] D. Laage, J.T. Hynes, A molecular jump mechanism of water reorientation, Science. 311 (2006) 832-835.

[75] M. Tuckerman, K. Laasonen, M. Sprik, M. Parrinello, Abinitio molecular dynamics simulation of the solvation and transport of hydronium and hydroxyl ions in water, J. Chem. Phys. 103 (1995) 150-161.

[76] E. Schwegler, J.C. Grossman, F. Gygi, G. Galli, Towards an assessment of the accuracy of density functional theory for first principles simulations of water. II, J. Chem. Phys. 121 (2004) 5400-5409.

[77] M.D. Newton, S. Ehrenson, Ab initio studies on the structures and energetics of inner-and outer-shell hydrates of the proton and the hydroxide ion, J. Am. Chem. Soc. 93 (1971) 4971-4990.

[78] J. VandeVondele, F. Mohamed, M. Krack, J. Hutter, M. Sprik, M. Parrinello, The influence of temperature and density functional models in ab initio molecular dynamics simulation of liquid water, J. Chem. Phys. 122 (2005) 014515.

[79] M. Benoit, S. Ispas, P. Jund, R. Jullien, Model of silica glass from combined classical and ab initio molecular-dynamics simulations, The European Physical Journal B-Condensed Matter and Complex Systems. 13 (2000) 631-636.

[80] P. Jund, R. Jullien, Molecular-dynamics calculation of the thermal conductivity of vitreous silica, Physical review B. 59 (1999) 13707.

[81] D. Ceresoli, M. Bernasconi, S. Iarlori, M. Parrinello, E. Tosatti, Two-membered silicon rings on the dehydroxylated surface of silica, Phys. Rev. Lett. 84 (2000) 3887.

[82] A.C. Van Duin, A. Strachan, S. Stewman, Q. Zhang, X. Xu, W.A. Goddard, ReaxFFSiO reactive force field for silicon and silicon oxide systems, The Journal of Physical Chemistry A. 107 (2003) 3803-3811.

[83] J.R. Hill, J. Sauer, Molecular mechanics potential for silica and zeolite catalysts based on ab initio calculations. 1. Dense and microporous silica, J. Phys. Chem. 98 (1994) 1238-1244.

[84] B. Van Beest, G. Kramer, R. Van Santen, Force fields for silicas and aluminophosphates based on ab initio calculations, Phys. Rev. Lett. 64 (1990) 1955.

[85] J.C. Fogarty, H.M. Aktulga, A.Y. Grama, A.C. Van Duin, S.A. Pandit, A reactive molecular dynamics simulation of the silica-water interface, J. Chem. Phys. 132 (2010) 174704.

[86] J. Du, A.N. Cormack, Molecular dynamics simulation of the structure and hydroxylation of silica glass surfaces, J Am Ceram Soc. 88 (2005) 2532-2539.

[87] J. Rimsza, J. Du, Ab initio Molecular Dynamics Simulations of the Hydroxylation of Nanoporous Silica, J Am Ceram Soc. (2015).

[88] M. Kagan, G.K. Lockwood, S.H. Garofalini, Reactive simulations of the activation barrier to dissolution of amorphous silica in water, Physical Chemistry Chemical Physics. 16 (2014) 9294-9301.

[89] S.H. Garofalini, T.S. Mahadevan, S. Xu, G.W. Scherer, Molecular mechanisms causing anomalously high thermal expansion of nanoconfined water, ChemPhysChem. 9 (2008) 1997-2001.

[90] T. Mahadevan, S. Garofalini, Dissociative chemisorption of water onto silica surfaces and formation of hydronium ions, The Journal of Physical Chemistry C. 112 (2008) 1507-1515.

[91] E.B. Webb, S.H. Garofalini, Relaxation of silica glass surfaces before and after stress modification in a wet and dry atmosphere: molecular dynamics simulations, J. Non Cryst. Solids. 226 (1998) 47-57.

[92] F. Jensen, Introduction to Computational Chemistry, John Wiley & Sons, 2007.

[93] A. Rimola, P. Ugliengo, A quantum mechanical study of the reactivity of (SiO)-defective silica surfaces, J. Chem. Phys. 128 (2008) 204702.

[94] T.R. Walsh, M. Wilson, A.P. Sutton, Hydrolysis of the amorphous silica surface. II. Calculation of activation barriers and mechanisms, J. Chem. Phys. 113 (2000) 9191-9201.

[95] L.C. Pierce, R. Salomon-Ferrer, Augusto F. de Oliveira, Cesar, J.A. McCammon, R.C. Walker, Routine access to millisecond time scale events with accelerated molecular dynamics, Journal of chemical theory and computation. 8 (2012) 2997-3002.

[96] N. Allsopp, G. Ruocco, A. Fratalocchi, Molecular dynamics beyonds the limits: Massive scaling on 72 racks of a bluegene/p and supercooled glass dynamics of a 1 billion particles system, Journal of Computational Physics. 231 (2012) 3432-3445.

[97] A.C. Van Duin, S. Dasgupta, F. Lorant, W.A. Goddard, ReaxFF: a reactive force field for hydrocarbons, The Journal of Physical Chemistry A. 105 (2001) 9396-9409.

[98] J. Yeon, A.C. van Duin, ReaxFF Molecular Dynamics Simulations of Hydroxylation Kinetics for Amorphous and Nano-Silica Structure, and Its Relations with Atomic Strain Energy, The Journal of Physical Chemistry C. (2015).

[99] S.H. Garofalini, Molecular dynamics computer simulations of silica surface structure and adsorption of water molecules, J. Non Cryst. Solids. 120 (1990) 1-12.

[100] B. Feuston, S. Garofalini, Oligomerization in silica sols, J. Phys. Chem. 94 (1990) 5351-5356.

[101] T. Mahadevan, S. Garofalini, Dissociative water potential for molecular dynamics simulations, The Journal of Physical Chemistry B. 111 (2007) 8919-8927.

[102] A.A. Hassanali, S.J. Singer, Model for the water-amorphous silica interface: The undissociated surface, The Journal of Physical Chemistry B. 111 (2007) 11181-11193.

[103] P.E. Lopes, V. Murashov, M. Tazi, E. Demchuk, A.D. MacKerell, Development of an empirical force field for silica. Application to the quartz-water interface, The Journal of Physical Chemistry B. 110 (2006) 2782-2792.

[104] K. Muralidharan, J. Simmons, P. Deymier, K. Runge, Molecular dynamics studies of brittle fracture in vitreous silica: Review and recent progress, J. Non Cryst. Solids. 351 (2005) 1532-1542.

[105] M. Du, A. Kolchin, H. Cheng, Hydrolysis of a two-membered silica ring on the amorphous silica surface, J. Chem. Phys. 120 (2004) 1044.

[106] M. Du, A. Kolchin, H. Cheng, Water–silica surface interactions: A combined quantum-classical molecular dynamic study of energetics and reaction pathways, J. Chem. Phys. 119 (2003) 6418.

[107] V. Bakaev, W. Steele, On the computer simulation of a hydrophobic vitreous silica surface, J. Chem. Phys. 111 (1999) 9803.

[108] T.W. Dijkstra, R. Duchateau, R.A. van Santen, A. Meetsma, G.P. Yap, Silsesquioxane models for geminal silica surface silanol sites. A spectroscopic investigation of different types of silanols, J. Am. Chem. Soc. 124 (2002) 9856-9864.

[109] P.K. Gupta, M. Meuwly, Dynamics and vibrational spectroscopy of water at hydroxylated silica surfaces, Faraday Discuss. 167 (2013) 329-346.

[110] M. Sulpizi, M. Gaigeot, M. Sprik, The Silica–Water Interface: How the Silanols Determine the Surface Acidity and Modulate the Water Properties, Journal of Chemical Theory and Computation. 8 (2012) 1037-1047.

[111] D.W. Sindorf, G.E. Maciel, Silicon-29 NMR study of dehydrated/rehydrated silica gel using cross polarization and magic-angle spinning, J. Am. Chem. Soc. 105 (1983) 1487-1493.

[112] L. Zhuravlev, Concentration of hydroxyl groups on the surface of amorphous silicas, Langmuir. 3 (1987) 316-318.

[113] B. Morrow, I.D. Gay, Silicon-29 cross-polarization/magic angle spinning NMR evidence for geminal silanols on vacuum-activated aerosil silica, J. Phys. Chem. 92 (1988) 5569-5571.

[114] S.A. Carroll, R.S. Maxwell, W. Bourcier, S. Martin, S. Hulsey, Evaluation of silica-water surface chemistry using NMR spectroscopy, Geochim. Cosmochim. Acta. 66 (2002) 913-926.

[115] B.M. Lowe, C. Skylaris, N.G. Green, Acid-base dissociation mechanisms and energetics at the silica–water interface: An activationless process, J. Colloid Interface Sci. 451 (2015) 231-244.

[116] S. Hamad, S.T. Bromley, Low reactivity of non-bridging oxygen defects on stoichiometric silica surfaces, Chemical Communications. (2008) 4156-4158.

[117] W.A. Adeagbo, N.L. Doltsinis, K. Klevakina, J. Renner, Transport Processes at α-Quartz–Water Interfaces: Insights from First-Principles Molecular Dynamics Simulations, ChemPhysChem. 9 (2008) 994-1002.

[118] A.S. D'Souza, C.G. Pantano, Hydroxylation and dehydroxylation behavior of silica glass fracture surfaces, J Am Ceram Soc. 85 (2002) 1499-1504.

[119] G. Hochstrasser, J. Antonini, Surface states of pristine silica surfaces: I. ESR studies of Es′ dangling bonds and of CO2− adsorbed radicals, Surf. Sci. 32 (1972) 644-664.

[120] A.S. DSouza, C.G. Pantano, K.M. Kallury, Determination of the surface silanol concentration of amorphous silica surfaces using static secondary ion mass spectroscopy, Journal of Vacuum Science & Technology A: Vacuum, Surfaces, and Films. 15 (1997) 526-531.

[121] A.S. D'Souza, C.G. Pantano, Mechanisms for silanol formation on amorphous silica fracture surfaces, J Am Ceram Soc. 82 (1999) 1289-1293.

[122] K. Davis, M. Tomozawa, Water diffusion into silica glass: structural changes in silica glass and their effect on water solubility and diffusivity, J. Non Cryst. Solids. 185 (1995) 203-220.

[123] Y. Kim, T. Wei, J. Stultz, D. Goodman, Dissociation of water on a flat, ordered silica surface, Langmuir. 19 (2003) 1140-1142.

[124] T. Takamuku, M. Yamagami, H. Wakita, Y. Masuda, T. Yamaguchi, Thermal property, structure, and dynamics of supercooled water in porous silica by calorimetry, neutron scattering, and NMR relaxation, The Journal of Physical Chemistry B. 101 (1997) 5730-5739.

[125] F. Mallamace, C. Corsaro, M. Broccio, C. Branca, N. Gonzalez-Segredo, J. Spooren, S.H. Chen, H.E. Stanley, NMR evidence of a sharp change in a measure of local order in deeply supercooled confined water, Proc. Natl. Acad. Sci. U. S. A. 105 (2008) 12725-12729.

[126] M. Kasuya, M. Hino, H. Yamada, M. Mizukami, H. Mori, S. Kajita, T. Ohmori, A. Suzuki, K. Kurihara, Characterization of Water confined between Silica surfaces using the resonance shear measurement, The Journal of Physical Chemistry C. 117 (2013) 13540-13546.

[127] M.F. Harrach, F. Klameth, B. Drossel, M. Vogel, Effect of the hydroaffinity and topology of pore walls on the structure and dynamics of confined water, J. Chem. Phys. 142 (2015) 034703.

[128] D. Faux, S. Cachia, P. McDonald, J. Bhatt, N. Howlett, S. Churakov, Model for the interpretation of nuclear magnetic resonance relaxometry of hydrated porous silicate materials, Physical Review E. 91 (2015) 032311.

[129] K. Yamashita, H. Daiguji, Molecular simulations of water adsorbed on mesoporous silica thin films, The Journal of Physical Chemistry C. 117 (2013) 2084-2095.

[130] E. Chiavazzo, M. Fasano, P. Asinari, P. Decuzzi, Scaling behaviour for the water transport in nanoconfined geometries, Nature communications. 5 (2014).

[131] A.C. Fogarty, E. Duboué-Dijon, D. Laage, W.H. Thompson, Origins of the non-exponential reorientation dynamics of nanoconfined water, J. Chem. Phys. 141 (2014) 18C523.

[132] D. Hou, T. Zhao, H. Ma, Z. Li, Reactive Molecular Simulation on Water Confined in the Nanopores of the Calcium Silicate Hydrate Gel: Structure, Reactivity, and Mechanical Properties, The Journal of Physical Chemistry C. 119 (2015) 1346-1358.

[133] M. Rosenstihl, K. Kämpf, F. Klameth, M. Sattig, M. Vogel, Dynamics of interfacial water, J. Non Cryst. Solids. 407 (2015) 449-458.

[134] C. Allolio, F. Klameth, M. Vogel, D. Sebastiani, Ab Initio H2O in Realistic Hydrophilic Confinement, ChemPhysChem. 15 (2014) 3955-3962.

[135] T. Bakos, S. Rashkeev, S. Pantelides, H_ {2} O and O_ {2} molecules in amorphous SiO_ {2}: Defect formation and annihilation mechanisms, Physical Review B. 69 (2004) 195206.

[136] G.K. Lockwood, S.H. Garofalini, Lifetimes of Excess Protons in Water Using a Dissociative Water Potential, The Journal of Physical Chemistry B. 117 (2013) 4089-4097.

[137] O. Sneh, S.M. George, Thermal stability of hydroxyl groups on a well-defined silica surface, J. Phys. Chem. 99 (1995) 4639-4647.

[138] T.M. Clark, P.J. Grandinetti, P. Florian, J.F. Stebbins, Correlated structural distributions in silica glass, Physical Review B. 70 (2004) 064202.

[139] M. O'Keeffe, G. Gibbs, Ab initio MO calculations on cyclodisiloxanes and other Si-X-Si-X rings and the problem of" silica-w", J. Phys. Chem. 89 (1985) 4574-4577.

[140] M. O'Keeffe, G. Gibbs, Defects in amorphous silica: Ab initio MO calculations, J. Chem. Phys. 81 (1984) 876-879.

[141] H. Poulsen, J. Neuefeind, H.B. Neumann, J. Schneider, M. Zeidler, Amorphous silica studied by high energy X-ray diffraction, J. Non Cryst. Solids. 188 (1995) 63-74.

[142] E. Görlich, The structure of SiO2—Current views, Ceram. Int. 8 (1982) 3-16.

[143] M. Sitarz, M. Handke, W. Mozgawa, Identification of silicooxygen rings in SiO 2 based on IR spectra, Spectrochimica Acta Part A: Molecular and Biomolecular Spectroscopy. 56 (2000) 1819-1823.

[144] A. Pasquarello, R. Car, Identification of Raman defect lines as signatures of ring structures in vitreous silica, Phys. Rev. Lett. 80 (1998) 5145.

[145] A. Geissberger, F.L. Galeener, Raman studies of vitreous Si O 2 versus fictive temperature, Physical Review B. 28 (1983) 3266.

[146] S.K. Sharma, J.F. Mammone, M.F. Nicol, Raman investigation of ring configurations in vitreous silica, (1981).

[147] C. Brinker, R. Kirkpatrick, D. Tallant, B. Bunker, B. Montez, NMR confirmation of strained “defects” in amorphous silica, J. Non Cryst. Solids. 99 (1988) 418-428.

[148] B. Bunker, D. Haaland, K. Ward, T. Michalske, W. Smith, J. Binkley, C. Melius, C. Balfe, Infrared spectra of edge-shared silicate tetrahedra, Surf. Sci. 210 (1989) 406-428.

[149] P. Umari, X. Gonze, A. Pasquarello, Concentration of small ring structures in vitreous silica from a first-principles analysis of the Raman spectrum, Phys. Rev. Lett. 90 (2003) 027401.

[150] T. Uchino, Y. Kitagawa, T. Yoko, Structure, energies, and vibrational properties of silica rings in SiO 2 glass, Physical Review B. 61 (2000) 234.

[151] K. Vollmayr, W. Kob, K. Binder, Cooling-rate effects in amorphous silica: A computer-simulation study, Physical Review B. 54 (1996) 15808.

[152] P. Masini, M. Bernasconi, Ab initio simulations of hydroxylation and dehydroxylation reactions at surfaces: amorphous silica and brucite, Journal of Physics: Condensed Matter. 14 (2002) 4133.

[153] C. Mischler, J. Horbach, W. Kob, K. Binder, Water adsorption on amorphous silica surfaces: a Car–Parrinello simulation study, Journal of Physics: Condensed Matter. 17 (2005) 4005.

[154] P. Frugier, S. Gin, Y. Minet, T. Chave, B. Bonin, N. Godon, J. Lartigue, P. Jollivet, A. Ayral, L. De Windt, SON68 nuclear glass dissolution kinetics: Current state of knowledge and basis of the new GRAAL model, J. Nucl. Mater. 380 (2008) 8-21.

[155] L.J. Criscenti, J.D. Kubicki, S.L. Brantley, Silicate glass and mineral dissolution: calculated reaction paths and activation energies for hydrolysis of a Q3 Si by H3O using ab initio methods, The Journal of Physical Chemistry A. 110 (2006) 198-206.

[156] W.H. Casey, A.C. Lasaga, G. Gibbs, Mechanisms of silica dissolution as inferred from the kinetic isotope effect, Geochim. Cosmochim. Acta. 54 (1990) 3369-3378.

[157] N. Zotov, H. Keppler, Silica speciation in aqueous fluids at high pressures and high temperatures, Chem. Geol. 184 (2002) 71-82.

[158] N. Zotov, H. Keppler, Letters. In-situ Raman spectra of dissolved silica species in aqueous fluids to 900° C and 14 kbar, Am. Mineral. 85 (2000) 600-603.

[159] J.P. Icenhower, P.M. Dove, The dissolution kinetics of amorphous silica into sodium chloride solutions: effects of temperature and ionic strength, Geochim. Cosmochim. Acta. 64 (2000) 4193-4203.

[160] P.M. Dove, N. Han, A.F. Wallace, J.J. De Yoreo, Kinetics of amorphous silica dissolution and the paradox of the silica polymorphs, Proc. Natl. Acad. Sci. U. S. A. 105 (2008) 9903-9908.

[161] G. Bird, J. Boon, T. Stone, Silica transport during steam injection into oil sands: 1. Dissolution and precipitation kinetics of quartz: New results and review of existing data, Chem. Geol. 54 (1986) 69-80.

[162] J.D. Rimstidt, Quartz solubility at low temperatures, Geochim. Cosmochim. Acta. 61 (1997) 2553-2558.

[163] W.H. Casey, G. Sposito, On the temperature dependence of mineral dissolution rates, Geochim. Cosmochim. Acta. 56 (1992) 3825-3830.

[164] S.L. Brantley, B. Evans, S.H. Hickman, D.A. Crerar, Healing of microcracks in quartz: Implications for fluid flow, Geology. 18 (1990) 136-139.

[165] J.J. Mazer, J.V. Walther, Dissolution kinetics of silica glass as a function of pH between 40 and 85 C, J. Non Cryst. Solids. 170 (1994) 32-45.

[166] H. Kazi, J.M. Rimsza, J. Du, J.A. Kelber, Ar ions and oxygen plasma interactions of amine terminated organosilicate glass (OSG): a combined experimental and ab intio simulation study, JVSTA. (2014).

[167] P. Zapol, H. He, K.D. Kwon, L.J. Criscenti, First-Principles Study of Hydrolysis Reaction Barriers in a Sodium Borosilicate Glass, International Journal of Applied Glass Science. 4 (2013) 395-407.

[168] E.M. Pierce, P. Frugier, L.J. Criscenti, K.D. Kwon, S.N. Kerisit, Modeling Interfacial Glass-Water Reactions: Recent Advances and Current Limitations, International Journal of Applied Glass Science. 5 (2014) 421-435.

[169] G. Wirth, J. Gieskes, The initial kinetics of the dissolution of vitreous silica in aqueous media, J. Colloid Interface Sci. 68 (1979) 492-500.

[170] A. Chroneos, M. Rushton, C. Jiang, L. Tsoukalas, Nuclear wasteform materials: Atomistic simulation case studies, J. Nucl. Mater. 441 (2013) 29-39.

[171] J.D. Vienna, J.V. Ryan, S. Gin, Y. Inagaki, Current Understanding and Remaining Challenges in Modeling Long-Term Degradation of Borosilicate Nuclear Waste Glasses, International Journal of Applied Glass Science. 4 (2013) 283-294.

[172] M.R. Filgueiras, G. La Torre, L.L. Hench, Solution effects on the surface reactions of a bioactive glass, J. Biomed. Mater. Res. 27 (1993) 445-453.

[173] D. Clark, M. Dilmore, E. Ethridge, L. Hench, Aqueous Corrosion of Soda-Silica and Soda-Lime-Silica Glass, J Am Ceram Soc. 59 (1976) 62-65.

[174] J. Sheng, K. Kadono, Y. Utagawa, T. Yazawa, X-ray irradiation on the soda-lime container glass, Applied radiation and isotopes. 56 (2002) 621-626.

[175] T. Tarvornpanich, G. Souza, W. Lee, Microstructural evolution on firing soda–lime–silica glass fluxed whitewares, J Am Ceram Soc. 88 (2005) 1302-1308.

[176] G. Perera, R.H. Doremus, W. Lanford, Dissolution rates of silicate glasses in water at pH 7, J Am Ceram Soc. 74 (1991) 1269-1274.

[177] B. Bunker, Molecular mechanisms for corrosion of silica and silicate glasses, J. Non Cryst. Solids. 179 (1994) 300-308.

[178] S. Gin, Open Scientific Questions about Nuclear Glass Corrosion, Procedia Materials Science. 7 (2014) 163-171.

[179] V. Daux, C. Guy, T. Advocat, J. Crovisier, P. Stille, Kinetic aspects of basaltic glass dissolution at 90 C: role of aqueous silicon and aluminium, Chem. Geol. 142 (1997) 109-126.

[180] E.H. Oelkers, General kinetic description of multioxide silicate mineral and glass dissolution, Geochim. Cosmochim. Acta. 65 (2001) 3703-3719.

[181] K.G. Knauss, W.L. Bourcier, K.D. McKeegan, C.I. Merzbacher, S.N. Nguyen, F.J. Ryerson, D.K. Smith, H.C. Weed, L. Newton, Dissolution kinetics of a simple analogue nuclear waste glass as a function of pH, time and temperature, 176 (1989) 176.

[182] G. Berger, C. Claparols, C. Guy, V. Daux, Dissolution rate of a basalt glass in silica-rich solutions: implications for long-term alteration, Geochim. Cosmochim. Acta. 58 (1994) 4875-4886.

[183] F. Devreux, P. Barboux, M. Filoche, B. Sapoval, A simplified model for glass dissolution in water, J. Mater. Sci. 36 (2001) 1331-1341.

[184] T. Geisler, T. Nagel, M.R. Kilburn, A. Janssen, J.P. Icenhower, R.O. Fonseca, M. Grange, A.A. Nemchin, The mechanism of borosilicate glass corrosion revisited, Geochim. Cosmochim. Acta. 158 (2015) 112-129.

[185] S. Gin, P. Jollivet, M. Fournier, F. Angeli, P. Frugier, T. Charpentier, Origin and consequences of silicate glass passivation by surface layers, Nature communications. 6 (2015).

[186] C. Cailleteau, F. Angeli, F. Devreux, S. Gin, J. Jestin, P. Jollivet, O. Spalla, Insight into silicate-glass corrosion mechanisms, Nature materials. 7 (2008) 978-983.

[187] C. Cailleteau, C. Weigel, A. Ledieu, P. Barboux, F. Devreux, On the effect of glass composition in the dissolution of glasses by water, J. Non Cryst. Solids. 354 (2008) 117-123.

[188] D.M. Strachan, Glass dissolution: testing and modeling for long-term behavior, J. Nucl. Mater. 298 (2001) 69-77.

[189] B. Grambow, R. Müller, First-order dissolution rate law and the role of surface layers in glass performance assessment, J. Nucl. Mater. 298 (2001) 112-124.

[190] P. Abraitis, F. Livens, J. Monteith, J. Small, D. Trivedi, D. Vaughan, R. Wogelius, The kinetics and mechanisms of simulated British Magnox waste glass dissolution as a function of pH, silicic acid activity and time in low temperature aqueous systems, Appl. Geochem. 15 (2000) 1399-1416.

[191] G. Cox, B. Ford, The long-term corrosion of glass by ground-water, J. Mater. Sci. 28 (1993) 5637-5647.

[192] M. Bauchy, M.A. Qomi, F. Ulm, R. Pellenq, Order and disorder in calcium–silicate–hydrate, J. Chem. Phys. 140 (2014) 214503.

[193] D. Lu, J. Du, Effective empirical potentials and molecular dynamics simulations of the structures and properties of boroaluminosilicate glasses, J. Chem. Phys. (2016).

[194] M.M. Smedskjaer, J.C. Mauro, R.E. Youngman, C.L. Hogue, M. Potuzak, Y. Yue, Topological principles of borosilicate glass chemistry, The Journal of Physical Chemistry B. 115 (2011) 12930-12946.

[195] L. Kieu, J. Delaye, L. Cormier, C. Stolz, Development of empirical potentials for sodium borosilicate glass systems, J. Non Cryst. Solids. 357 (2011) 3313-3321.

[196] L. Huang, J. Kieffer, Thermomechanical anomalies and polyamorphism in B 2 O 3 glass: a molecular dynamics simulation study, Physical Review B. 74 (2006) 224107.

[197] A. Cormack, J. Du, Molecular dynamics simulations of soda–lime–silicate glasses, J. Non Cryst. Solids. 293 (2001) 283-289.

[198] A. Tilocca, A.N. Cormack, Modeling the Water− Bioglass Interface by Ab Initio Molecular Dynamics Simulations, ACS applied materials & interfaces. 1 (2009) 1324-1333.

[199] A. Tilocca, A.N. Cormack, Exploring the surface of bioactive glasses: water adsorption and reactivity, The Journal of Physical Chemistry C. 112 (2008) 11936-11945.

[200] A. Tilocca, Structure and dynamics of bioactive phosphosilicate glasses and melts from ab initio molecular dynamics simulations, Physical Review B. 76 (2007) 224202.

[201] A. Tilocca, A.N. Cormack, N.H. de Leeuw, The structure of bioactive silicate glasses: new insight from molecular dynamics simulations, Chemistry of materials. 19 (2007) 95-103.

[202] S. Kerisit, E.M. Pierce, Monte Carlo simulations of the dissolution of borosilicate glasses in near-equilibrium conditions, J. Non Cryst. Solids. 358 (2012) 1324-1332.

[203] S. Kerisit, E.M. Pierce, Monte Carlo simulations of the dissolution of borosilicate and aluminoborosilicate glasses in dilute aqueous solutions, Geochim. Cosmochim. Acta. 75 (2011) 5296-5309.

[204] A. Ledieu, F. Devreux, P. Barboux, Monte Carlo simulations of borosilicate glass corrosion: predictions for morphology and kinetics, J. Non Cryst. Solids. 345 (2004) 715-719.

[205] F. Devreux, P. Barboux, Numerical modelling of glass dissolution: gel layer morphology, J. Nucl. Mater. 298 (2001) 145-149.

[206] D.M. Strachan, T.L. Croak, Compositional effects on long-term dissolution of borosilicate glass, J. Non Cryst. Solids. 272 (2000) 22-33.

[207] L. Woodcock, C. Angell, P. Cheeseman, Molecular dynamics studies of the vitreous state: Simple ionic systems and silica, J. Chem. Phys. 65 (1976) 1565-1577.

[208] B.J. Alder, T. Wainwright, Studies in molecular dynamics. I. General method, J. Chem. Phys. 31 (1959) 459-466.

[209] B. Alder, T. Wainwright, Phase transition for a hard sphere system, J. Chem. Phys. 27 (1957) 1208.

[210] A. Nakano, R.K. Kalia, P. Vashishta, Growth of pore interfaces and roughness of fracture surfaces in porous silica: Million particle molecular-dynamics simulations, Phys. Rev. Lett. 73 (1994) 2336-2339.

[211] R.A. Buckingham, The classical equation of state of gaseous helium, neon and argon, 168 (1938) 264-283.

[212] J.G. Lee, Computational Materials Science: An Introduction, CRC Press, 2011.

[213] W. Smith, I.T. Todorov, A short description of DL_POLY, Molecular Simulation. 32 (2006) 935-943.

[214] S. Plimpton, LAMMPS user's manual, Sandia National Laboratory. (2005).

[215] R.M. Martin, Electronic Structure: Basic Theory and Practical Methods, Cambridge university press, 2004.

[216] J.P. Perdew, K. Burke, M. Ernzerhof, Generalized gradient approximation made simple, Phys. Rev. Lett. 77 (1996) 3865.

[217] A.D. Becke, Density-functional exchange-energy approximation with correct asymptotic behavior, Physical review A. 38 (1988) 3098.

[218] C. Lee, W. Yang, R.G. Parr, Development of the Colle-Salvetti correlation-energy formula into a functional of the electron density, Physical Review B. 37 (1988) 785.

[219] J. VandeVondele, M. Krack, F. Mohamed, M. Parrinello, T. Chassaing, J. Hutter, Quickstep: Fast and accurate density functional calculations using a mixed Gaussian and plane waves approach, Comput. Phys. Commun. 167 (2005) 103-128.

[220] C. Mundy, F. Mohamed, F. Schiffman, G. Tabacchi, H. Forbert, W. Kuo, J. Hutter, M. Krack, M. Iannuzzi, M. McGrath, CP2K software package, There is no corresponding record for this reference. (2000).

[221] G. Kresse, J. Furthmüller, Software VASP, vienna (1999), Phys.Rev.B. 54 (1996) 169.

[222] M. Edén, NMR studies of oxide-based glasses, Annual Reports Section" C"(Physical Chemistry). 108 (2012) 177-221.

[223] X. Yuan, A. Cormack, Efficient algorithm for primitive ring statistics in topological networks, Computational materials science. 24 (2002) 343-360.

[224] C. Chen, J. Du, Lithium Ion Diffusion Mechanism in Lithium Lanthanum Titanate Solid-State Electrolytes from Atomistic Simulations, J Am Ceram Soc. 98 (2015) 534-542.

[225] R.J. Tilley, Defects in Solids, John Wiley & Sons, 2008.

[226] J. Du, C. Chen, Structure and lithium ion diffusion in lithium silicate glasses and at their interfaces with lithium lanthanum titanate crystals, J. Non Cryst. Solids. 358 (2012) 3531-3538.

[227] R.S. Mulliken, Electronic population analysis on LCAO–MO molecular wave functions. I, J. Chem. Phys. 23 (1955) 1833-1840.

[228] R. Mulliken, Electronic population analysis on LCAO–MO molecular wave functions. II. Overlap populations, bond orders, and covalent bond energies, J. Chem. Phys. 23 (1955) 1841-1846.

[229] R.F. Bader, Atoms in Molecules, Wiley Online Library, 1990.

[230] F. Weinhold, J.E. Carpenter, The Natural Bond Orbital Lewis Structure Concept for Molecules, Radicals, and Radical Ions, in: Anonymous The Structure of Small Molecules and Ions, Springer, 1988, pp. 227-236.

[231] J. Rimsza, Y. Li, F. Pasquale, J. Kelber, J. Du, Chemical bonding in carborane/aromatic co-polymers: a first-principles analysis of experimental photoemission spectra, Molecular Simulation. (2015) 1-8.

[232] C.M. Jantzen, M.J. Plodinec, Thermodynamic model of natural, medieval and nuclear waste glass durability, J. Non Cryst. Solids. 67 (1984) 207-223.

[233] B. Feuston, S.H. Garofalini, Water-induced relaxation of the vitreous silica surface, J. Appl. Phys. 68 (1990) 4830-4836.

[234] B. Feuston, S. Garofalini, Empirical three-body potential for vitreous silica, J. Chem. Phys. 89 (1988) 5818.

[235] J. Rimsza, J. Du, Structural and Mechanical Properties of Nanoporous Silica, J Am Ceram Soc. 97 (2014) 772-781.

[236] J. Sauer, Molecular structure of orthosilicic acid, silanol, and H3SiOH. cntdot. AlH3 complex: models of surface hydroxyls in silica and zeolites, J. Phys. Chem. 91 (1987) 2315-2319.

[237] P. Ugliengo, V. Saunders, E. Garrone, Silanol as a model for the free hydroxyl of amorphous silica: ab-initio calculations of the interaction with water, J. Phys. Chem. 94 (1990) 2260-2267.

[238] J. Brédas, D. Beljonne, V. Coropceanu, J. Cornil, Charge-transfer and energy-transfer processes in π-conjugated oligomers and polymers: a molecular picture, Chem. Rev. 104 (2004) 4971-5004.

[239] D. Hamann, Energies of strained silica rings, Physical Review B. 55 (1997) 14784.

[240] M.L. Connolly, Analytical molecular surface calculation, Journal of Applied Crystallography. 16 (1983) 548-558.

[241] V. MaterialStudio, 3.0; Accelyrys, Inc, San Diego, CA. (2004).

[242] F. Gao, J. Du, E.J. Bylaska, M. Posselt, W.J. Weber, Ab Initio atomic simulations of antisite pair recovery in cubic silicon carbide, Appl. Phys. Lett. 90 (2007) 221915-221915-3.

[243] S. Gopalakrishnan, J.C. Diniz da Costa, Hydrogen gas mixture separation by CVD silica membrane, J. Membr. Sci. 323 (2008) 144-147.

[244] B.N. Nair, T. Yamaguchi, T. Okubo, H. Suematsu, K. Keizer, S.I. Nakao, Sol-gel synthesis of molecular sieving silica membranes, J. Membr. Sci. 135 (1997) 237-243.

[245] J.J. Li, X.Y. Xu, Z. Jiang, Z.P. Hao, C. Hu, Nanoporous silica-supported nanometric palladium: Synthesis, characterization, and catalytic deep oxidation of benzene, Environ. Sci. Technol. 39 (2005) 1319-1323.

[246] N. Doltsinis, M. Burchard, W. Maresch, A. Boese, T. Fockenberg, Ab initio molecular dynamics study of dissolved SiO 2 in supercritical water, Journal of Theoretical and Computational Chemistry. 6 (2007) 49-62.

[247] M. Sanders, M. Leslie, C. Catlow, Interatomic potentials for SiO 2, Journal of the Chemical Society, Chemical Communications. (1984) 1271-1273.

[248] F.H. Stillinger, T.A. Weber, Computer simulation of local order in condensed phases of silicon, Physical review B. 31 (1985) 5262.

[249] J.R. Rustad, B.P. Hay, A molecular dynamics study of solvated orthosilicic acid and orthosilicate anion using parameterized potentials, Geochim. Cosmochim. Acta. 59 (1995) 1251-1257.

[250] Markus J. Beuhler, From nano to macro: Introduction to atomistic modeling techniques
Introduction to atomistic modeling techniques: Do we need atoms to describe how materials behave? Department of Civil & Enviormental Engineering, Massachusets Institute of Technology. (2006).

[251] Y. Zhang, J. Tao, X. Chen, B. Liu, Mixed-pattern cracking in silica during stress corrosion: a reactive molecular dynamics simulation, Computational Materials Science. 82 (2014) 237-243.

[252] A.D. Kulkarni, D.G. Truhlar, S. Goverapet Srinivasan, A.C. van Duin, P. Norman, T.E. Schwartzentruber, Oxygen interactions with silica surfaces: Coupled cluster and density functional investigation and the development of a new ReaxFF potential, The Journal of Physical Chemistry C. 117 (2012) 258-269.

[253] A. El-Sayed, M.B. Watkins, T. Grasser, V.V. Afanas'ev, A.L. Shluger, Hydrogen-Induced Rupture of Strained Si─ O Bonds in Amorphous Silicon Dioxide, Phys. Rev. Lett. 114 (2015) 115503.

[254] A. Li, Y. Liu, I. Szlufarska, Effects of Interfacial Bonding on Friction and Wear at Silica/Silica Interfaces, Tribology Letters. 56 (2014) 481-490.

[255] K. Chenoweth, S. Cheung, A.C. Van Duin, W.A. Goddard, E.M. Kober, Simulations on the thermal decomposition of a poly (dimethylsiloxane) polymer using the ReaxFF reactive force field, J. Am. Chem. Soc. 127 (2005) 7192-7202.

[256] J. Rimsza, L. Deng, J. Du, Molecular dynamics simulations of nanoporous organosilicate glasses using Reactive Force Field (ReaxFF), J. Non Cryst. Solids. (2015).

[257] J. Kieffer, C.A. Angell, Generation of fractal structures by negative pressure rupturing of SiO< sub> 2</sub> glass, J. Non Cryst. Solids. 106 (1988) 336-342.

[258] X. Yuan, A. Cormack, Si–O–Si bond angle and torsion angle distribution in vitreous silica and sodium silicate glasses, J. Non Cryst. Solids. 319 (2003) 31-43.

[259] B. Civalleri, E. Garrone, P. Ugliengo, Vibrational modes of isolated hydroxyls of silica computed ab initio in a cluster approach, Chemical physics letters. 294 (1998) 103-108.

[260] J. Nedelec, L. Hench, Ab initio molecular orbital calculations on silica rings, J. Non Cryst. Solids. 255 (1999) 163-170.

[261] A. Tilocca, Models of structure, dynamics and reactivity of bioglasses: a review, Journal of Materials Chemistry. 20 (2010) 6848-6858.

[262] Y. Xiang, J. Du, M.M. Smedskjaer, J.C. Mauro, Structure and properties of sodium aluminosilicate glasses from molecular dynamics simulations, J. Chem. Phys. 139 (2013) 044507.

[263] D. McKeown, F. Galeener, G. Brown, Raman studies of Al coordination in silica-rich sodium aluminosilicate glasses and some related minerals, J. Non Cryst. Solids. 68 (1984) 361-378.

[264] A. Winkler, J. Horbach, W. Kob, K. Binder, Structure and diffusion in amorphous aluminium silicate: A molecular dynamics computer simulation, J. Chem. Phys. 120 (2004) 394-393.

[265] R. Morris, P. Wheatley, Gas Storage in Nanoporous Materials, Angewandte Chemie International Edition. 47 (2008) 4966-4981.

[266] J.M. Thomas, R. Raja, Review: The Materials Chemistry of Inorganic Catalysts, Aust. J. Chem. 54 (2002) 551-560.

[267] G. Leofanti, M. Padovan, G. Tozzola, B. Venturelli, Surface area and pore texture of catalysts, Catalysis Today. 41 (1998) 207-219.

[268] G. Ma, X. Yan, Y. Li, L. Xiao, Z. Huang, Y. Lu, J. Fan, Ordered nanoporous silica with periodic 30− 60 nm pores as an effective support for gold nanoparticle catalysts with enhanced lifetime, J. Am. Chem. Soc. 132 (2010) 9596-9597.

[269] S. Gin, C. Guittonneau, N. Godon, D. Neff, D. Rebiscoul, M. Cabié, S. Mostefaoui, Nuclear glass durability: new insight into alteration layer properties, The Journal of Physical Chemistry C. 115 (2011) 18696-18706.

[270] W.H. Casey, H.R. Westrich, J.F. Banfield, G. Ferruzzi, G.W. Arnold, Leaching and reconstruction at the surfaces of dissolving chain-silicate minerals, Nature. 366 (1993) 253-256.

[271] F. Angeli, T. Charpentier, S. Gin, J. Petit, 17 O 3Q-MAS NMR characterization of a sodium aluminoborosilicate glass and its alteration gel, Chemical physics letters. 341 (2001) 23-28.

[272] S. Gin, I. Ribet, M. Couillard, Role and properties of the gel formed during nuclear glass alteration: importance of gel formation conditions, J. Nucl. Mater. 298 (2001) 1-10.

[273] M. Cypryk, Y. Apeloig, Mechanism of the acid-catalyzed Si-O bond cleavage in siloxanes and siloxanols. A theoretical study, Organometallics. 21 (2002) 2165-2175.

[274] I. Li, J. Bandara, M.J. Shultz, Time evolution studies of the H2O/quartz interface using sum frequency generation, atomic force microscopy, and molecular dynamics, Langmuir. 20 (2004) 10474-10480.

[275] S.O. Diallo, Pore-size dependence and characteristics of water diffusion in slitlike micropores, Physical Review E. 92 (2015) 012312.

[276] G.E. Martin, S.H. Garofalini, Sol-gel polymerization: analysis of molecular mechanisms and the effect of hydrogen, J. Non Cryst. Solids. 171 (1994) 68-79.

[277] S.H. Garofalini, G. Martin, Molecular simulations of the polymerization of silicic acid molecules and network formation, J. Phys. Chem. 98 (1994) 1311-1316.

[278] I. Gunnarsson, S. Arnórsson, Amorphous silica solubility and the thermodynamic properties of H 4 SiO 4 in the range of 0 to 350 C at P sat, Geochim. Cosmochim. Acta. 64 (2000) 2295-2307.

[279] R.O. Fournier, J.J. Rowe, Solubility of amorphous silica in water at high temperatures and high pressure, Am.Mineral.;(United States). 62 (1977).

[280] G. Morey, R. Fournier, J. Rowe, The solubility of quartz in water in the temperature interval from 25 to 300 C, Geochim. Cosmochim. Acta. 26 (1962) 1029-1043.

[281] M. Elanany, P. Selvam, T. Yokosuka, S. Takami, M. Kubo, A. Imamura, A. Miyamoto, A quantum molecular dynamics simulation study of the initial hydrolysis step in sol-gel process, The Journal of Physical Chemistry B. 107 (2003) 1518-1524.

[282] J. Tossell, Theoretical study on the dimerization of Si (OH) 4 in aqueous solution and its dependence on temperature and dielectric constant, Geochim. Cosmochim. Acta. 69 (2005) 283-291.

[283] S. Leroch, M. Wendland, Simulation of forces between humid amorphous silica surfaces: A comparison of empirical atomistic force fields, The Journal of Physical Chemistry C. 116 (2012) 26247-26261.

[284] N. Ning, F. Calvo, A. Van Duin, D. Wales, H. Vach, Spontaneous self-assembly of silica nanocages into inorganic framework materials, The Journal of Physical Chemistry C. 113 (2008) 518-523.

[285] M.C. Pitman, A.C. Van Duin, Dynamics of confined reactive water in smectite clay–zeolite composites, J. Am. Chem. Soc. 134 (2012) 3042-3053.

[286] M.R. So, A.F. Voter, Temperature-accelerated dynamics for simulation of infrequent events, J. Chem. Phys. 112 (2000) 9599-9606.

[287] C.F. Abrams, E. Vanden-Eijnden, Large-scale conformational sampling of proteins using temperature-accelerated molecular dynamics, Proc. Natl. Acad. Sci. U. S. A. 107 (2010) 4961-4966.

[288] F. Montalenti, M. Sørensen, A. Voter, Closing the gap between experiment and theory: Crystal growth by temperature accelerated dynamics, Phys. Rev. Lett. 87 (2001) 126101.

[289] K. Koga, X.C. Zeng, H. Tanaka, Freezing of confined water: A bilayer ice phase in hydrophobic nanopores, Phys. Rev. Lett. 79 (1997) 5262.

[290] F.H. Stillinger, Water revisited, Science. 209 (1980) 451-457.

[291] R. Zangi, Water confined to a slab geometry: a review of recent computer simulation studies, Journal of Physics: Condensed Matter. 16 (2004) S5371.

[292] T.R. Dyke, K.M. Mack, J.S. Muenter, The structure of water dimer from molecular beam electric resonance spectroscopy, J. Chem. Phys. 66 (1977) 498-510.

[293] M. Chaplin, A proposal for the structuring of water, Biophys. Chem. 83 (2000) 211-221.

[294] W. Kuhs, M. Lehmann, The structure of the ice Ih by neutron diffraction, J. Phys. Chem. 87 (1983) 4312-4313.

[295] H. Graetsch, A. Mosset, H. Gies, XRD and 29 Si MAS-NMR study on some non-crystalline silica minerals, J. Non Cryst. Solids. 119 (1990) 173-180.

[296] S. Shibata, L. Bartell, Electron-Diffraction Study of Water and Heavy Water, J. Chem. Phys. 42 (1965) 1147-1151.

[297] J. Finney, A. Soper, Solvent structure and perturbations in solutions of chemical and biological importance, Chem. Soc. Rev. 23 (1994) 1-10.

[298] A. Soper, M. Phillips, A new determination of the structure of water at 25 C, Chem. Phys. 107 (1986) 47-60.

[299] J.P. Rino, I. Ebbsjö, R.K. Kalia, A. Nakano, P. Vashishta, Structure of rings in vitreous SiO 2, Physical Review B. 47 (1993) 3053.

[300] B.P. Spalding, D.B. Watson, Measurement of dissolved H2, O2, and CO2 in groundwater using passive samplers for gas chromatographic analyses, Environ. Sci. Technol. 40 (2006) 7861-7867.

[301] P.V. Brady, J.V. Walther, Controls on silicate dissolution rates in neutral and basic pH solutions at 25 C, Geochim. Cosmochim. Acta. 53 (1989) 2823-2830.

[302] P.V. Brady, J.V. Walther, Kinetics of quartz dissolution at low temperatures, Chem. Geol. 82 (1990) 253-264.

[303] P. Qian, L. Lu, W. Song, Z. Yang, Study of water clusters in the n= 2–34 size regime, based on the ABEEM/MM model, Theoretical Chemistry Accounts. 123 (2009) 487-500.

[304] C. Guittonneau, S. Gin, N. Godon, J. Mestre, O. Dugne, P. Allegri, A 25-year laboratory experiment on French SON68 nuclear glass leached in a granitic environment–First investigations, J. Nucl. Mater. 408 (2011) 73-89.

[305] K. Ferrand, A. Abdelouas, B. Grambow, Water diffusion in the simulated French nuclear waste glass SON 68 contacting silica rich solutions: Experimental and modeling, J. Nucl. Mater. 355 (2006) 54-67.

[306] D.K. Nordstrom, C.N. Alpers, C.J. Ptacek, D.W. Blowes, Negative pH and extremely acidic mine waters from Iron Mountain, California, Environ. Sci. Technol. 34 (2000) 254-258.

[307] R.C. Wolfe, K.G. Weil, B.A. Shaw, H.W. Pickering, Measurement of pH gradients in the crevice corrosion of iron using a palladium hydride microelectrode, J. Electrochem. Soc. 152 (2005) B82-B88.